Doctoral Dissertation
Doctoral Program in Metrology ($36^{th}$ cycle)

# Magnetic Nanoparticles for Biomedical Applications

**Marta Vassallo**
* * * * *

**Supervisors**
Dr. A. Manzin, Supervisor
Dr. C. Divieto, Co-supervisor

Politecnico di Torino
$9^{th}$ September 2024

This thesis is licensed under a Creative Commons License, Attribution - Noncommercial-NoDerivative Works 4.0 International: see www.creativecommons.org. The text may be reproduced for non-commercial purposes, provided that credit is given to the original author.

I hereby declare that, the contents and organization of this dissertation constitute my own original work and does not compromise in any way the rights of third parties, including those relating to the security of personal data.

. . . . . .

Marta Vassallo

Turin, 9$^{th}$ September 2024

# Summary

Magnetic nanoparticles (MNPs) are crucial and extensively studied for various biological applications due to their manipulability *via* external magnetic fields. For instance, they can be guided by a magnetic field gradient towards specific regions within the body. Additionally, when exposed to an alternating current (AC) magnetic field, they dissipate heat through energy loss mechanisms, with hysteresis being a significant contributor. An interesting biomedical application of MNPs is magnetic hyperthermia, which involves using MNPs to raise the temperature within tumor regions to 40-45 °C, thereby enhancing the sensitivity of cancer cells to other standard cancer therapies.

This thesis aims to develop MNPs with high thermal efficiency and to employ the generated heat for various applications, including magnetic hyperthermia on cell cultures, magnetically mediated drug delivery, drug-controlled release by thermosensitive nanocarriers, and the induction of acrylamide radical polymerization to produce hydrogels.

In this thesis work, the co-precipitation synthesis is employed to obtain magnetite ($Fe_3O_4$) and cobalt ferrite ($CoFe_2O_4$) NPs. After the synthesis, these MNPs are functionalized with different coating agents to improve their colloidal stability and heating efficiency. The synthesized MNPs are thoroughly characterized to determine their dimensional, physicochemical, magnetic, and heating properties. The effectiveness of the surface coatings is assessed through comprehensive characterization, comparing the thermal properties of untreated and treated MNPs to evaluate the effect of the coating. The results show that citrate coating significantly enhances the thermal properties of MNPs, which are expressed through the specific loss power (SLP) parameter.

The biocompatibility and potential cytotoxic effects of $Fe_3O_4$ and $CoFe_2O_4$ NPs at varying concentrations, both with and without citrate coating, are evaluated through *in vitro* cytotoxicity tests. Additionally, a novel protocol for conducting *in vitro* magnetic hyperthermia experiments using $Fe_3O_4$ NPs on adherent cultures of a human lung cancer cell line is developed.

Another focus of this work is the synthesis and characterization of magnetic oxygen-loaded nanodroplets (MOLNDs) through the magnetic decoration of the surface of oxygen-loaded nanodroplets (OLNDs). OLNDs are nanovectors capable of transporting oxygen and releasing oxygen molecules following exposure to an ultrasound (US) field. The purpose of the magnetic decoration is to create dual-responsive nanosystems (responsive to both US fields and AC magnetic fields) for the controlled release of oxygen. Four samples with varying compositions are synthesized and characterized in terms of dimensional and morphological properties. Characterization results confirm successful magnetic decoration and other experiments are performed to evaluate oxygen release induced by AC magnetic field exposure. *In vitro* cytotoxicity tests are also conducted to assess the biocompatibility of these nanohybrid systems.

Finally, an innovative method for inducing radical polymerization of polyacrylamide-based magnetic hydrogels is presented by exploiting the thermal energy released by $CoFe_2O_4$ NPs. Furthermore, the properties of hydrogels polymerized *via* AC magnetic field are compared with those polymerized through conventional heating methods. Specific experiments are presented, focusing on polymerizing magnetic hydrogels in a selective volume within a thermo-sensitive environment, as well as using MNPs concentrated in a small volume as a heat generator to polymerize non-magnetic hydrogels.

# Acknowledgements

I would like to acknowledge my supervisor, Alessandra Manzin (INRiM), and my co-supervisor, Carla Divieto (INRiM), for their invaluable guidance, support, and encouragement throughout my PhD studies. Their expertise and dedication have been fundamental to the successful completion of this thesis.
My sincere thanks go to Elena Sonia Olivetti (INRiM) and to the Department of Chemistry at the University of Florence, particularly to Daniele Martella, for their assistance in chemical synthesis and for generously providing access to the chemistry laboratories.
I would like to extend my thanks to Gabriele Barrera for his invaluable assistance and support during the magnetic characterization of materials. His expertise and guidance have been essential to the successful completion of my thesis.
I am also grateful to Jessica Petiti (INRiM) for her support with the biological experiments. Her collaboration and insights have significantly contributed to the advancement of my research.
I would also like to extend my appreciation to all my colleagues at INRiM who have made it possible for me to collaborate with them during the development of this thesis. In particular, I would like to thank Federica Celegato, Marco Coïsson, Riccardo Ferrero, Simone Galati, Luca Martino, Mattia Pegoraro, Paola Tiberto, Adriano Troia, and Marta Vicentini.
I am also grateful to Marco Loiacono (Department of Clinical and Biological Sciences, University of Turin) for allowing me to use the instruments in his laboratory, which greatly facilitated my experiments.
Additionally, I would like to acknowledge Hüseyin Sözeri (TÜBITAK, Turkey) and Marta Vallino (IPSP-CNR, Turin) for their support with TEM imaging.
Lastly, I am grateful to everyone else who has supported me in various ways throughout this journey. Your encouragement and assistance have been essential to the completion of this work.

# Contents

**Summary** II

**Contents** VI

**List of Tables** IX

**List of Figures** XI

**List of Abbreviations** XX

**1 Introduction** 1
- 1.1 Magnetic Nanoparticles . . . 3
  - 1.1.1 Methods for magnetic nanoparticle preparation . . . 4
  - 1.1.2 Activation of magnetic nanoparticles by alternating current magnetic fields . . . 7
- 1.2 Biomedical applications of magnetic nanoparticles . . . 10
  - 1.2.1 Magnetic Hyperthermia . . . 10
  - 1.2.2 Magnetic oxygen loaded nanodroplets . . . 12
  - 1.2.3 Radical polymerization of hydrogels induced by magnetic nanoparticles . . . 15
- 1.3 Outline of the Thesis . . . 17

**2 Synthesis and characterization of magnetic nanoparticles** 19
- 2.1 Materials and Methods . . . 19
  - 2.1.1 Reagents . . . 19
  - 2.1.2 Preparation of $Fe_3O_4$ nanoparticles . . . 20
  - 2.1.3 Preparation of $CoFe_2O_4$ nanoparticles . . . 20
  - 2.1.4 Characterization of magnetic nanoparticles . . . 20
- 2.2 Results . . . 22
  - 2.2.1 Magnetic nanoparticle synthesis . . . 22
  - 2.2.2 Magnetic nanoparticle characterization . . . 23
- 2.3 Conclusions . . . 31

**3 Influence of surface coating on the hyperthermia properties of $Fe_3O_4$ nanoparticles** 33
3.1 Materials and Methods . . . 33
3.1.1 Reagents . . . 33
3.1.2 Surface coating of $Fe_3O_4$ nanoparticles . . . 34
3.1.3 Dimensional characterization and assessment of surface coating of $Fe_3O_4$ nanoparticles . . . 34
3.1.4 Magnetic and thermometric characterization of $Fe_3O_4$ nanoparticles . . . 35
3.2 Results . . . 35
3.2.1 Assessment of surface coating . . . 35
3.2.2 Magnetic characterization . . . 40
3.2.3 Thermometric characterization . . . 43
3.3 Comparison with data in literature . . . 45
3.4 Analysis of nanoparticle solution stability . . . 49
3.5 Conclusions . . . 49

**4 *In vitro* experiments of magnetic hyperthermia** 51
4.1 Materials and Methods . . . 51
4.1.1 Reagents . . . 51
4.1.2 Cell culture . . . 51
4.1.3 Resazurine viability assay . . . 52
4.1.4 *In vitro* cytotoxicity tests . . . 53
4.1.5 *In vitro* magnetic hyperthermia tests . . . 54
4.2 Results . . . 55
4.2.1 *In vitro* cytotoxicity tests . . . 55
4.2.2 *In vitro* magnetic hyperthermia tests . . . 59
4.3 Conclusions . . . 65

**5 Magnetic oxygen-loaded nanodroplets** 67
5.1 Materials and Methods . . . 68
5.1.1 Reagents . . . 68
5.1.2 Synthesis of oxygen-loaded nanodroplets and decoration with $Fe_3O_4$ NPs . . . 68
5.1.3 Characterization . . . 69
5.1.4 Oxygen release through magnetic droplet vaporization . . . 71
5.1.5 *In vitro* test of cytotoxicity . . . 72
5.2 Results and Discussion . . . 74
5.2.1 Synthesis of oxygen-loaded nanodroplets and magnetic decoration . . . 74
5.2.2 Assessment of magnetic decoration . . . 77
5.2.3 Oxygen release through magnetic droplet vaporization . . . 83

5.2.4 *In vitro* cytotoxicity tests . . . . . 86
5.3 Conclusions . . . . . 88

**6 Application of magnetic hyperthermia in radical polymerization processes** 89
6.1 Materials and Methods . . . . . 90
6.1.1 Reagents . . . . . 90
6.1.2 Hydrogel preparation . . . . . 90
6.1.3 Hydrogel characterization . . . . . 90
6.2 Results . . . . . 91
6.2.1 Concept of radical polymerization *via* magnetic hyperthermia 91
6.2.2 Characterization of magnetic hydrogel . . . . . 93
6.2.3 Polymerization in thermosensitive environments *via* magnetic hyperthermia . . . . . 96
6.2.4 Preparation of non-magnetic hydrogel *via* magnetic hyperthermia . . . . . 99
6.3 Conclusions . . . . . 102

**Future perspectives** 103

**List of Publications** 104

**A Influence of surface coating on the hyperthermia properties of $Fe_3O_4$ nanoparticles** 1
A.1 Simulations with heat-transfer finite element solver . . . . . 1

**B Magnetic oxygen-loaded nanodroplets** 5
B.1 Acoustic response . . . . . 5
B.2 Numerical modeling of magnetic oxygen-loaded nanodroplet flow under magnetic field gradients . . . . . 11
B.3 Oxygen release following ultrasound field exposure . . . . . 14

**C Application of magnetic hyperthermia in radical polymerization processes** 17
C.1 Mechanical tests of polyacrylamide hydrogels . . . . . 17
C.2 Heat transfer numerical modeling . . . . . 20

**Bibliography** 25

# List of Tables


2.1 Mean hydrodynamic size, PDI and $\zeta$ potential values for the $Fe_3O_4$ NPs and $CoFe_2O_4$ NPs. . . . . 27
2.2 Values of saturation magnetization ($M_S$), remanent magnetization ($M_R$), and coercivity ($H_C$) of $Fe_3O_4$ NPs and $CoFe_2O_4$ NPs at room temperature. The magnetization values are normalized to the MNP mass. . . . . 28
2.3 SLP values for $Fe_3O_4$ and $CoFe_2O_4$ NPs, obtained at different peak amplitudes $\hat{H}_a$ of the AC magnetic field (24-48 kA/m), setting the frequency $f$ at 100 kHz. . . . . 31
3.1 Mean hydrodynamic size, polydispersity index (PDI) and $\zeta$ potential values for uncoated and coated $Fe_3O_4$ NPs. . . . . 39
3.2 Values of saturation magnetization ($M_S$), remanent magnetization ($M_R$), and coercivity ($H_C$) of uncoated and coated $Fe_3O_4$ NPs at room temperature. The magnetization values are normalized to the $Fe_3O_4$ mass. . . . . 41
3.3 SLP values for uncoated and coated $Fe_3O_4$ NPs, obtained at different peak amplitudes $\hat{H}_a$ of the AC magnetic field (24-48 kA/m), setting the frequency $f$ at 100 kHz. . . . . 45
3.4 Comparison of the results from our study to data from the literature regarding the heating efficiency of spherical $Fe_3O_4$ NPs. PVP = polyvinylpyrrolidone, PEG = polyethylene glycol, PAA = polyacrylic acid, HA = hyaluronic acid. . . . . 48
4.1 Initial temperature ($T_i$), equilibrium temperature ($T_{eq}$) and temperature variation ($\Delta T$) values for different concentrations of citrate-coated $Fe_3O_4$ NPs dispersed in DMEM, exposed to an AC magnetic field with a peak amplitude of 48 kA/m and a frequency of 100 kHz for 30 min. . . . . 62
5.1 Dimensions of the microchannel (BeFlow, BEOnChip) utilized in the microfluidic setup. . . . . 70
5.2 Composition and dimensions of the magnets used to generate magnetic field gradients. . . . . 71

5.3 Magnetic field generated by the magnets as a function of the distance. The measurements are performed with a hole probe. . . . . 71
5.4 Mean hydrodynamic diameters and $\zeta$ potential values of all the studied samples. . . . . 77
6.1 Parameters obtained by gravimetric characterization of the hydrogels. 95
C.1 Summary of the mechanical properties of the hydrogels. . . . . 19
C.2 Summary of the material properties used in the thermal simulations. 21

# List of Figures


1.1 Classification of nanomaterials based on size. . . . . 2
1.2 Main biomedical applications of MNPs. This image is extracted from ref. [29]. . . . . 3
1.3 Comparative analysis of advantages and disadvantages associated with different chemical synthesis techniques. . . . . 5
1.4 M-H curves of (**A**) ferromagnetic nanoparticles and (**B**) superparamagnetic nanoparticles, featuring $M_s$ as magnetic saturation, $M_r$ as remanent magnetization, and $H_c$ as coercivity. (**C**) Illustration of transitions from superparamagnetic behavior to single-domain and multi-domain configurations in relation to particle size; this image is extracted from ref. [40]. . . . . 8
1.5 Schematic representation of the mechanism of action of magnetic hyperthermia. This image is extracted from ref. [30]. . . . . 11
1.6 Diagram illustrating the magnetic decoration of oxygen-loaded nanodroplets with $Fe_3O_4$ NPs, followed by activation via AC magnetic field, leading to oxygen release through magnetic droplet vaporization. This Figure is reported in ref. [88]. . . . . 14
1.7 General reaction of free radical polymerizations. . . . . 15
1.8 Schematic representation of radical polymerization induced by MNPs heating. This Figure is reported in ref. [115]. . . . . 16
2.1 (**A**) Picture of the thermometric setup and (**B**) schematic of the sample container used for the determination of the SLP of MNPs. . 22
2.2 Schematic representation of the chemical preparation of $Fe_3O_4$ NPs *via* co-precipitation. . . . . 23
2.3 Schematic representation of the chemical preparation *via* co-precipitation of $CoFe_2O_4$ NPs. . . . . 23
2.4 (**A**) Representative TEM images and (**B**) size distribution histogram (derived from statistical analysis on TEM images) of $Fe_3O_4$ NPs. . . 24
2.5 (**A**) Representative TEM images and (**B**) size distribution histogram (derived from statistical analysis on TEM images) of $CoFe_2O_4$ NPs. 24

2.6 XRD pattern of $Fe_3O_4$ NPs, reporting the square root of the intensities. The characteristic diffraction peaks of $Fe_3O_4$ (ICDD PDF card no. 01-075-0033) and $\gamma$-$Fe_2O_3$ (ICDD PDF card no. 00-039-1346) are indicated, respectively, with the red and green vertical lines. . . 25
2.7 XRD pattern of $CoFe_2O_4$ NPs, reporting the square root of the intensities. The characteristic diffraction peaks of $CoFe_2O_4$ are indicated with the blue vertical lines. . . . . 26
2.8 DLS particle size distributions for (**A**) $Fe_3O_4$ NPs and (**B**) $CoFe_2O_4$ NPs. The dashed curves represent the Gaussian fits of the distributions, which serve as a guide to the eye. . . . . 27
2.9 Room-temperature $M(H)$ curves of (**A**) $Fe_3O_4$ NPs and (**B**) $CoFe_2O_4$ NPs in dry form. The magnetization values are normalized to the MNP mass and the portion of the hysteresis loops around remanent magnetization and coercivity is shown zoomed in the inset. . . . . 28
2.10 Time evolutions of the temperature of the magnetic suspensions containing (**A**) $Fe_3O_4$ and (**B**) $CoFe_2O_4$ NPs following the application of an AC magnetic field with different peak amplitudes $\hat{H}_a$ variable in the range 24-48 kA/m and frequency $f$ fixed to 100 kHz. . . . . 30
2.11 SLP values for $Fe_3O_4$ and $CoFe_2O_4$ NPs obtained at different peak amplitudes $\hat{H}_a$ of the AC magnetic field, fixing the frequency $f$ to 100 kHz. . . . . 30
3.1 Schematic representation of the surface coating process of $Fe_3O_4$ NPs. 35
3.2 Representative TEM images and size distributions of $Fe_3O_4$ NPs with (**A**) citrate coating and (**B**) carboxymethyl cellulose coating. . . . . 36
3.3 FTIR spectra of $Fe_3O_4$ NPs (black) and coated NPs with tri-sodium citrate (red) and CMC (blue). . . . . 37
3.4 Thermogravimetric analysis curves for uncoated (black), citrate-coated (red), and CMC-coated (blue) $Fe_3O_4$ NPs. . . . . 38
3.5 DLS particle size distribution for uncoated (black), citrate-coated (red), and CMC-coated (blue) $Fe_3O_4$ NPs (the reported Gaussian fits are a guide to the eye). . . . . 39
3.6 Room-temperature $M(H)$ curves of uncoated and coated $Fe_3O_4$ NPs in dry form. The magnetization values are normalized to the $Fe_3O_4$ mass, subtracting the coating mass obtained from TGA results. A hysteretic behavior can be inferred from the inset, which shows the portion of the hysteresis loops zoomed around coercivity and remanence. 40

3.7 Dynamic hysteresis loops at room temperature of uncoated and coated $Fe_3O_4$ NPs. The measurements were performed on liquid samples at different values of the AC magnetic field peak amplitude ($\hat{H}_a$) in the range 13-32 kA/m, fixing the frequency ($f$) to 69 kHz. All the hysteresis curves are normalized to the $Fe_3O_4$ mass and reported in arbitrary units with the same inferior and superior limits, to enable direct comparison. . . . . 41
3.8 Dynamic minor hysteresis loops for uncoated (black), citrate-coated (red), and CMC-coated (blue) $Fe_3O_4$ NPs for a magnetic field with peak amplitude $\hat{H}_a$ of (**A**) 13.3 kA/m and (**B**) 28.4 kA/m. All of the hysteresis curves are normalized to the $Fe_3O_4$ mass and reported in arbitrary units with the same inferior and superior limits to enable direct comparison. . . . . 42
3.9 Areas of the dynamic hysteresis loops versus $\hat{H}_a$, evaluated for all of the considered samples at a $f$ of 69 kHz. . . . . 43
3.10 Time evolutions of the temperature of the magnetic suspensions containing the uncoated NPs, the citrate- and CMC-coated NPs following the application of an AC magnetic field with different peak amplitudes $\hat{H}_a$ variable in the range 24-48 kA/m and frequency fixed to 100 kHz. The cooling transients, after the switching off of the field, are also reported. The graphs contain the experimental data and the best fit outputs of the analytical thermodynamic model. . . . . 44
3.11 SLP values for uncoated and coated $Fe_3O_4$ NPs obtained at different peak amplitudes $\hat{H}_a$ of the AC magnetic field, fixing the frequency $f$ to 100 kHz. . . . . 45
3.12 (**A**) Images of magnetic solutions, taken after 6 months from their synthesis. (**B**) Images of agarose gels with encapsulated MNPs. The comparison was made between uncoated, citrate-coated, and CMC-coated NPs. . . . . 49
4.1 Enzymatic reduction of resazurin to resorufin. . . . . 53
4.2 Cell viability assessment on A549 cell cultures after incubation with uncoated (left) and citrate-coated (right) $Fe_3O_4$ NPs. (**A**) Cell viability after 24, 48, and 72 h of treatment with different concentrations of $Fe_3O_4$ NPs, in the range 0-2 mg/mL, dissolved in the culture medium. (**B**) Histograms of cell viability at 72 h of treatment. Cell viability is evaluated using the resazurin assay and is quantified as a percentage of relative fluorescence units (RFU). In both cases, the reported data are normalized with respect to the control (without NP treatment), which is considered as 100%. RFU data are indicated as mean ± SD (biological replicate n° = 3). All the analyses with a $p$-value $< 0.05$ were indicated as statistically significant ($^*p \leq 0.05$; $^{**}p \leq 0.01$; $^{***}p \leq 0.001$; $^{****}p \leq 0.0001$). . . . . 57

4.3 Cell viability assessment on A549 cell cultures after incubation with uncoated (left) and citrate-coated (right) $CoFe_2O_4$ NPs. (**A**) Cell viability after 24, 48, and 72 h of treatment with different concentrations of $CoFe_2O_4$ NPs, in the range 0-2 mg/mL, dissolved in the culture medium. (**B**) Histograms of cell viability at 72 h of treatment. Cell viability is evaluated using the resazurin assay and is quantified as a percentage of relative fluorescence units (RFU). In both cases, the reported data are normalized with respect to the control (without NP treatment), which is considered as 100%. RFU data are indicated as mean ± SD (biological replicate n° = 3). All the analyses with a $p$-value $< 0.05$ were indicated as statistically significant ($^*p \leq 0.05$; $^{**}p \leq 0.01$; $^{***}p \leq 0.001$; $^{****}p \leq 0.0001$). . 58
4.4 Schematic of Experiment#2 conducted to evaluate the effects of magnetic hyperthermia induced by MNPs internalized within the cellular cytoplasm or closely associated with cell membranes. . . . . 60
4.5 Time evolution of the temperature of 0.4 mL of (**A**) distilled water and DMEM, (**B**) $Fe_3O_4$ NP solutions in DMEM at concentration of 0.1 mg/mL, with and without citrate coating, and (**C**) $Fe_3O_4$ NP solutions in DMEM with citrate coating at different concentrations (in the range 0.1-2 mg/mL) contained in the containers used for magnetic hyperthermia treatment under the exposure of the AC magnetic field. In all reported conditions, the AC magnetic field has a peak amplitude of 48 kA/m and a frequency of 100 kHz. . . . . 61
4.6 Temperature variation ($\Delta T$) values for different concentrations of citrate-coated $Fe_3O_4$ NPs, exposed to an AC magnetic field with a peak amplitude of 48 kA/m and a frequency of 100 kHz for 30 min. 62
4.7 Cellular viability assessment on A549 cell cultures following magnetic hyperthermia treatment with 1.5 mg/mL of uncoated and citrate-coated $Fe_3O_4$ NPs dispersed in the culture medium (Experiment#1). Cellular viability is evaluated using the resazurin assay at 24 and 48 h after a 30-min exposure to an AC magnetic field with a peak amplitude of 48 kA/m and a frequency of 100 kHz; the data are reported as a percentage of relative fluorescence units (RFU) normalized with respect to the control (untreated cells), which is set at 100%. RFU data are indicated as the mean ± SD of three technical replicates. Additionally, a control sample exposed to the AC magnetic field in the absence of MNPs is included to evaluate the potential effects of the magnetic fields on the cells. . . . . 63

4.8 Cellular viability assessment on A549 cell cultures following magnetic hyperthermia treatment induced by MNPs internalized within the cellular cytoplasm or closely associated with cell membranes (Experiment#2). The experiment is conducted with both uncoated and citrate-coated $Fe_3O_4$ NPs. Cellular viability is evaluated using the resazurin assay at 72 h after a 1-h exposure to an AC magnetic field with a peak amplitude of 48 kA/m and a frequency of 100 kHz; the data are reported as a percentage of relative fluorescence units (RFU) normalized with respect to the control (cells treated with MNPs but not exposed to the AC magnetic field), which is set at 100%. RFU data are indicated as the mean ± SD of three technical replicates. . 65
5.1 (**A**) Visual representation of the setup employed to observe the droplet behavior using an ecographic imaging probe, in the absence and presence of a magnet. (**B**) Image and schematic of the microfluidic setup designed to examine MOLND trajectories under the influence of a magnet, located in four distinct positions. . . . . 70
5.2 Visual depiction of the experimental system to evaluate oxygen release induced by the AC magnetic field stimulus. . . . . 72
5.3 Schematic representation of MOLND structure. . . . . 74
5.4 Representative SEM images of the marks left on a silicon substrate by (**A**) DFP-OLNDs and (**B**) DFP-MOLNDs, both with chitosan coating. . . . . 75
5.5 Representative TEM images of chitosan-coated DFP-MOLNDs. . . 75
5.6 Hydrodynamic size distributions obtained through DLS for all samples of OLNDs and MOLNDs with both cores, DFP or PFP, and both coatings, chitosan or dextran. . . . . 76
5.7 Frames showing the motion of DFP- or PFP-based MOLNDs with chitosan coating are presented in three subsequent frames following the exposure to a US field. In both cores, the upper sequence illustrates the behavior of droplet samples in the absence of a magnetic field gradient, while the lower sequence shows their behavior in the presence of a magnetic field gradient generated by a permanent magnet, indicated by the red box. Green circles are employed to emphasize the trajectory of a single droplet over time. . . . . 78
5.8 Frames showing the motion of DFP- or PFP-based MOLNDs with dextran coating are presented in three subsequent frames following the exposure to a US field. In both cores, the upper sequence illustrates the behavior of droplet samples in the absence of a magnetic field gradient, while the lower sequence shows their behavior in the presence of a magnetic field gradient generated by a permanent magnet, indicated by the red box. Green circles are employed to emphasize the trajectory of a single droplet over time. . . . . 79

5.9 Average streaming velocities of DFP- and PFP-based MOLNDs in the absence or presence of a magnetic field gradient. . . . . 80
5.10 Frames at two subsequent time instants displaying the trajectory of a DFP-MOLND with chitosan coating (green circle) under the influence of a magnet placed next to the microchannel flow. . . . . 81
5.11 Mean deflection angle values obtained for DFP-core MOLNDs for all magnetic field gradient conditions. . . . . 82
5.12 Mean values of streaming velocity obtained for DFP-core MOLNDs for all magnetic field gradient conditions. The values are normalized with respect to the "No Magnet" case. . . . . 82
5.13 Variation in oxygen concentration observed for each MOLND sample at selected temperatures following AC magnetic field excitation. The uniform magnetic field applied has a peak amplitude of 72 kA/m and a frequency of 100 kHz. . . . . 84
5.14 Heating curves of chitosan-coated MOLNDs with DFP- and PFP-core. 85
5.15 Optical microscope images of magnetically vaporized MOLNDs at the respective boiling points of both fluorocarbon cores. . . . . 85
5.16 Cell viability assessment (% RFU) on A549 cell culture after 24-, 48- and 72-hour incubation with MOLNDs using resazurin assay. Control refers to cells without MOLND treatment, while other cell samples were treated with four different dilutions of MOLNDs (1:20, 1:10, 1:8, and 1:5) in the culture medium. The reported data are normalized with respect to the control, which is considered as 100%. RFU data are indicated as mean ± SD (for a number of biological replicates equal to 3). All the analyses with a $p < 0.05$ were indicated as statistically significant ($^{*}$ $p \leq 0.05$; $^{**}$ $p \leq 0.01$; $^{***}$ $p \leq 0.001$; $^{****}$ $p \leq 0.0001$). . . . . 87
6.1 (**A**) Schematic of magnetic hyperthermia based heating to activate a radical polymerization. (**B**) Picture of the setup for radical polymerization by magnetic hyperthermia. . . . . 92
6.2 (**A**) Images of the initial hydrogel formulation, and the same after AC magnetic field application or immersion in a heating bath at 60 °C. In the first case, the image depicts a liquid state of the material during the vial inversion test, indicating no polymerization. Conversely, a solid hydrogel was observed to form through conventional heating. (**B**) Pictures of the initial hydrogel formulation doped with $CoFe_2O_4$ NPs and the same after AC magnetic field application. In this case, the picture demonstrates a solid material during the vial inversion test. (**C**) Temperature time evolution during the AC magnetic field exposure in a formulation containing the $CoFe_2O_4$ NPs. The temperature behaviour after the magnetic field switching off is also reported. . . . . 93

6.3 The ATR spectrum of the acrylamide monomer exhibits the characteristic peak at 816 $cm^{-1}$ corresponding to the C=C bending. For MNPs, the band at $530 - 580$ $cm^{-1}$ (554 $cm^{-1}$) can be attributed to the stretching vibration of Fe-O and Co-O bonds. In both the hydrogels, the disappearance of the peak at 816 $cm^{-1}$ demonstrates complete polymerization. . . . . 94
6.4 Comparison between static hysteresis loops at room temperature of magnetic hydrogels prepared by MNP based heating and classical bulk heating. . . . . 96
6.5 Possible application to induce polymerization in thermo-sensitive environments. An ultra-low gelling temperature agarose hydrogel shell (**A**) was filled with the acrylamide formulation (**B**). The samples were subjected to: (**C**) heating in a thermal bath (obtaining agarose melting and mixing of the materials); (**D**) magnetic hyperthermia (to achieve selective acrylamide polymerization). The vial inversion showed the formation of a solid hydrogel. . . . . 98
6.6 Time evolution of the temperature inside the acrylamide formulation during magnetic hyperthermia application. In this case, the formulation was placed inside an agarose shell during AC magnetic field application with a peak amplitude of 56 kA/m and a frequency of 100 kHz. . . . . 98
6.7 Picture of the hydrogel before (**A**) and after (**B**) dissolution of $CoFe_2O_4$ NPs by soaking the hydrogel in HCl (1M) for 3 days. . . . . 99
6.8 Possible application to prepare non-magnetic hydrogels. (**A**) Scheme of polymerization due to magnetic hyperthermia by MNPs concentrated on the bottom of the vial. (**B**) Sequence of pictures showing the protocol followed to obtain non-magnetic hydrogels polymerized by the action of the MNPs concentrated on one side. . . . . 100
6.9 (**A**) Scheme of polymerization applied in the experiments in the other panels. The reaction has been carried out by magnetic hyperthermia when the MNPs are concentrated on the bottom of the vial; (**B**) Picture of two samples after exposure to the same field application (56 kA/m for 20 min). Only if MNPs were present in the formulation, a solid hydrogel was formed; (**C**) Picture of two samples after exposure to the AC magnetic field (56 kA/m) for different times. After 20 min of application, the whole solution was converted into a solid hydrogel. For a shorter time (10 min), only a partial polymerization was detected. The formed hydrogel was extracted from the solution to take the picture. . . . . 101
A.1 Schematic of the sample container, corresponding to the domain considered for the heat-transfer numerical modeling. . . . . 3

A.2 Time evolutions of the temperature of the magnetic suspensions containing (**A**) the uncoated NPs and (**B**) the citrate-coated NPs, following the application for 60 min of an AC magnetic field with a peak amplitude of 48 kA/m) and a frequency of 100 kHz. The graphs contain the experimental data, the best fit outputs of the analytical thermodynamic model and the results obtained with the heat-transfer numerical model. (**C**) Spatial distribution of the temperature, calculated for the uncoated NP sample at the end of the heating interval. . . . . 3
B.1 Acoustic spectra of DFP-core OLNDs and MOLNDs with chitosan and dextran coating, measured at three acoustic pressures (0.47, 0.78 and 1.54 MPa). The reported results are based on the average of three acquired values. . . . . 7
B.2 Acoustic spectra of PFP-core OLNDs and MOLNDs with chitosan and dextran coating, measured at three acoustic pressures (0.47, 0.78 and 1.54 MPa). The reported results are based on the average of three acquired values. . . . . 8
B.3 Cavitation Noise Power (CNP) values evaluated in the acoustic pressure range 0.47-1.74 MPa for DFP-core nanodroplets: comparison between OLNDs (top) and MOLNDs (bottom). The reported results are based on the average of three acquired values. . . . . 9
B.4 Cavitation Noise Power (CNP) values evaluated in the acoustic pressure range 0.47-1.74 MPa for PFP-core nanodroplets: comparison between OLNDs (top) and MOLNDs (bottom). The reported results are based on the average of three acquired values. . . . . 10
B.5 Spatial distribution of the amplitude of the magnetic field produced by the permanent magnet in the $xz$-plane. The magnet is assumed to be uniformly magnetized along the out-of-plane direction, with a magnetization of 715 kA/m. The magnetization value was chosen to guarantee a good agreement between simulation and magnetic field measurement results obtained with a Hall probe. . . . . 12
B.6 Trajectories in $xz$-plane calculated for (**A**) chitosan-coated DFP-MOLNDs and (**B**) dextran-coated DFP-MOLNDs, for magnet position 3. (**C**) Trajectories in the $xy$-plane calculated for chitosan-coated DFP-MOLNDs, for magnet position 1. In the simulation graphs, the magnet center is positioned at $x = 20$ mm. . . . . 14
B.7 (**A**) Visual depiction of the setup used to conduct oxygen release experiments on OLND samples during US exposure ($f_0 = 1$ MHz, $P_a = 0.13$ MPa). (**B**) Variations of the oxygen concentration collected by the oximeter probe during US excitation over time (270 s). . . . 15

C.1 Rheological and mechanical tests on hydrogels with and without $CoFe_2O_4$ NPs: (**A**) frequency dependence of the viscoelastic shear moduli; (**B**) stress-strain curves for unconfined compression. . . . . 18
C.2 Rheological and mechanical tests on non-magnetic hydrogels obtained by magnetic hyperthermia polymerization with confined MNPs. (**A**) Frequency dependence of the viscoelastic shear moduli; (**B**) stress-strain curves for unconfined compression (the computed elastic modulus is reported in the inset). "Gel slice #1" refers to the top slice, while "Gel slice #2" refers to the slice more in proximity to the MNPs. Data for the reference hydrogel obtained by simple bulk heating are the same as in Figure C.1. . . . . 19
C.3 (**A**) Simulated heating-cooling transients at different points within the sample, whose positions are marked in the map of Figure **B**. The time instants corresponding to the polymerization reaction start and the AC magnetic field switching off are indicated with dashed lines. (**B**) Spatial distribution of the temperature calculated on the longitudinal section of the vial at the temperature peak, associated with the maximal enthalpy change during the polymerization reaction. (**C**) Time interval required to reach 60 °C, as a function of the specific heating power released by MNPs (the experimental data is indicated with a red circle as a reference). . . . . 22
C.4 SLP versus AC magnetic field peak amplitude for two frequencies (150 and 300 kHz), for (**A**) JHU NPs, and (**B**) nanomag®-D-spio NPs. The blue and red markers correspond to the experimental data extrapolated from the literature, [211] whereas the black curves to their polynomial interpolation. Diagrams of the time interval required to reach 60 °C, as a function of MNP concentration and magnetic field peak amplitude, when using commercial MNPs, namely (**C-D**) JHU NPs and(**E-F**) nanomag®-D-spio NPs. . . . . 24

# List of Abbreviations

$\hat{H}_{\mathrm{a}}$ Peak amplitude of the magnetic field

$d_{\mathrm{C}}$ Critical Diameter

$f$ Frequency of the AC magnetic field

$H_{\mathrm{C}}$ Coercivity

$M_{\mathrm{R}}$ Remanent Magnetization

$M_{\mathrm{S}}$ Saturation Magnetization

$T_{\mathrm{eq}}$ Equilibrium Temperature

AC Alternating Current

APS Ammonium persulfate

ATCC American Type Culture Collection

ATR Attenuated Total Reflectance

CMC Carboxymethyl cellulose

CNP Cavitation Noise Power

DC Direct Current

DFP Decafluoropentane

DLS Dynamic Light Scattering

DMEM Dulbecco's Modified Eagle's Medium

DMSO Dimethyl sulfoxide

EDS Energy Dispersive Spectometry

FBS Fetal Bovine Serum

FFT Fast Fourier Transform

FI Fluorescence Intensity

FTIR Fourier Transform Infrared

HA Hyaluronic acid

ILP Intrinsic Loss Power

MDV Magnetic droplet vaporization

MNPs Magnetic Nanoparticles

MOLNDs Magnetic oxygen-loaded nanodroplets

MRI Magnetic Resonance Imaging

NADH Nicotinamide Adenine Dinucleotide

NADPH Nicotinamide Adenine Dinucleotide phosphate

NPs Nanoparticles

OLNBs Oxygen-loaded nanobubbles

OLNDs Oxygen-loaded nanodroplets

PAA Polyacrylic acid

PCD Passive Cavitation Detector

PDI Polidispersity index

PEG Polyethylene glycol

PFP Perfluoropentane

PVP Polyvinylpyrrolidone

RFU Relative Fluorescence Units

ROS Reactive Oxygen Species

SD Standard Deviation

SEM Scanning Electron Microscopy

SLP Specific Loss Power

TEM Transmission Electron Microscopy

TGA Thermogravimetric Analysis

US Ultrasound

VSM Vibrating Sample Magnetometer

XRD X-ray Diffraction

# Chapter 1

# Introduction

In recent decades, nanotechnologies have become crucial in scientific research due to their wide applicability across numerous sectors. The U.S. National Nanotechnology Initiative (NNI) in 2000 defined nanotechnology as the study and manipulation of matter at sizes between 1 and 100 nm, where unique physical, chemical, and biological properties emerge, distinct from those in bulk form. Nowadays, many products incorporate nanoscale components spanning pharmaceuticals, cosmetics, high-tech, and renewable energy sectors. Research in nanotechnologies is continuously evolving, and one promising branch is certainly nanomedicine, which involves the application of nanotechnologies in the biomedical field. Its main objective is to bring improvements in disease diagnosis, monitoring, prevention, and treatment. In this field, successful development has already been achieved with biosensors and nanomaterials for diagnostic, therapeutic, and regenerative applications. [1, 2] Notable applications include regenerative nanomedicine for repairing oro-facial fractures and cartilage regeneration. [3, 4] Diagnostic research explores the use of fluorescent or magnetic nanosystems for early disease diagnosis *via* imaging techniques such as Magnetic Resonance Imaging (MRI). [5] Therapeutic studies focus on utilizing nanostructures to trap, protect, and transport drugs to specific targets within the body, achieving therapeutic success without invasiveness or side effects, particularly in treating malignant tumors. [6, 7] Furthermore, a pioneering field within nanomedicine is theranostics, which integrates therapeutic drugs and diagnostic imaging agents within nanostructured systems, also exploiting different therapeutic modalities in response to specific stimuli. [8]

According to the recommendation of the European Commission 2011/696/EU dated 20.10.2011, the term nanomaterial refers to a natural, incidental, or manufactured material containing particles, either in an unbound state or as an aggregate or as an agglomerate and where, in which at least 50% of the number size distribution of the particles possesses one or more external dimensions in the size range 1-100 nm. Nanomaterials can be classified based on their dimensions, as illustrated in Figure 1.1. For instance, nanoparticles are nanomaterials with all three

dimensions falling within the nanoscale range, exhibiting no substantial difference between their longest and shortest axes, thus they can be defined as 0D nanomaterials. Nanofibers, on the other hand, can be considered as 1D nanomaterials since they have two of their dimensions in the nanoscale range; moreover, they may have either a solid (nanorods) or hollow (nanotubes) structure. Finally, nanoplates or nanosheets have one dimension in the nanoscale range and are defined as 2D nanomaterials. [9]

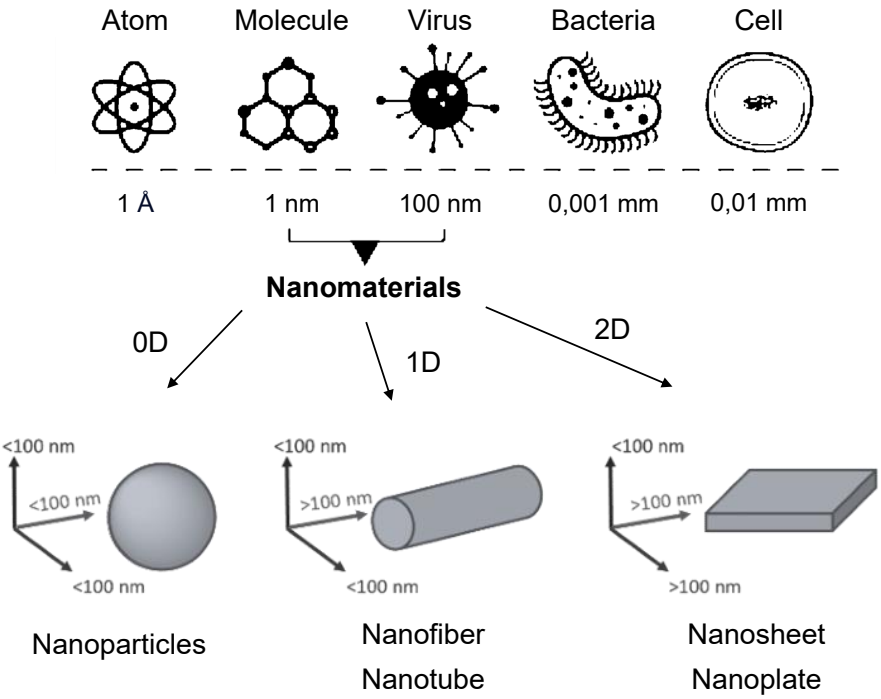



**Figure 1.1.** Classification of nanomaterials based on size.

Biocompatibility is a critical aspect in the development of nanomaterials for biomedical application. It refers to the ability of a material to interact with biological systems without causing undesirable effects. Alternatively, biocompatibility can be defined as the ability of the material to function appropriately within a specific application context. For these reasons, in recent decades, nanotoxicology has been increasingly developed, which is the discipline that assesses and studies the potential effects on the environment and human health of nanomaterials. [8] The toxicity issues associated with these materials depend on various factors, including size, shape, surface area, surface reactivity, density, and composition. For instance, the size of nanoparticles can influence their cellular uptake and distribution within the body, impacting their toxicity profiles. Similarly, the shape of nanomaterials can affect their interactions with biological molecules and cells, potentially altering their biological responses. Therefore, a comprehensive understanding of these

factors is essential for assessing and mitigating the toxicological risks associated with nanomaterials. [10, 11] Now, we focus on specific nanomaterials, magnetic nanoparticles.

## 1.1 Magnetic Nanoparticles

Magnetic nanoparticles (MNPs) are highly promising in various domains due to their magnetic properties, which enable manipulation through external magnetic fields. They exhibit very high surface area to volume ratio and physicochemical properties dependent on size, rendering them notably versatile and reactive when compared to their respective bulk material. [12] MNPs, owing to their unique physical, chemical, and magnetic properties, find applications across various fields, including environmental remediation, [13, 14] data and energy storage [15, 16], catalysis [17, 18], spintronics [19], magnetic inks [20], and biomedicine [21–30]. In the biomedical field, MNPs can be employed for various applications and are interesting due to their capability, for instance, to be guided by an external magnetic field to specific anatomical sites within the body and to induce the controlled release of encapsulated therapeutic agents in targeted regions. Examples of the main biomedical applications are summarized in Figure 1.2.

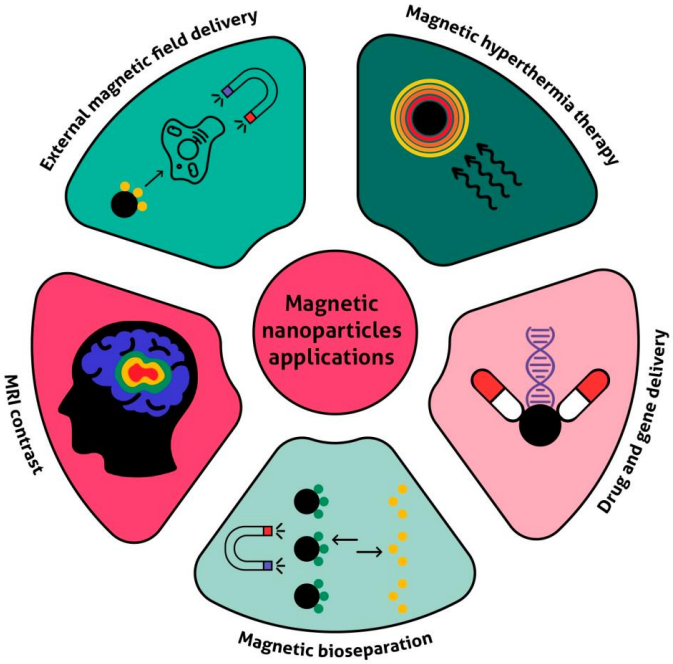



**Figure 1.2.** Main biomedical applications of MNPs. This image is extracted from ref. [29].

Particularly advantageous in biomedical contexts is the superparamagnetic behavior observed in small magnetic nanoparticles with dimensions below 20-30 nm. This behavior ensures that MNPs exhibit no residual magnetization upon cessation of the applied magnetic field, thereby preserving colloidal stability and preventing undesired aggregation or clustering. [1, 31] For MNPs to be suitable as nanocarriers for therapeutic applications, they must exhibit sufficient bioactivity and avoid eliciting inflammatory or cytotoxic reactions within the body. Among various types of MNPs, iron oxide nanoparticles, such as maghemite ($\gamma$-$Fe_2O_3$) and magnetite ($Fe_3O_4$), are of interest as they meet these criteria and also possess optimal chemical and physical attributes, including chemical stability and high saturation magnetization. Biocompatibility of these materials is attributed to the widespread presence of iron in bodily organs such as the heart, spleen, and liver, as well as its role as a fundamental component in essential biological molecules like hemoglobin, myoglobin, and ferritin, ensuring their biocompatibility. [32] However, other MNPs, such as those composed of cobalt ferrite or zinc ferrite, have been investigated for diverse biomedical applications. [33, 34] It is demonstrated that the application of polymers, ceramics, or molecules with high charge or steric hindrance as surface coatings is efficient in enhancing the biocompatibility and colloidal stability of MNPs. Furthermore, the presence of a surface coating can facilitate the functionalization with specific biomolecules, such as proteins, enzymes, or antibodies. [12, 35]
$Fe_3O_4$ nanoparticles, notably, exhibit remarkable responsiveness to external magnetic fields at physiological temperatures, owing to their high saturation magnetization values. Furthermore, their biocompatibility, low toxicity, and capacity for surface functionalization render them particularly suited for biomedical uses. Consequently, superparamagnetic $Fe_3O_4$ nanoparticles find widespread application in MRI [21, 22], targeted drug delivery [23, 24], magnetic hyperthermia [25, 26], and bio-separation [27, 28].

### 1.1.1 Methods for magnetic nanoparticle preparation

Various synthesis methods are employed to fabricate MNPs with tailored properties suitable for diverse applications, and they can be categorized into two main groups: top-down processes, which refers to the process of size reduction starting from the bulk material, and bottom-up processes, which refers to the process of building nanosized structures from molecular reagents. Methods of chemical synthesis, which are classified under the bottom-up approach, are frequently favored for their capability to obtain MNPs with meticulous control in terms of size, shape and narrow size distribution. Examples of these techniques include coprecipitation, thermal decomposition, hydrothermal, sol-gel and microwave-assisted approaches. [36] In Figure 1.3, the main advantages and disadvantages of these techniques are delineated.

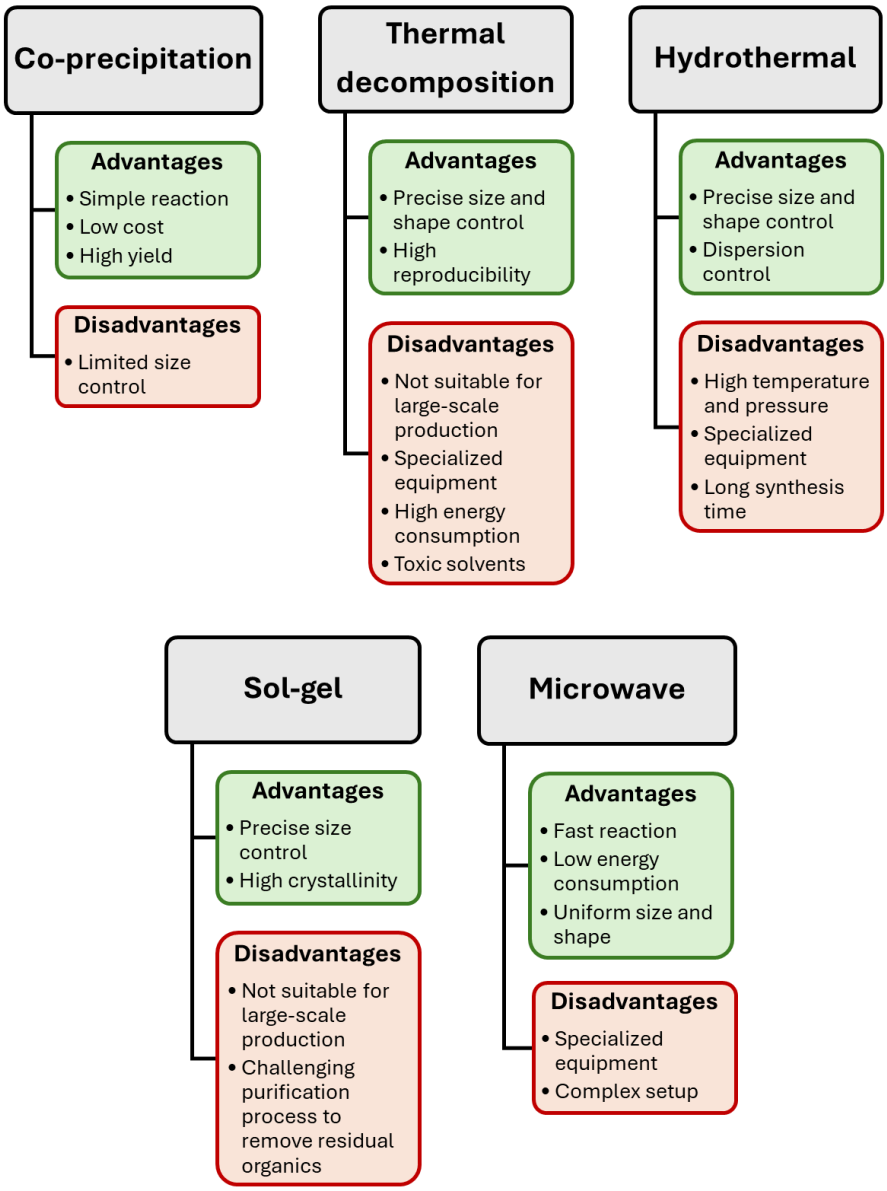



**Figure 1.3.** Comparative analysis of advantages and disadvantages associated with different chemical synthesis techniques.

- Co-precipitation is a method for synthesizing MNPs from aqueous salt solutions by adding a base as a precipitating agent, either at room temperature or at a higher temperature. This process is simple and practical, offering advantages such as high yield and the production of a large quantity of MNPs. It is considered one of the preferred synthesis methods due to its simplicity, high

yield, and potential for scalable industrial applications. For instance, $Fe_3O_4$ NPs can be synthesized by hydrolyzing an aqueous solution containing a base and iron salts at room temperature in an open environment. Co-precipitation involves the simultaneous precipitation of $Fe^{2+}$ and $Fe^{3+}$ ions to produce magnetite ($Fe_3O_4$) NPs. However, control over particle size distribution is limited as only kinetic factors are involved in crystal formation. To refine the size, shape, and chemical composition of the MNPs, it is essential to control reaction parameters such as the type of metal cation precursors, the molar ratio between the metal cations, reaction temperature, pH value, and the type and concentration of the alkaline agent. This method has been widely used also for the production of ferrite NPs, for example to synthesize cobalt or zinc ferrite. [36–39]

- Thermal decomposition is a method that involves the precursor heating to high temperatures in an inert atmosphere. During this process, precursor molecules undergo decomposition, leading to the formation of NPs. The decomposition typically occurs in a controlled environment, such as a tube furnace or a high-temperature reactor, where the temperature and gas atmosphere can be carefully regulated. This method allows for precise control over the size, shape, and composition of the resulting nanoparticles by adjusting parameters such as temperature, heating rate, and precursor concentration. However, while thermal decomposition offers advantages in terms of control and versatility, it may not be suitable for large-scale production due to the need for specialized equipment and the relatively high energy consumption associated with high-temperature processes. [36]

- Hydrothermal synthesis is a wet-chemical process that entails heating and dissolving iron precursors in an aqueous medium at high temperatures and elevated pressure. This method utilizes a Teflon-sealed stainless-steel autoclave with supercritical or sub-supercritical water, facilitating chemical processes. The iron oxide phase is achieved through the dehydration of hydroxide intermediates ($Fe(OH)_n$) produced during the hydrolysis of ferrous ions. Various factors, including synthesis temperature and precursor concentration, significantly affect reaction kinetics and nucleation rates, influencing particle size and size distribution. [36]

- Sol-gel method involves dissolving precursors in a liquid solution to form a suspension called "sol", which is then evaporated, causing the precursors to condense and form a solid structure, known as "gel". The obtained gel can then be further treated thermally to remove residual moisture and obtain the desired final material. This method allows for precise control of the material structure (i.e. highly crystalline and uniformly sized MNPs), but it may not be suitable for large-scale and cost-effective manufacturing. [36]

- Microwave-assisted synthesis utilizes exposure of reaction mixture to microwave radiation to induce uniform heating, which results in uniform crystallization and rapid formation of crystallites with a narrow size distribution. One of the advantages of this technique is the ability to produce MNPs with uniform size and shape. However, it also has drawbacks, such as slow reaction kinetics and the need for specialized equipment (microwave reactor). [36]

In conclusion, the choice of synthesis method can lead to MNPs with varying size, shape, and size distribution and consequently also lead to different magnetic and heating properties of MNPs. In this thesis work, the MNPs are synthesized using the co-precipitation method, as it allows for simple reactions and the production of a large quantity of MNPs.

### 1.1.2 Activation of magnetic nanoparticles by alternating current magnetic fields

The magnetic behavior of a material in the presence of an external magnetic field (**H**) reflects the collective response of its constituent atomic moments. This response is commonly characterized by the magnetic induction (**B**) or the magnetization vector (**M**), both of which vary with the applied field strength (**H**). The resulting M-H curve is unique to each material and is influenced by factors such as composition, as well as physical and geometrical properties. Specifically, the M-H curve exhibits distinct shapes corresponding to the magnetic behavior of the material, including diamagnetism, paramagnetism, and ferromagnetism. In the case of MNPs, they typically display ferromagnetic behavior, which is notably influenced by MNP size. MNPs larger than the critical size, which depends on the material composition and is usually in the range of 80-120 nm, are categorized as multi-domain. Conversely, those with sizes smaller than the critical size are considered single-domain. These MNPs may exhibit hysteresis, signifying an irreversible magnetization process, and are characterized by an M-H relationship depicted as a loop with a non-negligible area, known as hysteresis loop.
In Figure 1.4A, the characteristic shape of the M-H curve for ferromagnetic materials is illustrated, where $H_c$ represents the coercivity - a measure of the resistance to demagnetization of the material. $M_r$ is the remanent magnetization, which corresponds to the residual magnetization when the applied field diminishes to zero, while $M_s$ indicates the magnetic saturation, defining the asymptote of the curve as the applied field intensity increases. The hysteresis loss, corresponding to energy dissipation as heat, is proportional to the area enclosed by the hysteresis loop. Notably, particles smaller than 20-30 nm (the critical size is dependent on the material) exhibit a distinct magnetic behavior called superparamagnetism. Superparamagnetic materials lack hysteresis (i.e., remanent magnetization is absent),

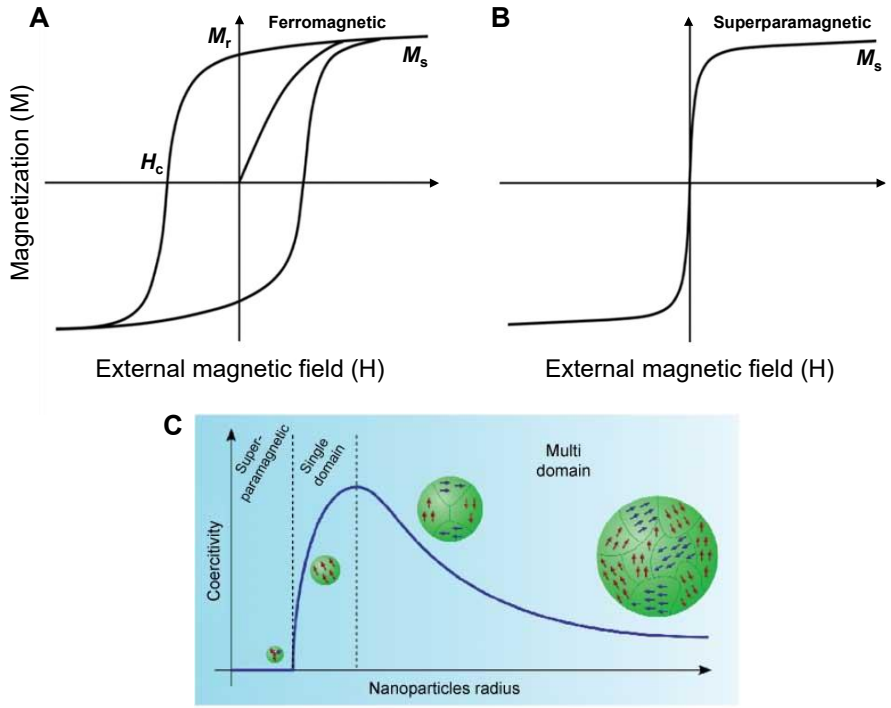



**Figure 1.4.** M-H curves of (**A**) ferromagnetic nanoparticles and (**B**) superparamagnetic nanoparticles, featuring $M_s$ as magnetic saturation, $M_r$ as remanent magnetization, and $H_c$ as coercivity. (**C**) Illustration of transitions from superparamagnetic behavior to single-domain and multi-domain configurations in relation to particle size; this image is extracted from ref. [40].

and their magnetization direction randomly fluctuates in response to thermal energy, even without an applied field. Figure 1.4B displays the typical M-H curve shape for superparamagnetic NPs, while Figure 1.4C schematically illustrates the transition from superparamagnetic behavior to single-domain and multi-domain configurations in relation to NP size and coercivity.

When a magnetic material is exposed to an alternating current (AC) magnetic field, heat dissipation occurs through various mechanisms of energy loss, including eddy current, hysteresis, and Brownian relaxation. [41, 42] Eddy current effects predominantly contribute to heating in bulk materials but are negligible in microparticles and nanoparticles due to their diminished dimensions and the low electrical conductivity of iron oxides. Conversely, other heating mechanisms involve the alignment of the magnetic moment of MNPs with the direction of the AC magnetic field, either through the rotation of magnetization vectors within MNPs (hysteresis) or via the mechanical rotation of MNPs within the medium, leading to the generation of frictional losses (Brownian relaxation). The latter is typically impeded in the tumor microenvironment, with only minor oscillations permitted

by tissue elasticity.
The magnetic behavior and resulting heating properties of materials are profoundly affected by the size of MNPs, with the existence of two critical dimensions that are dependent on the material type. The smallest critical size delineates the transition from superparamagnetic to single-domain ferromagnetic behavior. Beyond this threshold, the coercivity and consequently the hysteresis losses (absent in the superparamagnetic state) begin to increase gradually, reaching a maximum. This peak coincides with the largest critical size, which indicates the transition to multi-domain ferromagnetic behavior. Subsequently, as the size exceeds this critical point, both coercivity and hysteresis losses start to decline with dimension.
The heating efficiency of MNPs is commonly expressed through the specific loss power (SLP), a parameter that quantifies the thermal power dissipated per unit mass of magnetic material. [43] This parameter is influenced by a multitude of factors, encompassing not only the dimensional and physicochemical properties of MNPs (including size, shape, magnetic behavior, and state of aggregation) but also the conditions of magnetic field exposure, notably the amplitude and frequency of the field. [44–49] Concerning material properties, it is demonstrated that modifying magnetocrystalline anisotropy can lead to an increase in heating efficiency, as observed in the case of cobalt and zinc ferrites. [50–52] To determine the SLP of MNPs, thermometric measurements are typically conducted, wherein the temperature evolution in a suspension of MNPs contained within a vial exposed to an AC magnetic field is recorded. Typically, the data measured at a specific location within the sample, representing the exponential relationship between time ($t$) and temperature ($T$), are employed to calculate the SLP using the following equation, assuming that the process is conducted under adiabatic conditions and that there are no alterations within the sample [53]:

$$SLP = \frac{\Delta T}{\Delta t}\frac{C}{m_{\mathrm{Fe}}} \tag{1.1}$$

where $\Delta T/\Delta t$ represents the initial slope of the curve, $C$ is the volumetric heat capacity of the sample, and $m_{\mathrm{Fe}}$ is the mass of magnetic material present in the sample.
The estimation of the SLP is significant as a high value is required for efficient hyperthermia therapy, aiming to minimize the injected dose of MNPs within the body while ensuring a suitable temperature increase for therapeutic purposes.

### Enhancing magnetocrystalline anisotropy through doping of iron oxide nanoparticles

Magnetocrystalline anisotropy is a property where, due to spin-orbit coupling, there can be one or more energetically favorable directions along the crystalline lattice axes in which magnetization aligns. For example, in uniaxial anisotropy,

there is a single preferred direction along which the magnetization aligns, known as the magnetic easy axis. [54]
One way to enhance thermal efficiency, besides changing the size, shape, surface coating, aggregation state, and adjusting the parameters of the AC magnetic field, is to manipulate the magnetocrystalline anisotropy of MNPs. [55, 56] An increase of this property leads to greater coercivity in MNPs, directly impacting the hysteresis losses of the sample. [57]
To increase magnetocrystalline anisotropy, one approach is to modify the chemical composition of iron oxide nanoparticles by doping them with different metals (Co, Ni, Zn, Cu, Gd, Mn). It has been demonstrated that doped ferrites can show high magnetocrystalline anisotropy, resulting in larger coercivity and thus greater hysteresis losses. [55, 58]
For example, it is shown that cobalt ferrite NPs have an inverse spinel structure with $Co^{2+}$ ions mainly placed in octahedral sites and $Fe^{3+}$ ions almost equally distributed between tetrahedral and octahedral sites. They present high magnetocrystalline anisotropy constant and large coercivity. [59, 60] It has already been demonstrated that small-sized cobalt ferrite NPs, whose anisotropy constant is about 20-30 times greater than that of magnetite NPs, have a higher heating efficiency than magnetite NPs of the same size. [60]
However, it should be considered that the increase in heating efficiency also depends on the amount of cobalt present within the nanomaterial. It has been shown that the magnetic anisotropy of cobalt ferrite NPs ($Co_xFe_{3-x}O_4$) does not increase monotonically with the cobalt content ($x$), but increases up to a certain value of $x$, then decreases again for higher values. [60] It has also been demonstrated that higher temperatures are obtained with an increase in Co content until $x = 0.7$, while the temperature decreases for values of $x$ between 0.7 and 1, indicating that the magnetocrystalline anisotropy does not increase with the increase in Co content. [61, 62]

## 1.2 Biomedical applications of magnetic nanoparticles

### 1.2.1 Magnetic Hyperthermia

Hyperthermia is applied as an adjuvant to standard cancer therapies like radiotherapy and chemotherapy, aiming to enhance their effectiveness. This therapeutic approach involves raising the temperature within tumor regions to increase cancer cell sensitivity, thereby enhancing the therapeutic impact of standard treatments. Maintaining the temperature within the optimal range of 40-45 °C for an adequate duration, sometimes up to one hour, is crucial for achieving desired outcomes. [63,

64] Notably, a selective *in vivo* response is obtained due to disparities in the physiological characteristics of cancer cells compared to healthy cells. Solid tumors possess a complex vascular architecture, including hypoxic and low-pH regions absent in normal tissues, rendering cancer cells more vulnerable to temperature elevation. While most normal tissues can tolerate temperatures up to 44 °C for one hour, with the exception of nerve tissues showing heightened sensitivity. Hyperthermia triggers diverse cellular changes, such as protein unfolding, cytoskeletal disruption, organelle fragmentation, and altered nuclear processes, ultimately culminating in apoptosis induction. Additionally, hyperthermia induces the production of reactive oxygen species (ROS), further contributing to apoptosis induction. [65] Hyperthermia can be categorized based on the heated surface area or volume into: local hyperthermia, which targets small areas like localized tumors; regional hyperthermia, applied to larger areas such as entire organs or limbs; and whole-body hyperthermia, utilized for metastatic cancers that have spread throughout the body. Hyperthermia can be induced by different ways, such as electromagnetic radiation, laser application, therapeutic ultrasound, and the use of MNPs as heat mediators. Among these techniques, magnetically mediated hyperthermia is a good option due to its ability to provide more selective heating while minimizing side effects in surrounding tissues. [64] Magnetic hyperthermia, as illustrated in Figure 1.5, involves the injection of MNPs into the tumor region and the activation of them by an AC magnetic field, with the consequent release of thermal energy through hysteresis losses and Brownian relaxation. This technique is particularly advantageous for treating both superficial and deep cancers due to the ability of the applied magnetic field to penetrate tissues effectively. Additionally, magnetic hyperthermia is a viable approach for treating brain tumors due to the size of MNPs, which can easily pass through the blood-brain barrier. Moreover, magnetic hyperthermia offers distinct advantages over other hyperthermia methods: MNPs have the ability to be internalized by cells, facilitating direct heat delivery to them, and MNPs can be functionalized with molecules to enhance their affinity for cancer cells, promoting more targeted heat delivery and ensuring a more uniform local temperature distribution. [36]

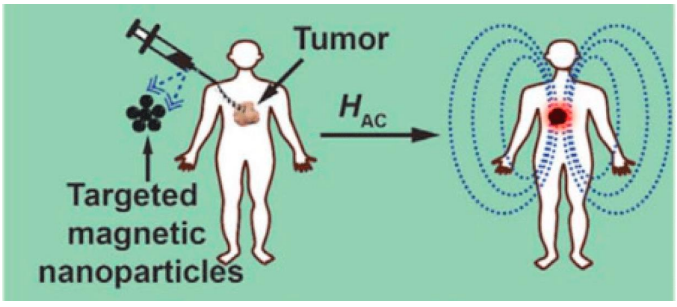



**Figure 1.5.** Schematic representation of the mechanism of action of magnetic hyperthermia. This image is extracted from ref. [30].

In 2003, the first clinical application of interstitial hyperthermia using MNPs for the treatment of human cancer was reported. In particular, magnetic fluid hyperthermia was employed as a potential minimally invasive therapeutic approach for prostate cancer, demonstrating the feasibility and tolerability of the technique in patients with recurrent prostate carcinoma. [66, 67] Subsequently, another significant clinical study focused on magnetic hyperthermia in combination with radiotherapy for the treatment of glioblastoma multiforme was conducted. A significant improvement of the survival time from the diagnosis of the glioblastoma recurrence was observed, attributable to thermo-/radiotherapy. [68]

#### AC magnetic field limitations

Increasing the amplitude $H_a$ and frequency $f$ of the applied magnetic field can enhance hysteresis losses up to saturation conditions. However, when patients are exposed to an AC magnetic field, it's essential to control parameters $H_a$ and $f$ to prevent the unwanted induction of eddy currents in the body. These currents can create side effects or hot-spots, potentially causing discomfort and tissue damage. To mitigate these effects, limits are imposed on the product $H_a \times f$. Initially, an upper limit of $4.85 \times 10^8$ A/ms, known as the Atkinson-Brezovich limit, was considered acceptable to avoid excessive resistive heating. [69] Subsequently, a less stringent criterion of $H_a \times f \leq 5 \cdot 10^9$ A/ms was proposed by Hergt and Dutz. [70, 71] The tolerability of these limits was demonstrated in early clinical trials on magnetic hyperthermia, where patients with various tumor types were exposed to a magnetic field of 100 kHz, with amplitudes ranging from 2.5 kA/m to 18 kA/m. [66–68] Therefore, it is important from an experimental standpoint to stay below this limit in order to conduct measurements that are compatible with the conditions applicable in clinical trials.
Therefore, it is crucial to take into account this safety limit of the product of $H_a \times f$ when evaluating the thermal efficiency of MNPs. Specifically, increasing the magnetocrystalline anisotropy of MNPs (i.e. doping with $Co^{2+}$) allows for higher coercive field. However, if the coercive field is too high, it becomes impossible to achieve saturation magnetization while keeping the field within the limit defined by Hergt-Dutz, thus preventing the full exploitation of heat generation potential. [62]

### 1.2.2 Magnetic oxygen loaded nanodroplets

In the last decades, there has been an increase in the study of nanomaterials for oxygen delivery to develop novel therapeutic treatments for hypoxic tissues due to various pathologies, such as cancer, diabetes, and infections. [72–77] Fluorocarbon compounds, characterized by linear, cyclic, or polycyclic hydrocarbons substituted with fluorine, have emerged as promising candidates for creating oxygen

delivery carriers in aqueous suspension like oxygen-loaded nanobubbles (OLNBs) or oxygen-loaded nanodroplets (OLNDs). Their stability, inertness, and ability in gas stabilization render them particularly well-suited for this purpose. [72, 73, 78–83] OLNBs and OLNDs exhibit variances in their physical states, with OLNBs existing in a gaseous state and OLNDs in a liquid state, determined by the boiling temperature of the fluorocarbon utilized in their synthesis. The majority of investigated OLNBs and OLNDs in the literature are synthesized with a perfluoropentane (PFP) and decafluoropentane (DFP) core, respectively. These distinct fluorocarbons exhibit different boiling points falling within the ranges of 28–32 °C for PFP and 51–55 °C for DFP. The release of oxygen from these systems tipically depends on the phenomenon of acoustic cavitation, wherein bubbles within a solution undergo growth and oscillation upon exposure to an ultrasound (US) field. The nature of cavitation, whether stable or inertial, depends on the applied acoustic pressure. Under low pressure conditions, cavitation remains stable, enabling bubbles to oscillate around their resonant size, thereby facilitating controlled oxygen release. Conversely, high pressure induces inertial cavitation, characterized by the occurrence of violent bubble collapse. [84, 85]
Liquid formulations of OLNDs offer a range of advantages over OLNBs. Notably, they show more effective oxygen release performance and exhibit a smaller size profile, potentially enabling them to cross the nano-scale interendothelial gaps commonly present in the fenestrated capillaries associated with tumor environments. [73, 80] OLNDs have the capacity to undergo acoustic cavitation following their vaporization into microbubbles (with diameters ranging from 10 to 100 $\mu$m) through interaction with an energy source, resulting in a localized temperature increase up to the boiling point of the fluorocarbon. Conventional techniques for triggering vaporization, such as acoustic droplet vaporization or optical droplet vaporization, employ US or optical stimuli. [86, 87]

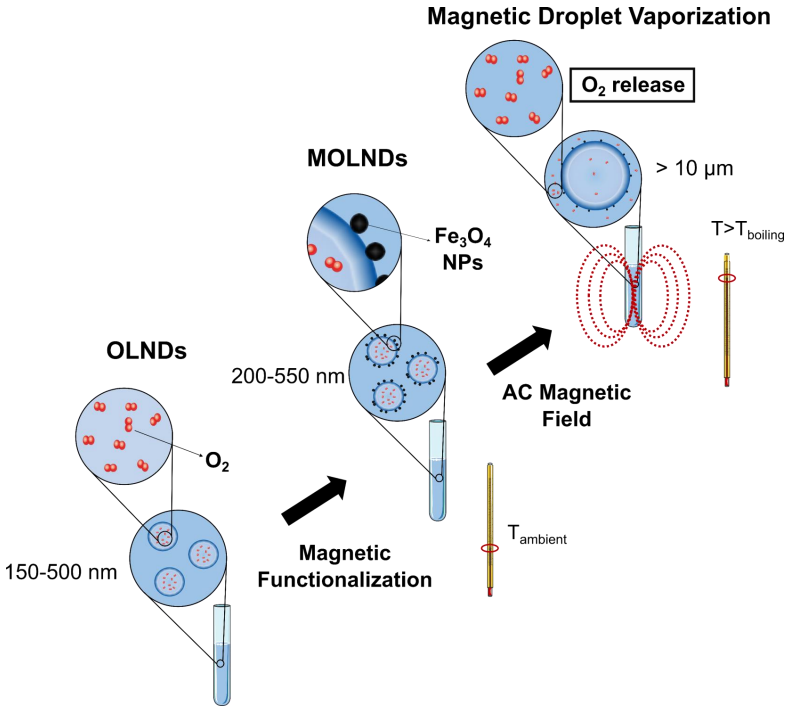



**Figure 1.6.** Diagram illustrating the magnetic decoration of oxygen-loaded nanodroplets with $Fe_3O_4$ NPs, followed by activation via AC magnetic field, leading to oxygen release through magnetic droplet vaporization. This Figure is reported in ref. [88].

Traditional methods inducing vaporization (i.e. US or optical stimuli) may encounter challenges in accessing deeper anatomical sites within the human body while simultaneously attempting to limit adverse effects. These limitations stem from both the penetration capability of the energy source employed and the properties of the tissue to be traversed. [89] One potential approach to surpassing this constraint involves exploiting the heat generated by magnetically functionalized OLNDs, tipically called magnetic oxygen-loaded nanodroplets (MOLNDs), when activated by an AC magnetic field. This strategy, illustrated in Figure 1.6, enables magnetic droplet vaporization, thereby triggering the release of oxygen. [89, 90] Magnetic functionalization can be achieved by decorating the surface of OLNDs with MNPs, resulting in the formation of MOLNDs. The benefit of employing magnetic fields as stimuli lies in their ability to penetrate the body without being affected by tissue properties, thereby enabling greater penetration depths to be achieved.
In recent years, only a limited number of studies have explored the mechanism of magnetic droplet vaporization, as well as the processes of functionalization and conjugation aimed at developing hybrid multi-responsive nanocarriers characterized by both acoustic and magnetic properties. [91] Although certain studies have investigated the utilization of magnetic droplet vaporization in alternative theranostic

nanosystems, including its role as heat mediators for magnetic hyperthermia treatment [90] or as contrast agents for US imaging [89], none of these investigations have examined its potential for oxygen delivery as a therapeutic method. Conversely, significant focus has been directed towards assessing the *in vitro* biocompatibility, cellular uptake, and magnetic hyperthermia effectiveness of MOLNDs. [92–96] Due to the gaps in the existing literature, this topic emerges as highly interesting for further exploration and investigation.

### 1.2.3 Radical polymerization of hydrogels induced by magnetic nanoparticles

Radical polymerizations enable the production of a diverse range of materials suitable for various applications, ranging from biological to technological and industrial sectors. [97] Despite the vast array of materials produced, all radical polymerization procedures entail, at minimum, a monomer equipped with appropriate functional groups (such as acrylate or vinyl) and a radical initiator. [98] The latter species generate free radicals through decomposition under specific conditions, initiating a cascade process that leads to the formation of the polymeric chain. Indeed, the initial radical attaches to a monomer unit, thereby generating new radical species that can subsequently bond with other monomers and elongating the polymer chain, as shown in Figure 1.7.

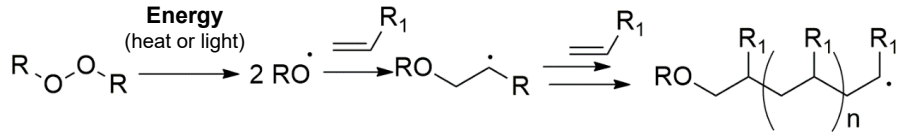



**Figure 1.7.** General reaction of free radical polymerizations.

Initiation represents a crucial factor in determining the ultimate properties of the polymer: employing identical monomer compositions, the structural characteristics of the material can be adjusted through varied reaction conditions. [99–101] The primary techniques for initiating radical polymerization typically involve the use of initiators that generate radicals either through heating ("thermal polymerization") or exposure to light irradiation ("photopolymerization"). [102] Alternative methods of initiation may involve electrolysis, microwaves, or the application of ultrasound. [103–105] Conventional thermal heating represents the simplest means to induce radical polymerization and produce bulk materials, requiring no specialized equipment or reactors, but using heating plates or ovens. When scaling up the polymerization process, challenges may arise due to the unavoidable thermal gradient within the material volume during polymerization, potentially resulting in material inhomogeneity. Conversely, photopolymerization offers an approach to confine the

reaction within a designated volume (illuminated by light), allowing for its utilization in various applications ranging from large-area coatings to photolithographic techniques, with resolutions extending down to the nanometer scale. [106–108] Photopolymerization can be directly utilized for shaping polymeric materials in 3D and in biological settings, through the careful selection of the photoinitiator and the wavelength used for activation. [109–111] As a result, this approach is hindered by inadequate light penetration within the monomeric solution and the requirement for a transparent environment, consequently restricting the size and composition of the monomers as well as the type of substrate or vessel in which the process can occur. Certain constraints of both methods can be addressed through frontal polymerization process. This process is triggered solely by applying a localized stimulus to the monomer solution (either heating or light irradiation), after which it becomes self-sustaining throughout the entire volume due to the locally released heat during radical addition. [112–114] For these reasons, the ability to achieve bulk material, spatial selectivity, and *in situ* processing within an opaque (including biological) environment remains challenging to integrate with all the previously mentioned techniques.

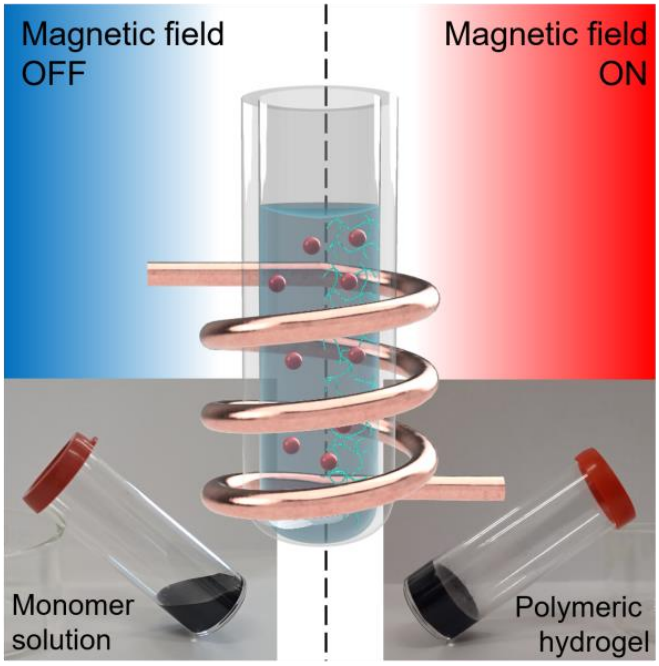



**Figure 1.8.** Schematic representation of radical polymerization induced by MNPs heating. This Figure is reported in ref. [115].

Previous studies have demonstrated the utilization of indirect heating methods, such as electromagnetic induction, to accomplish these goals. In this approach, polymerization may be initiated by an AC magnetic field through the interaction

of susceptors and resistive heating elements added within the monomeric formulation, such as metallic additives or metal grids. [116–118] Another adaptable system for achieving wireless heating involves exploiting the heat released by MNPs when exposed to an AC magnetic field, as schematized in Figure 1.8. [119]
Therefore, the induction of radical polymerization by MNPs can serve as an alternative for industrial-scale hydrogel production and has potential applications in the biomedical field. Specifically, magnetic hydrogels can be used to create phantoms that mimic the properties of tissues with dispersed MNPs. These phantoms can be useful for calibrating instruments for magnetic hyperthermia or for evaluating the heating properties of MNPs in environments more similar to physiological conditions, where factors such as limited mobility also play a role. [120–122]

## 1.3 Outline of the Thesis

This thesis, conducted at the Istituto Nazionale di Ricerca Metrologica (INRiM) in Torino, aims to develop magnetic nanoparticles (MNPs) with good heating efficiency, following exposure to an AC magnetic field, and to employ the generated heat for various applications, including magnetic hyperthermia on cell cultures, oxygen release using thermosensitive nanovectors, and the induction of acrylamide radical polymerization. We employ co-precipitation synthesis to produce magnetite ($Fe_3O_4$) and cobalt ferrite ($CoFe_2O_4$) NPs, subsequently functionalizing their surfaces with coating agents to improve both the heating efficiency and colloidal stability. Following synthesis, the MNPs are characterized to determine their dimensional, physicochemical, magnetic, and heating properties and their cytotoxicity. Subsequently, the heat release from the MNPs is utilized to assess its effects on cell cultures, to induce vaporization and consequent oxygen release from synthesized magnetic oxygen loaded nanodroplets, and finally, to induce radical polymerization to obtain polyacrylamide hydrogels.

In Chapter 1, we have provided an overview of nanomaterials, with a particular focus on MNPs. We have outlined their main characteristics, the synthesis methodologies employed for their fabrication, and their widespread biomedical applications, focusing on magnetic hyperthermia. Furthermore, we have reported an overview on nanocarriers employed for oxygen delivery (OLNDs) and polymer hydrogels with biomedical applications, exploring the potential of integrating MNPs into these systems to enhance their properties.

In Chapter 2, we introduce the methodologies employed for synthesizing $Fe_3O_4$

and $CoFe_2O_4$ NPs, encompassing the obtained results in terms of structural, morphological, dimensional, magnetic, and thermometric characterization. This detailed exploration constitutes a fundamental foundation for elucidating the properties of the synthesized nanoparticles, which will be employed for various applications in the subsequent chapters.

In Chapter 3, we describe surface coating treatments applied to $Fe_3O_4$ NPs employing diverse coating agents, with the aim of increasing the heating efficiency of the NPs. Subsequently, we present the results obtained from a comprehensive characterization conducted to assess the effectiveness of the surface coating. Finally, we compare the magnetic and thermal properties of untreated and treated NPs to evaluate the impact of the coating.

In Chapter 4, we present investigations focused on evaluating the biocompatibility and potential cytotoxic effects of $Fe_3O_4$ and $CoFe_2O_4$ NPs at varying concentrations, both with and without citrate coating, which has shown a significant effect in enhancing the SLP of the NPs. Subsequently, we introduce a novel protocol for conducting *in vitro* magnetic hyperthermia experiments using $Fe_3O_4$ NPs on adherent cultures of a human lung cancer cell line.

In Chapter 5, we focus on the preparation and characterization of magnetic oxygen loaded nanodroplets (MOLNDs), achieved by decorating OLNDs with $Fe_3O_4$ NPs. In particular, we synthesize four distinct samples of OLNDs using two types of coatings, chitosan or dextran, and two types of fluorocarbon cores, decafluoropentante (DFP) or perfluoropentane (PFP). Then, we present results obtained from the characterization conducted to assess the magnetic decoration. Subsequently, we describe experiments carried out to evaluate the oxygen release induced by AC magnetic field exposure. Finally, we report *in vitro* cytotoxicity tests conducted to investigate the biocompatibility of these nanohybrid systems.

In Chapter 6, we present an innovative method for inducing radical polymerization of magnetic hydrogels, which are based on polyacrylamide, by harnessing the thermal energy released by $CoFe_2O_4$ NPs. Subsequently, we compare the properties of the hydrogels polymerized via AC magnetic field with those polymerized through conventional heating methods. Finally, we discuss specific experiments aimed at polymerizing magnetic hydrogels in a selective volume within a thermosensitive environment, as well as polymerizing non-magnetic hydrogels using MNPs concentrated in a small volume as a heat generator.

# Chapter 2

# Synthesis and characterization of magnetic nanoparticles

In this Chapter, MNPs with distinct compositions are synthesized using chemical methods and comprehensively characterized in terms of their structural, morphological, dimensional, magnetic, and heating properties. The synthesized samples consist of $Fe_3O_4$ and $CoFe_2O_4$ NPs. Part of the content of this Chapter has been published in:

[38] *M. Vassallo, D. Martella, G. Barrera, F. Celegato, M. Coïsson, R. Ferrero, E. S. Olvetti, A. Troia, H. Sözeri, C. Parmeggiani, D. S. Wiersma, P. Tiberto, A. Manzin. Improvement of Hyperthermia Properties of Iron Oxide Nanoparticles by Surface Coating.* ACS Omega, ***2023**, 8(2): 2143–2154.*

In the Chapter 3, $Fe_3O_4$ NPs synthesized in this phase of the research undergoing a surface treatment aimed at enhancing their heating efficiency by surface coating with various functionalizing agents, sodium citrate and carboxymethyl cellulose. Subsequently, these MNPs have been employed to explore various biomedical applications. These applications include magnetic hyperthermia and drug delivery, as detailed in Chapter 4 and Chapter 5, respectively. Meanwhile, $CoFe_2O_4$ NPs have been investigated for polymerization processes exploiting magnetic hyperthermia, as outlined in Chapter 6.

## 2.1 Materials and Methods

### 2.1.1 Reagents

Iron(II) chloride tetrahydrate ($FeCl_2 \cdot 4H_2O$), iron(III) chloride hexahydrate ($FeCl_3 \cdot 6H_2O$), cobalt(II) nitrate hexahydrate ($Co(NO_3)_2 \cdot 6H_2O$), iron(III) nitrate nonahydrate ($Fe(NO_3)_3 \cdot 9H_2O$), and ammonium hydroxide solution ($NH_4OH$, 30%)

were purchased from Sigma-Aldrich (St Louis, MO). All chemicals were used without further purification.

### 2.1.2 Preparation of $Fe_3O_4$ nanoparticles

For the synthesis of $Fe_3O_4$ NPs the co-precipitation method was employed. [37, 38]
Iron(II) chloride tetrahydrate and iron(III) chloride hexahydrate were dissolved in deionized water with a molar ratio of $Fe^{2+}/Fe^{3+}$ equal to 1:2 and an iron concentration of 0.5 M. The reaction was carried out in a total volume of 100 mL of water under vigorous stirring and nitrogen throughout. Following complete dissolution, the mixture was heated up to 75 °C, and precipitation was achieved by adding a 15 mL solution of ammonium hydroxide (30%) dropwise until reaching a pH of 8.0–8.5. The precipitate was then heated to 85 °C for 1 h, washed with deionized water until reaching a neutral pH, and magnetically decanted to separate the synthesized $Fe_3O_4$ NPs.

### 2.1.3 Preparation of $CoFe_2O_4$ nanoparticles

For the synthesis of $CoFe_2O_4$ the co-precipitation method was employed. [39]
Cobalt(II) nitrate hexahydrate (2.8 g) and iron(III) chloride hexahydrate (5.4 g) were dissolved in deionized water (300 mL) with a 1:2 molar ratio. Under vigorous stirring, an aqueous solution of sodium hydroxide (10 M) was added to reach a pH of 13. The reaction mixture was heated to 100 °C under stirring and nitrogen flow. After 30 min, iron(III) nitrate nonahydrate (3.9 g) was added to the solution to achieve a $Co^{2+}/Fe^{3+}$ molar ratio of 1:3. The reaction was carried on for another 30 min. After cooling to room temperature, the precipitate obtained was magnetically decanted and washed several times using deionized water until reaching a neutral pH.

### 2.1.4 Characterization of magnetic nanoparticles

#### Morphological, structural and dimensional characterization

The morphology and the size distribution of MNPs were evaluated by transmission electron microscopy (TEM) at TUBITAK (Turkey) using a JEM-2100 transmission electron microscope (JEOL, Tokyo, Japan). TEM images were analyzed using the open-source software ImageJ [123] and the mean size of MNP samples was extrapolated through statistical analysis on 150 MNPs.
The crystal phase of the MNP samples was analyzed by X-ray diffractometry (XRD) using a X'Pert PRO MPD diffractometer (Malvern Panalytical, Malvern, UK) with

a Cu K$\alpha$ radiation ($\lambda$ = 1.541874 Å) in the $2\theta$ range from 8 to 100°. The dried nanopowders were placed in the cavity of a silicon zero-background sample holder and analyzed in Bragg-Brentano configuration.
The atomic ratio between Fe and Co in cobalt-ferrite NPs was estimated by standardless semi-quantitative analysis through Energy Dispersive Spectrometry, coupled to a Scanning Electron Microscope (SEM-EDS), after deposition of the MNPs on the carbon adhesive tape used for electron microscopy.
The hydrodynamic size distribution of the MNPs was investigated at room temperature by dynamic light scattering (DLS) using the Zetasizer Ultra instrument (Malvern Panalytical, Malvern, UK). DLS results were obtained with at least three scans for each measurement. The above instrument was also used to evaluate the surface charge of the MNPs by $\zeta$ potential measurements conducted on the magnetic suspensions at neutral pH. The $\zeta$ potential results were obtained through a minimum of three scans for each measurement.

### Magnetic characterization

The static hysteresis loops of dry samples were measured at room temperature by vibrating sample magnetometry (VSM) using a 7410 magnetometer (Lake Shore, Westerville, Ohio, USA). The characterization was performed under direct current (DC) magnetic fields, varying from −1350 to 1350 kA/m in steps of 0.8 kA/m.
The magnetic properties of $Fe_3O_4$ NPs were also analyzed under dynamic conditions to better understand the physical mechanisms of magnetic losses in the samples when exposed to an AC magnetic field. The measurements were performed using a custom-built setup developed at INRIM [124] with a frequency of 69 kHz and an amplitude selectable up to 38 kA/m, which are conditions comparable to hyperthermia treatments. The hysteresis loops were recorded on liquid samples of $Fe_3O_4$ NPs with a concentration of approximately 10 mg/mL.

### Thermometric characterization

To evaluate the heating efficiency of MNPs, thermometric measurements were conducted with a custom-built setup, developed at INRIM and depicted in Figure 2.1. [125] The aqueous suspensions of MNPs, with a concentration of about 12 mg/mL for $Fe_3O_4$ NPs and 8 mg/mL for $CoFe_2O_4$ NPs, were poured into a test tube and then exposed to a uniform AC magnetic field with a frequency of 100 kHz and an amplitude selectable in the range 24–48 kA/m, thus fulfilling the Hergt–Dutz limit. [70, 71] The heating time was fixed to 1 h for each measurement. A fiber optic thermometer (Osensa Innovation, Burnaby, CAN), with the sensing point placed at the suspension center, was used to measure the local temperature during the heating and cooling transients. Then, the recorded curves of the temperature time evolution were processed using a fitting function derived from an analytical

thermodynamic model, [125] allowing the estimation of the SLP of MNPs.

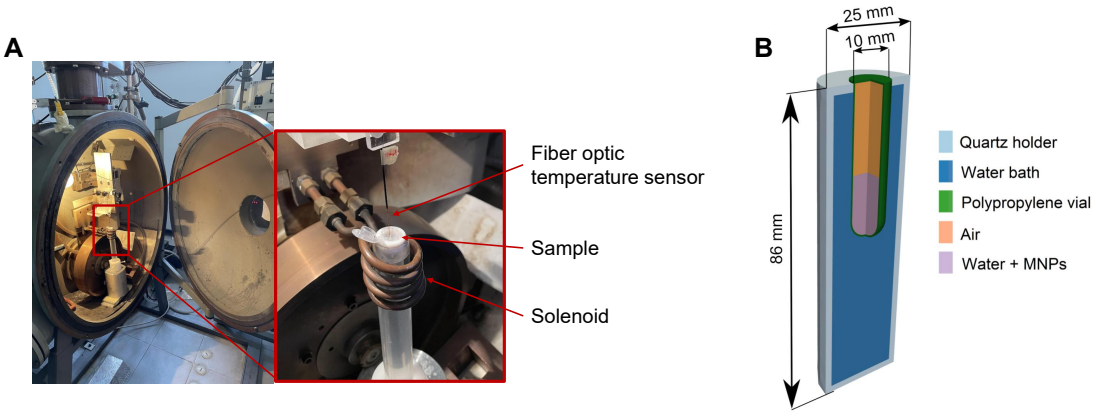



**Figure 2.1.** (**A**) Picture of the thermometric setup and (**B**) schematic of the sample container used for the determination of the SLP of MNPs.

## 2.2 Results

### 2.2.1 Magnetic nanoparticle synthesis

An illustration of the $Fe_3O_4$ NPs synthesis is shown in Figure 2.2. The synthesis is performed with a large-scale process involving co-precipitation in an alkaline environment. Starting from a mixture containing $Fe^{2+}$ and $Fe^{3+}$, the NPs are precipitated with ammonium hydroxide solution and heated up to 85 °C. After magnetic recovery and washing with water, a large quantity of MNPs is obtained, corresponding to a yield of 70 % (mass of 1.7 g). The reproducibility of the co-precipitation method is verified, by synthesizing a second batch of $Fe_3O_4$ NPs using the same synthesis conditions described above.

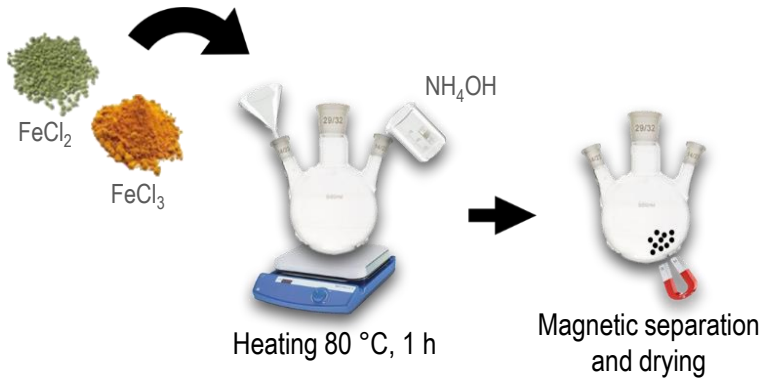



**Figure 2.2.** Schematic representation of the chemical preparation of $Fe_3O_4$ NPs *via* co-precipitation.

Additionally, the synthesis of $CoFe_2O_4$ NPs involves a co-precipitation process in an alkaline environment, as depicted in Figure 2.3. Briefly, a mixture containing $Co^{2+}$ and $Fe^{3+}$ ions is precipitated by the addition of a NaOH solution. The reaction proceeds for 1 h at 100°C. Subsequently, the NPs are washed to achieve a neutral pH using magnetic decantation. Furthermore, the synthesis is scaled up to produce 2.5 g of $CoFe_2O_4$ NPs.

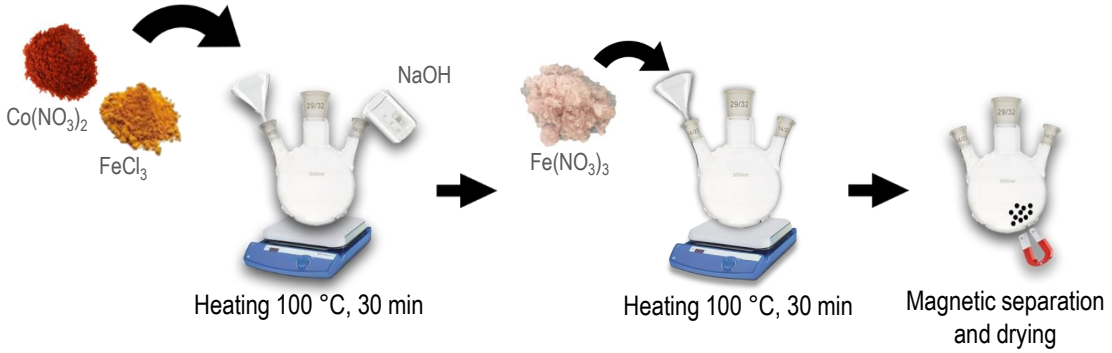



**Figure 2.3.** Schematic representation of the chemical preparation *via* co-precipitation of $CoFe_2O_4$ NPs.

## 2.2.2 Magnetic nanoparticle characterization

### Physicochemical characterization

Representative TEM images and size distributions of $Fe_3O_4$ and $CoFe_2O_4$ NPs are reported in Figures 2.4 and 2.5 NPs, respectively. Both samples exhibit a quasi-spherical shape and a highly uniform size distribution, as illustrated by the

histograms. These histograms result from a statistical analysis of TEM images, performed on 150 NPs using ImageJ software. [123] $Fe_3O_4$ NPs have a mean diameter of 10.9 nm with a standard deviation of 2.6 nm, while $CoFe_2O_4$ NPs have a mean diameter of 13.7 nm with a standard deviation of 1.2 nm.

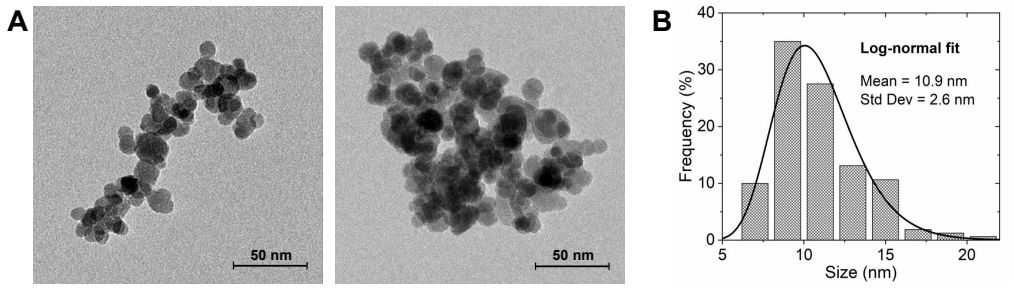



**Figure 2.4.** (**A**) Representative TEM images and (**B**) size distribution histogram (derived from statistical analysis on TEM images) of $Fe_3O_4$ NPs.

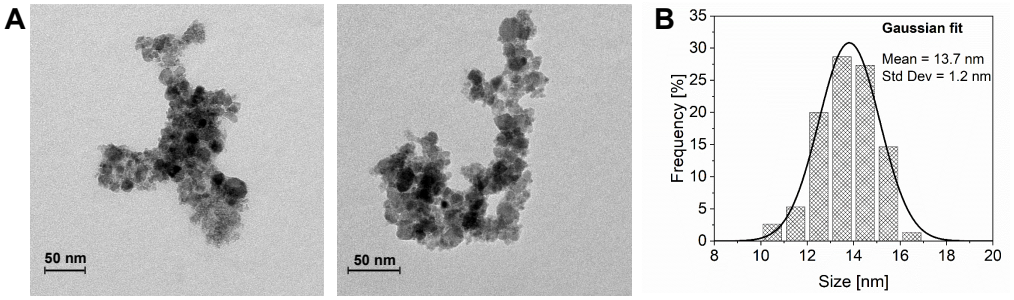



**Figure 2.5.** (**A**) Representative TEM images and (**B**) size distribution histogram (derived from statistical analysis on TEM images) of $CoFe_2O_4$ NPs.

The XRD pattern for $Fe_3O_4$ NPs is shown in Figure 2.6, revealing a crystalline phase with main diffraction peaks indexed as (220), (311), (400), (511), and (440), such as for the cubic spinel structure of $Fe_3O_4$ (ICDD PDF card no. 01-075-0033), whose characteristic diffraction peaks are indicated with red vertical lines. In addition, the XRD pattern of $Fe_3O_4$ NPs is compared with that of $\gamma$-$Fe_2O_3$ (ICDD PDF card no. 00-039-1346) to assess the presence of other iron oxides, as illustrates in Figure 2.6 with green vertical lines. This comparison confirms the absence of the $\gamma$-$Fe_2O_3$ phase. Specifically, the characteristic additional peaks of $\gamma$-$Fe_2O_3$ at around 15°, 24°, and 26° are not observed. [126, 127]

The XRD pattern of $CoFe_2O_4$ NPs is shown in Figure 2.7, revealing a crystalline phase with the main diffraction peaks compatible with the ones of cubic iron-spinel phases like magnetite and its substituted relatives such as $CoFe_2O_4$, where all $Fe^{2+}$ ions have been replaced by $Co^{2+}$ ions. Since these two phases have the same cubic structure and very similar lattice parameters, their XRD pattern is almost identical,

as shown in Figure 2.6 and Figure 2.7. Consequently, distinguishing cobalt ferrite from magnetite based on X-ray diffraction is very difficult. For this reason, the actual presence and concentration of Co ions in the synthesized NPs are checked and confirmed by SEM-EDS elemental semi-quantitative analysis: the atomic ratio between Co and Fe, turned out to be 1:3, corresponding to the one used in the synthesis process (detailed in Section 2.1.3).

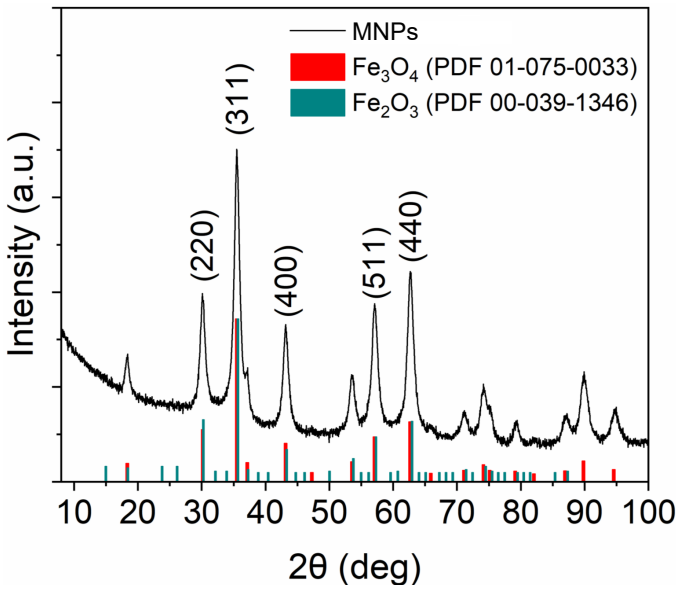



**Figure 2.6.** XRD pattern of $Fe_3O_4$ NPs, reporting the square root of the intensities. The characteristic diffraction peaks of $Fe_3O_4$ (ICDD PDF card no. 01-075-0033) and $\gamma$-$Fe_2O_3$ (ICDD PDF card no. 00-039-1346) are indicated, respectively, with the red and green vertical lines.

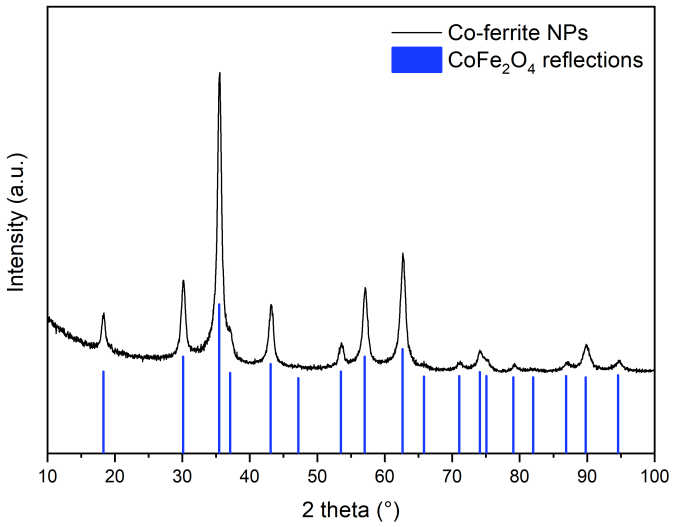



**Figure 2.7.** XRD pattern of $CoFe_2O_4$ NPs, reporting the square root of the intensities. The characteristic diffraction peaks of $CoFe_2O_4$ are indicated with the blue vertical lines.

The hydrodynamic size distributions of $Fe_3O_4$ NPs and $CoFe_2O_4$ NPs obtained by DLS are shown in Figure 2.8A and Figure 2.8B, respectively. Additionally, the mean hydrodynamic size, the relative polidispersity index (PDI), and the $\zeta$ potential value of both samples are reported in Table 2.1. DLS enables the characterization of the hydrodynamic behavior of NPs, providing insights into the sizes of their aggregates. The average hydrodynamic size of the $Fe_3O_4$ NPs is approximately 135 nm, while for the $CoFe_2O_4$ NPs, it is around 75 nm. The values of the polydispersity index obtained for the samples indicate a fairly uniform and narrow size distribution. The $\zeta$ potential measurements offer insights into the surface charge of NPs. It is established that when the absolute values exceed 30 mV, the suspension demonstrates excellent colloidal stability and exhibits a minimal tendency to flocculate. [128] The $\zeta$ potential values obtained for $Fe_3O_4$ and $CoFe_2O_4$ NPs are around -25 mV and -30 mV, respectively, in agreement with the values reported in the literature. [129, 130] The $CoFe_2O_4$ NP sample exhibits smaller aggregates compared to the $Fe_3O_4$ sample, potentially attributed to the slightly higher absolute value of the $\zeta$ potential that leads to enhanced colloidal stability of the $CoFe_2O_4$ sample. [128]

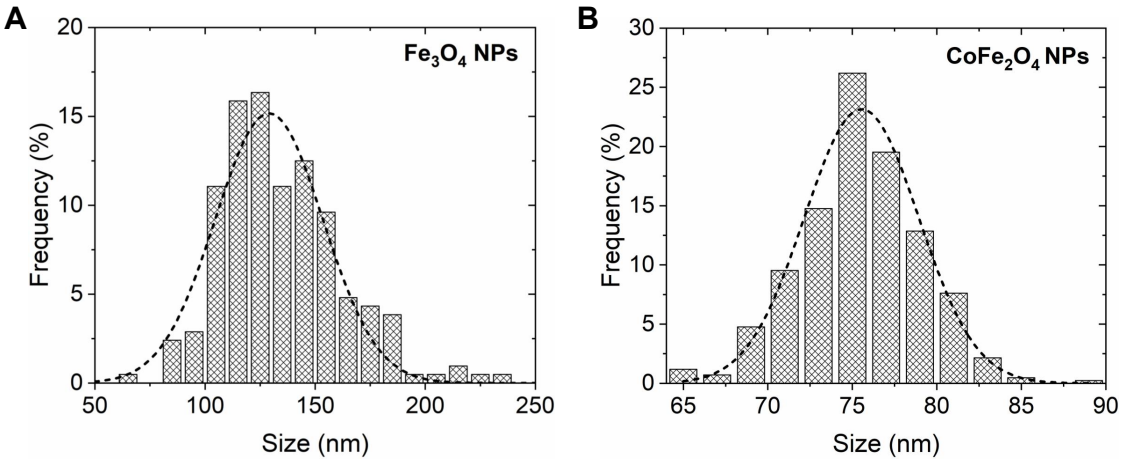



**Figure 2.8.** DLS particle size distributions for (**A**) $Fe_3O_4$ NPs and (**B**) $CoFe_2O_4$ NPs. The dashed curves represent the Gaussian fits of the distributions, which serve as a guide to the eye.

**Table 2.1.** Mean hydrodynamic size, PDI and $\zeta$ potential values for the $Fe_3O_4$ NPs and $CoFe_2O_4$ NPs.

| **Sample** | **Mean Hydrodynamic Size** [nm] | **PDI** | **$\zeta$ potential** [mV] |
|---|---|---|---|
| $Fe_3O_4$ NPs | 135 ± 35 | 0.277 | -24.8 ± 0.5 |
| $CoFe_2O_4$ NPs | 76 ± 3.6 | 0.246 | -29.6 ± 0.7 |

### Magnetic characterization

The static magnetic behaviour of the prepared $Fe_3O_4$ and $CoFe_2O_4$ NPs are investigated using VSM. The measurements are conducted at room temperature on the samples in powder form. The measured magnetic signal is normalized to the mass of magnetic material in both samples, and the obtained curves for $Fe_3O_4$ and $CoFe_2O_4$ NPs are presented in Figure 2.9A and Figure 2.9B, respectively. The saturation magnetization ($M_S$) and coercivity ($H_C$) values are provided in Table 2.2.

For the $Fe_3O_4$ NPs (Figure 2.9A), the magnetization reversal exhibits a sigmoidal trend with a gradual approach to saturation value, which is not fully attained even at the maximum applied field. The $M_S$ of $Fe_3O_4$ NPs is approximately 74 $Am^2/kg$, lower than the bulk magnetite value of 92 $Am^2/kg$. [131] This discrepancy may be attributed to effects such as canting or disorder of the magnetic spins at the surface of the $Fe_3O_4$ NPs. [132, 133] Furthermore, this value closely aligns with those reported for other $Fe_3O_4$ NPs in the literature [134], as well as for commercial magnetite fine powder (84 $Am^2/kg$). [135]

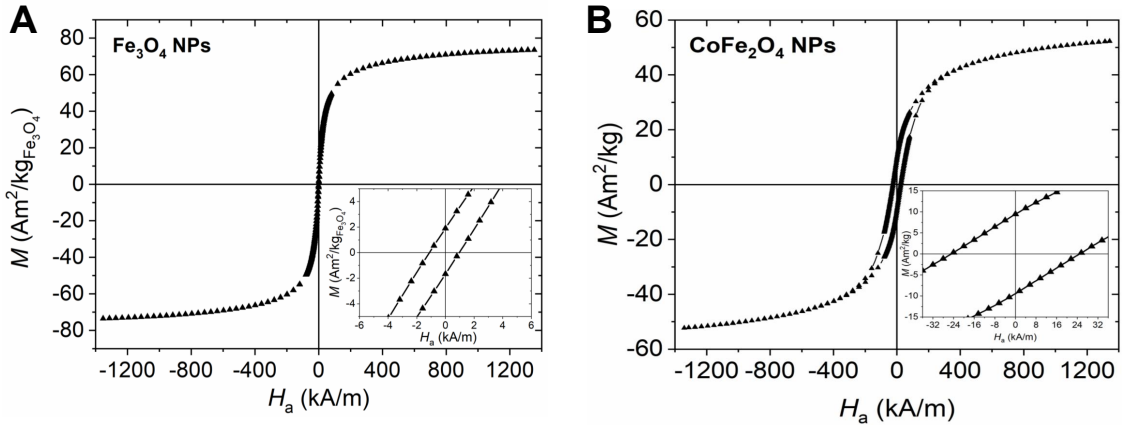



**Figure 2.9.** Room-temperature $M(H)$ curves of (**A**) $Fe_3O_4$ NPs and (**B**) $CoFe_2O_4$ NPs in dry form. The magnetization values are normalized to the MNP mass and the portion of the hysteresis loops around remanent magnetization and coercivity is shown zoomed in the inset.

**Table 2.2.** Values of saturation magnetization ($M_S$), remanent magnetization ($M_R$), and coercivity ($H_C$) of $Fe_3O_4$ NPs and $CoFe_2O_4$ NPs at room temperature. The magnetization values are normalized to the MNP mass.

| **Sample** | $M_S$ [$Am^2/kg$] | $M_R$ [$Am^2/kg$] | $H_C$ [kA/m] |
|---|---|---|---|
| $Fe_3O_4$ NPs | 73.5 | 1.8 | 1.0 |
| $CoFe_2O_4$ NPs | 52.3 | 10.6 | 24.7 |

Moreover, a hysteresis behavior is noticeable at low applied magnetic fields, resulting in a small coercivity ($H_C$) of approximately 1 kA/m (inset of Figure 2.9A). These characteristics suggest that the sample primarily consists of interacting superparamagnetic nanoparticles. This hypothesis is corroborated by TEM and DLS results. On one side, the TEM size distribution (see Figure 2.4B) indicates that the NPs have an average diameter of approximately 10 nm, mainly below the critical value ($d_C$) at which the transition from superparamagnetism to ferromagnetism is expected to occur. In particular, $d_C$ is estimated in the range of 17–21 nm, when considering the common values of effective anisotropy constant for $Fe_3O_4$ ($(2-4)\cdot 10^4 J/m^3$). [136–138] Only a small tail of the size distribution exceeds the evaluated $d_C$ values. Consequently, a superparamagnetic regime should be expected for practically all the single NPs, in which the $M(H)$ curve follows the non-hysteretic Langevin function (i.e., zero coercivity and zero remanence). On the other hand, the NP arrangement in aggregates, as revealed by the TEM images (Figure 2.4A) and DLS size distribution (Figure 2.8A), leads to the formation of

magnetic structures with an effective diameter larger than $d_C$, in which the magnetic moments respond coherently to the applied magnetic field, thus inducing the small hysteresis observed under static conditions. [139]
The magnetization curve of $CoFe_2O_4$ NPs (Figure 2.9B) presents a sigmoidal shape, with a slower approach to saturation compared to $Fe_3O_4$ NPs, and complete saturation is not achieved at higher values of applied magnetic field. Specifically, at an applied magnetic field of 1300 kA/m, the $M_S$ is approximately 52 $Am^2/kg$, lower than the bulk cobalt ferrite value of 80 $Am^2/kg$. This decrease in $M_S$ is attributed to magnetic moment disorder at the surface of the NPs, as observed in $Fe_3O_4$ NPs as well. [131] Analysis of the $M(H)$ curve reveals a hysteretic behavior in $CoFe_2O_4$ NPs, with a coercivity of approximately 25 kA/m. These results suggest that the sample consists of interacting superparamagnetic NPs, as previously explained for $Fe_3O_4$ NPs. Indeed, the NPs have an average diameter of about 14 nm, as shown in the TEM analysis (Figure 2.5), which is smaller than the $d_C$. Additionally, interactions among the $CoFe_2O_4$ NPs are further confirmed by the DLS size distribution (Figure 2.8B), demonstrating the formation of aggregates with dimensions ranging from 70 to 85 nm.

### Thermometric characterization

The heating properties of the synthesized $Fe_3O_4$ and $CoFe_2O_4$ NPs are investigated by performing thermometric measurements with a custom-built setup, detailed in Figure 2.1. The characterization involves liquid suspensions housed in a polypropylene test tube immersed in a water bath held within a quartz holder. Figure 3.10 depicts the heating and cooling transients recorded with a fiber optic probe for aqueous solutions containing $Fe_3O_4$ and $CoFe_2O_4$ NPs. These thermal profiles are recorded after exposing for 60 min the NP samples to an AC magnetic field with a frequency ($f$) of 100 kHz and a peak amplitude ($\hat{H}_a$) in the range 24-48 kA/m, thus adhering to the Hergt–Dutz limit. [70, 71] The NP concentration used was 12 mg/mL and 8 mg/mL, respectively, for $Fe_3O_4$ and $CoFe_2O_4$ NPs to ensure both the stability of the magnetic solution and the maintenance of temperature within an appropriate range during the measurements. Utilizing an analytical thermodynamic model [125] that accounts for the various heat exchange mechanisms within the experimental setup (detailed in Section 2.1.4), the experimental curves were fitted to estimate the SLP of the NPs as an indicator of their heating efficiency.

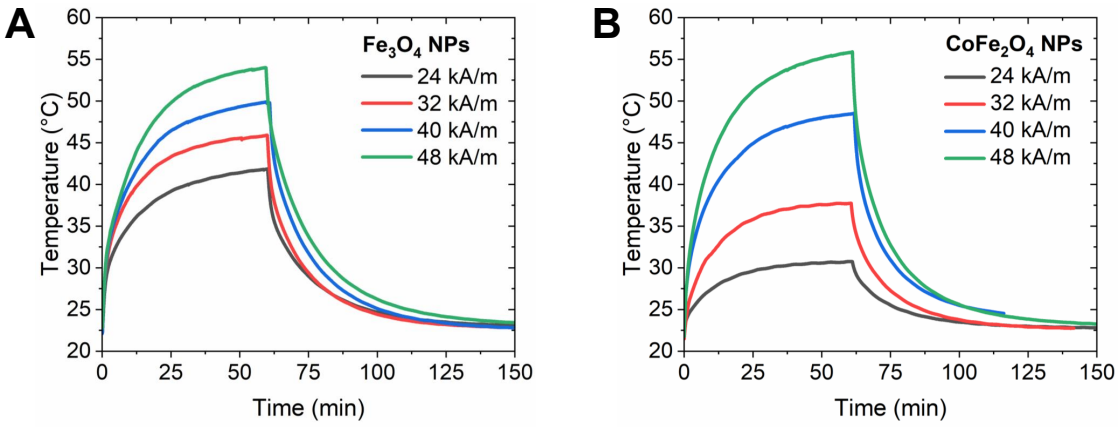



**Figure 2.10.** Time evolutions of the temperature of the magnetic suspensions containing (**A**) $Fe_3O_4$ and (**B**) $CoFe_2O_4$ NPs following the application of an AC magnetic field with different peak amplitudes $\hat{H}_a$ variable in the range 24-48 kA/m and frequency $f$ fixed to 100 kHz.

The SLP values, obtained by fitting the experimental data and validated through numerical modeling (detailed in Appendix 6.3), are shown in Figure 2.11 and Table 3.3. The results obtained reveal the dependence of SLP on the $\hat{H}_a$ for both investigated samples. Particularly noteworthy is the observation that at a higher peak amplitude of 48 kA/m, the SLP values are approximately 86 W/g for $Fe_3O_4$ NPs and 106 W/g for and $CoFe_2O_4$ NPs.

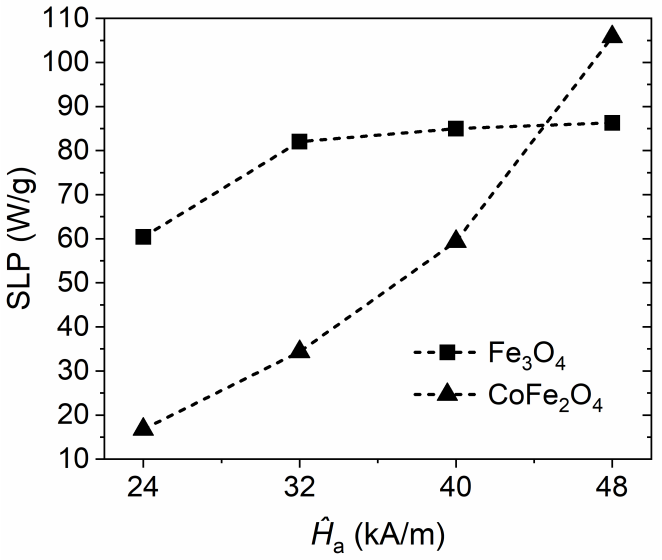



**Figure 2.11.** SLP values for $Fe_3O_4$ and $CoFe_2O_4$ NPs obtained at different peak amplitudes $\hat{H}_a$ of the AC magnetic field, fixing the frequency $f$ to 100 kHz.

**Table 2.3.** SLP values for $Fe_3O_4$ and $CoFe_2O_4$ NPs, obtained at different peak amplitudes $\hat{H}_a$ of the AC magnetic field (24-48 kA/m), setting the frequency $f$ at 100 kHz.

| **Sample** | $\hat{H}_a$ | | | |
|---|---|---|---|---|
| | 24 kA/m | 32 kA/m | 40 kA/m | 48 kA/m |
| $Fe_3O_4$ | 60.4 | 82.0 | 85.0 | 86.3 |
| $CoFe_2O_4$ | 16.8 | 34.3 | 59.3 | 105.8 |

## 2.3 Conclusions

In this Chapter, spherical-shaped $Fe_3O_4$ and $CoFe_2O_4$ NPs with an average size of approximately 10 and 14 nm, respectively, were synthesized using the co-precipitation method. The obtained samples were thoroughly investigated in terms of morphology, structure, size, magnetic properties, and heating properties for potential applications in magnetic hyperthermia, with a focus on thermal efficiency. The $Fe_3O_4$ NPs exhibit superparamagnetic behavior under static conditions and demonstrate a SLP around 86 W/g when subjected to an AC magnetic field of 48 kA/m, consistent with literature data for MNPs with similar characteristics. In contrast, the $CoFe_2O_4$ NPs display hysteretic behavior with a coercive field of 25 kA/m, attributed to the increased magnetocrystalline anisotropy compared to iron oxide NPs. Despite this increase in magnetocrystalline anisotropy and coercive field in $CoFe_2O_4$ NPs, enhanced SLP compared to $Fe_3O_4$ NPs is observed only at the highest peak amplitude value (48 kA/m), reaching 106 W/g. This phenomenon occurs because, at lower AC magnetic fields, saturation magnetization is not achieved, and consequently, the thermal potential of these MNPs cannot be fully exploited. Furthermore, the study highlights the simplicity and reproducibility of the NP synthesis approach employed, which does not require pressure control or high boiling point solvents. This approach represents a significant step towards the reproducibility of preparation procedures in standard chemical laboratories and underscores the potential scalability of the process, as demonstrated here on a gram scale.
In the following Chapters, these MNPs will be utilized for various applications exploiting their ability to generate heat when exposed to an AC magnetic field. Firstly, the $Fe_3O_4$ NPs will undergo surface coating treatment to enhance their thermal efficiency. Subsequently, these MNPs will be characterized in terms of biocompatibility and utilized for *in vitro* tests of magnetic hyperthermia and experiments of oxygen drug delivery. Finally, the $CoFe_2O_4$ NPs will be employed to induce the radical polymerization of polyacrylamide hydrogels.

# Chapter 3

# Influence of surface coating on the hyperthermia properties of $Fe_3O_4$ nanoparticles

In this Chapter, we investigate surface treatments applied to $Fe_3O_4$ NPs employing diverse coating agents, namely sodium citrate and carboxymethyl cellulose (CMC), with the objective of enhancing the thermal efficiency of the NPs. Following the application of these treatments, the resultant samples undergo comprehensive characterization to evaluate the effectviness of the surface coating using different techniques, such as Fourier Transform Infrared Spectroscopy (FTIR), Thermogravimetric Analysis (TGA), and DLS. Subsequently, the NPs are characterized in terms of their magnetic and thermal properties to assess the effects of the coating on these properties.

Part of the content of this chapter has been published in:

[38] *M. Vassallo, D. Martella, G. Barrera, F. Celegato, M. Coïsson, R. Ferrero, E. S. Olvetti, A. Troia, H. Sözeri, C. Parmeggiani, D. S. Wiersma, P. Tiberto, A. Manzin. Improvement of Hyperthermia Properties of Iron Oxide Nanoparticles by Surface Coating.* ACS Omega, ***2023***, *8(2): 2143–2154.*

## 3.1 Materials and Methods

### 3.1.1 Reagents

Sodium carboxymethyl cellulose (average molecular mass of ~90 kDa), and trisodium citrate dihydrate ($C_6H_5Na_3O_7 \cdot 2H_2O$) were purchased from Sigma-Aldrich (St Louis, MO). All chemicals were used without further purification.

### 3.1.2 Surface coating of $Fe_3O_4$ nanoparticles

To obtain the citrate coating, dried $Fe_3O_4$ NPs were suspended in 50 mL of water (2% w/v) and sonicated for 10 min. An aqueous solution of 4% w/v tri-sodium citrate dihydrate was prepared under stirring and added to the above suspension with a molar ratio of 6.4 ($Fe_3O_4$/citrate). The obtained mixture was sonicated in a sonicator bath and heated up to 60 °C for 1 h. The material was washed three times with deionized water and recovered by magnetic separation.
While for the CMC coating, dried $Fe_3O_4$ NPs were suspended in 15 mL of water (1% w/v) and sonicated for 10 min. An aqueous solution of 0.1% w/v CMC (10 mL) was obtained under stirring and added dropwise to the magnetic suspension. The mixture was stirred overnight, and the $Fe_3O_4$ NPs were collected magnetically and washed three times with deionized water.

### 3.1.3 Dimensional characterization and assessment of surface coating of $Fe_3O_4$ nanoparticles

TEM images were collected at TUBITAK laboratories (Turkey) using a JEM-2100 transmission electron microscope (JEOL, Tokyo, Japan).
To evaluate the presence of the coating on the surface of the $Fe_3O_4$ NPs an analysis by FTIR spectroscopy was performed using a IRAffinity-1S FTIR spectrometer (Shimadzu, Kyoto, JPN).
$Fe_3O_4$ NP composition was investigated by TGA, employing a Discovery SDT 650 analyzer (TA Instruments, New Castle, Delaware, USA), operating with a temperature ramp up to 1000 °C and applying a constant heating rate of 10 °C/min. TGA results enabled the evaluation of the amount of coating bounded to the surface of the NPs.
The hydrodynamic size and colloidal stability of the coated $Fe_3O_4$ NPs were analyzed by DLS using a Zetasizer Ultra instrument (Malvern Panalytical, Malvern, UK). DLS results were obtained with at least three scans for each measurement. The above instrument was also used to evaluate the surface charge of the $Fe_3O_4$ NPs by $\zeta$ potential measurements conducted on the magnetic suspensions at neutral pH. $\zeta$ potential results were obtained with at least three scans for each measurement.
Colloidal stability was also monitored in time by observing the NP suspensions after 6 months, following their preparation, and by characterizing the NPs encapsulated in hydrogels. For the encapsulation, agarose was added to an aqueous suspension of $Fe_3O_4$ NPs, with a concentration of 5 mg/mL, to obtain a concentration of 1% w/v. The mixture was then heated at 80 °C for 10 min to dissolve the agarose and cooled down to form the gel.

### 3.1.4 Magnetic and thermometric characterization of $Fe_3O_4$ nanoparticles

The static hysteresis loops of dry samples were analyzed at room temperature by VSM using a 7410 magnetometer (Lake Shore, Westerville, Ohio, USA). The characterization was performed under DC magnetic fields, varying from −1350 to 1350 kA/m in steps of 0.8 kA/m.
The magnetic properties of uncoated and coated $Fe_3O_4$ NPs were also analyzed under dynamic conditions to better understand the physical mechanisms of magnetic losses in the samples when exposed to an AC magnetic field. The measurements were performed using a custom-built setup [124] with a frequency of 69 kHz and an amplitude selectable up to 38 kA/m, which are conditions compatible with hyperthermia experiments. The hysteresis loops were recorded on liquid samples of uncoated and coated $Fe_3O_4$ NPs with a concentration of approximately 10 mg/mL. To evaluate the heating efficiency of $Fe_3O_4$ NPs, thermometric measurements were conducted, as detailed in Section 2.1.4 in Chapter 2.

## 3.2 Results

### 3.2.1 Assessment of surface coating

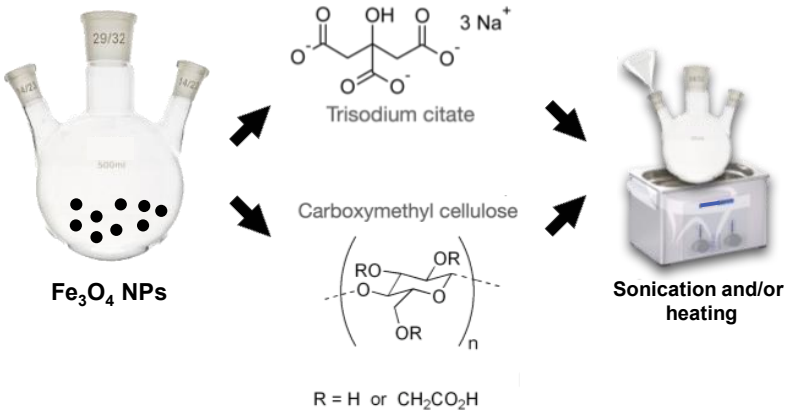



**Figure 3.1.** Schematic representation of the surface coating process of $Fe_3O_4$ NPs.

Figure 3.1 illustrates the production of two distinct samples of coated $Fe_3O_4$ NPs, achieved using two different coating agents: trisodium citrate and CMC. Initially, a solution containing the respective coating agent is introduced into the MNP suspension, followed by heating and/or sonication. Subsequently, the coated MNPs undergo purification through magnetic decantation and several water washes.
Representative TEM images and size distributions of $Fe_3O_4$ NPs with coating of

citrate and CMC are reported in Figure 3.2A and 3.2B, respectively. The coating process does not result in any structural alterations of the $Fe_3O_4$ NPs. They maintain their quasi-spherical shape and exhibit diameters comparable to those of the uncoated NPs (10.9 ± 2.6 nm) analyzed in Chapter 2 (Figure 2.4), it results 10.9 ± 2.6 nm for citrate-coated NPs and 11.3 ± 2.1 nm for CMC-coated NPs. From the TEM images, differences in nanoparticle aggregation can be discerned. As observed for the uncoated $Fe_3O_4$ NPs in Chapter 2, even the NPs with CMC coating (Figure 3.2B) form aggregates with dimensions approximately of 120 nm, likely due to magnetic dipole-dipole interactions. In contrast, citrate-coated $Fe_3O_4$ NPs exhibit smaller clusters (Figure 3.2A), with dimensions around 70 nm.

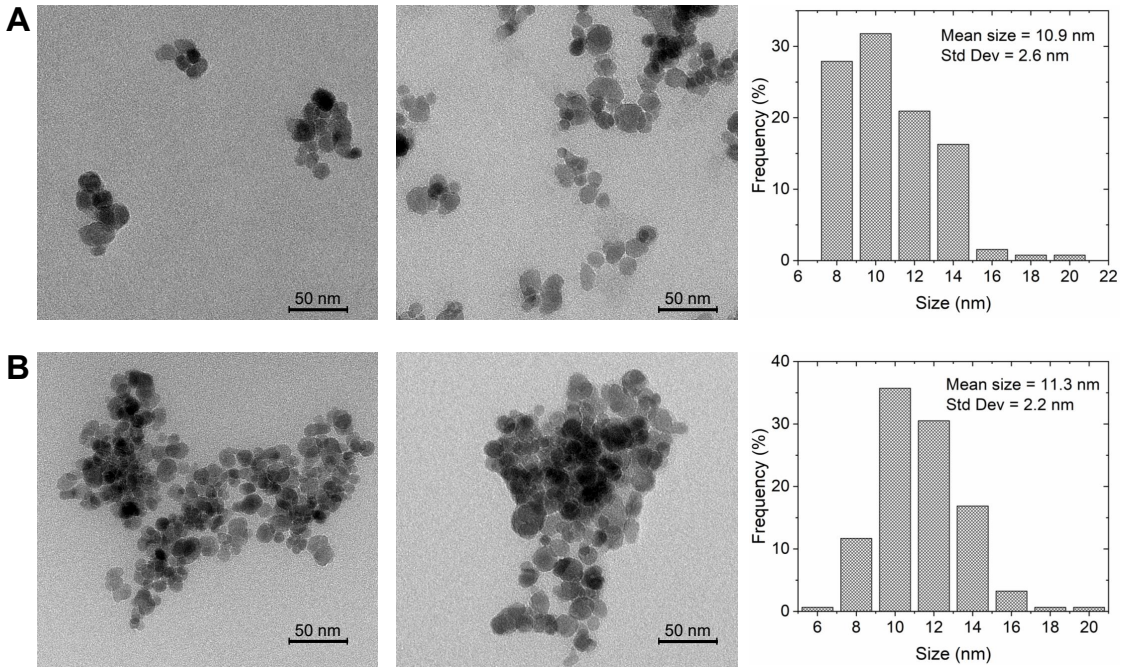



**Figure 3.2.** Representative TEM images and size distributions of $Fe_3O_4$ NPs with (**A**) citrate coating and (**B**) carboxymethyl cellulose coating.

The confirmation of surface coating, whether citrate-based or CMC-based, is established through various characterization techniques, including FTIR spectroscopy, TGA, and DLS analysis. Figure 3.3 presents the FTIR spectra of both uncoated and coated $Fe_3O_4$ NPs. In the spectra of uncoated NPs (black), distinctive features characteristic of $Fe_3O_4$ NPs are evident, such as the band around 580–630 $cm^{-1}$, corresponding to Fe–O bond vibrations, and peaks at 1624 and 3400 $cm^{-1}$, attributed to the bending and stretching vibrations of hydroxyl groups from adsorbed water molecules on the sample surface. [140] However, in the spectra of citrate-coated (red) and CMC-coated (blue) NPs, the emergence of two and three new peaks at 1381, 1616 $cm^{-1}$, and 1059, 1417, 1623 $cm^{-1}$, respectively, is observed. The peaks

at 1381 and 1616 $cm^{-1}$ are associated with the symmetric and asymmetric stretching vibrations of $COO^-$ groups from citrate anions. [141, 142] The peaks at 1059, 1417, and 1623 $cm^{-1}$ are associated with the stretching vibrations of O–C–C bonds and symmetric and asymmetric stretching vibrations of −COO bonds in carboxylic salt structures. The appearance of these new peaks provides evidence of effective bonding of the coating agents to the $Fe_3O_4$ NP surface. [140, 143, 144]

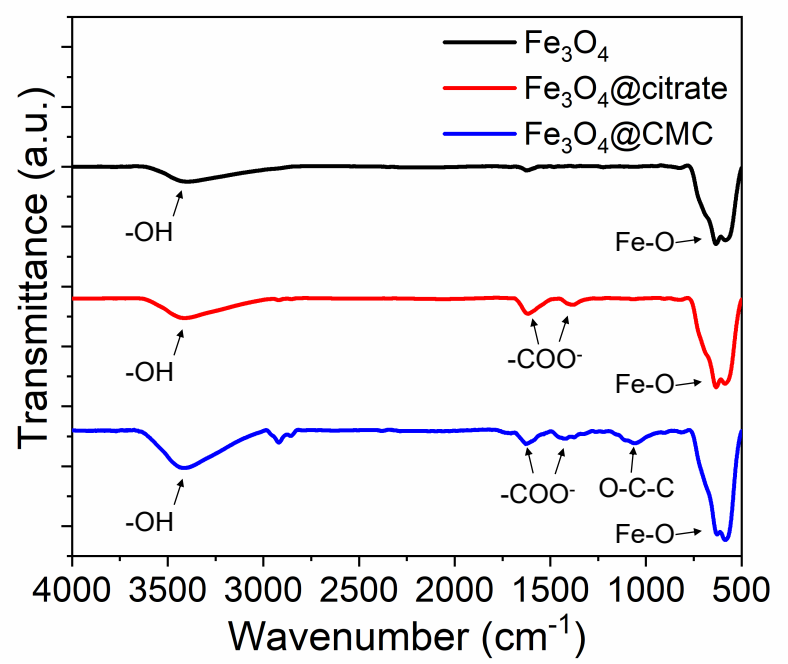



**Figure 3.3.** FTIR spectra of $Fe_3O_4$ NPs (black) and coated NPs with tri-sodium citrate (red) and CMC (blue).

The thermographs obtained via TGA for both uncoated and coated $Fe_3O_4$ NPs are depicted in Figure 3.4. The initial weight reduction below 200 °C is attributed to the desorption of water molecules. Specifically, the thermogravimetric analysis of uncoated NPs illustrates a weight loss of approximately 4% in this temperature range. Conversely, the coated NPs exhibit a weight loss of 5.4% and 3% for citrate- and CMC-coated $Fe_3O_4$ NPs, respectively. These slight discrepancies are primarily due to variations in the water content across the samples. Subsequent weight loss occurring between 200 and 1000 °C corresponds to the decomposition of the coating agent adsorbed on the NP surface. This decomposition accounts for approximately 9.2% and 6.4% for citrate- and CMC-coated NPs, respectively. The observed weight loss suggests a higher quantity of coating agent adsorbed on the surface of NPs treated with citrate compared to those treated with CMC.

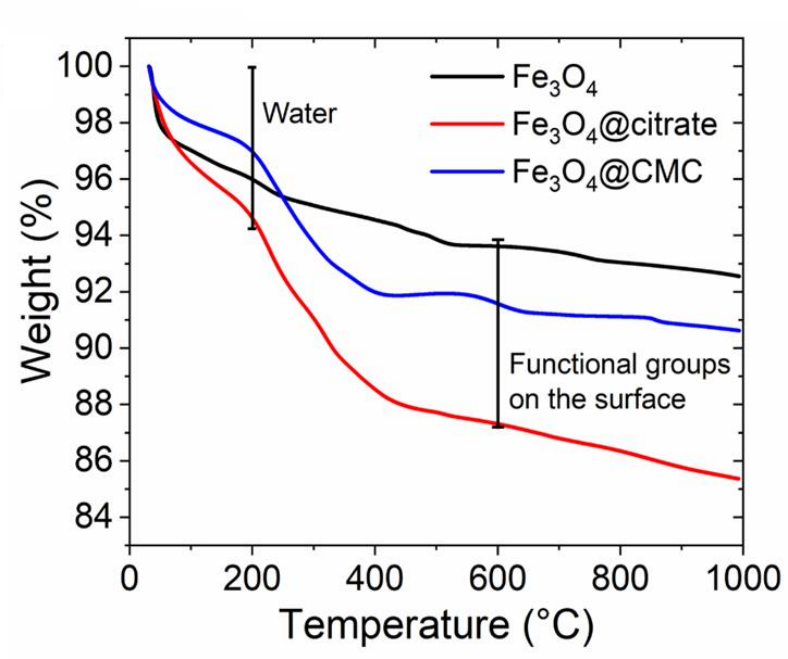



**Figure 3.4.** Thermogravimetric analysis curves for uncoated (black), citrate-coated (red), and CMC-coated (blue) $Fe_3O_4$ NPs.

Finally, the stability of the NPs in solution, a critical parameter for their potential biomedical applications, is assessed. The hydrodynamic size distributions, as characterized by DLS, are illustrated in Figure 3.5, while Table 3.1 presents the mean hydrodynamic size, relative polydispersity index, and $\zeta$ potential value for each sample. DLS and $\zeta$ potential measurements are conducted on both uncoated and coated NPs to investigate any changes in sample dispersion resulting from the surface coating process. DLS enables characterization of the hydrodynamic behavior of NPs, specifically the size of the aggregates in which they are organized. However, this technique does not distinguish between the inorganic material and the organic material of the coating. The mean hydrodynamic size of uncoated NPs is approximately 135 nm, consistent with the aggregate size observed in TEM images (Figure 2.4). The enhancement in dispersion of citrate-coated $Fe_3O_4$ NPs, evidenced by a decrease in aggregate size as observed in the TEM image (Figure 3.2A), is further confirmed by a smaller mean hydrodynamic size of around 95 nm. Conversely, CMC-coated NPs form aggregates with larger dimensions compared to uncoated NPs, with sizes around 150 nm. Hence, the introduction of surface coating results in variations in aggregate size, heavily influenced by the type of coating, as previously demonstrated in the literature through DLS measurements. [145]
The PDI values exhibit similarity across the samples, indicating comparable width in the size distribution. This illustrates that, despite changes in the hydrodynamic

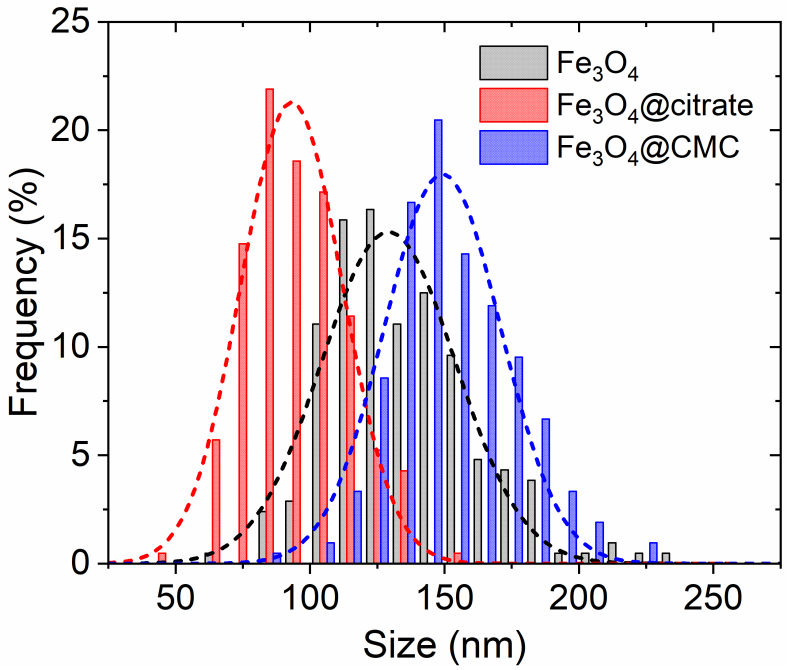



**Figure 3.5.** DLS particle size distribution for uncoated (black), citrate-coated (red), and CMC-coated (blue) $Fe_3O_4$ NPs (the reported Gaussian fits are a guide to the eye).

size of the MNP aggregates due to surface treatment, the distribution width consistently remains peaked.

$\zeta$ potential measurements offer insights into the surface charge of $Fe_3O_4$ NPs, where it is established that values exceeding 30 mV indicate good colloidal stability and low tendency to flocculate. [128] The $\zeta$ potential recorded for uncoated NPs at neutral pH was -24.8 $\pm$ 0.5 mV, consistent with values reported for $Fe_3O_4$ NPs. [129] Citrate- and CMC-coated NPs display $\zeta$ potentials of -26.1 $\pm$ 1.4 and -26.8 $\pm$ 1.0 mV, respectively. The slight elevation in the absolute value of the $\zeta$ potential indicates the absorption of negatively charged carboxylic groups onto the MNP surface. This marginal rise in $\zeta$ potential may be attributed to the minimal presence of coating agents on the surface of $Fe_3O_4$ NPs, as also evidenced by the TGA results.

**Table 3.1.** Mean hydrodynamic size, polydispersity index (PDI) and $\zeta$ potential values for uncoated and coated $Fe_3O_4$ NPs.

| **Sample** | **Mean Hydrodynamic Size** [nm] | **PDI** | **$\zeta$ potential** [mV] |
|---|---|---|---|
| $Fe_3O_4$ | 135 $\pm$ 35 | 0.277 | -24.8 $\pm$ 0.5 |
| $Fe_3O_4$@citrate | 95 $\pm$ 18 | 0.251 | -26.1 $\pm$ 1.4 |
| $Fe_3O_4$@CMC | 152 $\pm$ 27 | 0.276 | -26.8 $\pm$ 1.0 |

### 3.2.2 Magnetic characterization

The magnetic properties of both uncoated and coated $Fe_3O_4$ NPs under static conditions are assessed using VSM at room temperature with the samples in powder form. The magnetic signal measured is normalized to the mass of $Fe_3O_4$ in each sample, with the coating mass subtracted based on TGA results (refer to Figure 3.4).
The $M(H)$ curves at room temperature for uncoated, citrate-coated, and CMC-coated $Fe_3O_4$ NPs are depicted in Figure 3.6, while the $M_S$ and $H_C$ are provided in Table 3.2. The major hysteresis loops of the $Fe_3O_4$ NPs are described in Chapter 2 (Section 2.2.2). The $M(H)$ curves of citrate- and CMC-coated $Fe_3O_4$ NPs closely align with the curve of uncoated NPs, suggesting that the coating type minimally influences the magnetic properties of the samples in their dry state under static conditions.

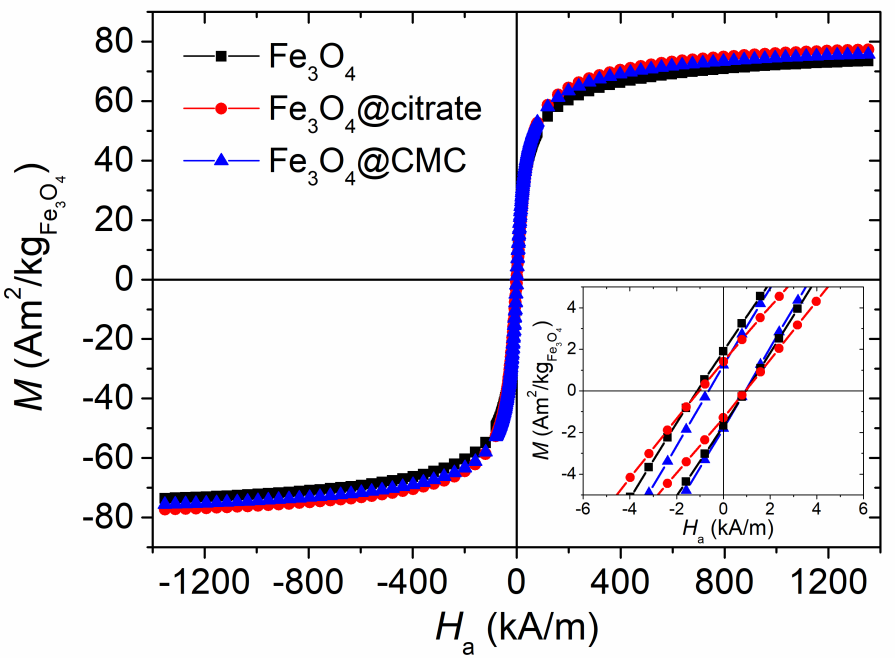



**Figure 3.6.** Room-temperature $M(H)$ curves of uncoated and coated $Fe_3O_4$ NPs in dry form. The magnetization values are normalized to the $Fe_3O_4$ mass, subtracting the coating mass obtained from TGA results. A hysteretic behavior can be inferred from the inset, which shows the portion of the hysteresis loops zoomed around coercivity and remanence.

**Table 3.2.** Values of saturation magnetization ($M_S$), remanent magnetization ($M_R$), and coercivity ($H_C$) of uncoated and coated $Fe_3O_4$ NPs at room temperature. The magnetization values are normalized to the $Fe_3O_4$ mass.

| **Sample** | $\mathbf{M_S}$ [A m$^2$ / kg] | $\mathbf{M_R}$ [A m$^2$ / kg] | $H_C$ [kA/m] |
|---|---|---|---|
| $Fe_3O_4$ | 73.5 | 1.8 | 1.0 |
| $Fe_3O_4$@citrate | 77.3 | 1.3 | 1.0 |
| $Fe_3O_4$@CMC | 75.7 | 1.5 | 0.8 |

AC magnetometry is conducted to explore the MNP capacity for heat release when exposed to AC magnetic fields with a $f$ and $\hat{H}_a$ meeting the Hergt–Dutz limit. [70, 71] Specifically, dynamic hysteresis loops of aqueous suspensions containing both uncoated and coated $Fe_3O_4$ NPs are measured by applying an AC magnetic field with $f$ set at 69 kHz and $\hat{H}_a$ limited to 36 kA/m. The complete set of AC magnetometry results for uncoated and coated $Fe_3O_4$ NPs are reported in Figure 3.7. The hysteresis curves corresponding to specific $\hat{H}_a$ values of 13.3 and 28.4 kA/m are depicted in Figure 3.8. The vertical axis is presented in arbitrary units since the output signal from the custom-built B–H tracer lacks a direct relationship with magnetization values established through a proper calibration procedure. Nevertheless, all hysteresis curves are normalized to the sample mass to facilitate comparison of the magnetic properties across the samples under investigation.

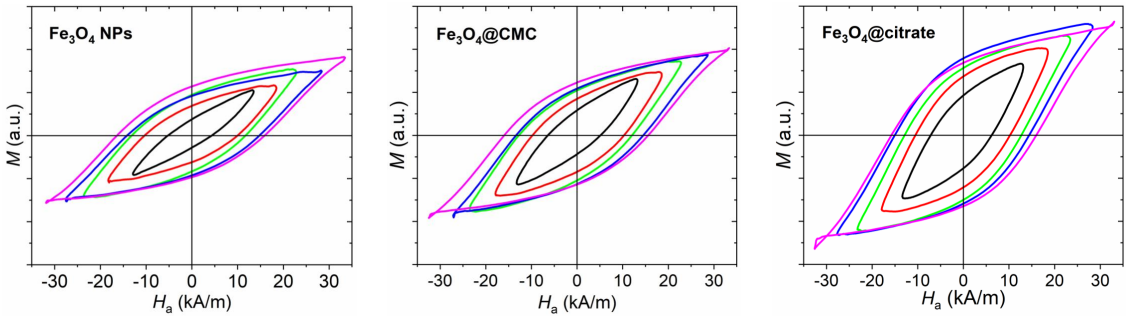



**Figure 3.7.** Dynamic hysteresis loops at room temperature of uncoated and coated $Fe_3O_4$ NPs. The measurements were performed on liquid samples at different values of the AC magnetic field peak amplitude ($\hat{H}_a$) in the range 13-32 kA/m, fixing the frequency ($f$) to 69 kHz. All the hysteresis curves are normalized to the $Fe_3O_4$ mass and reported in arbitrary units with the same inferior and superior limits, to enable direct comparison.

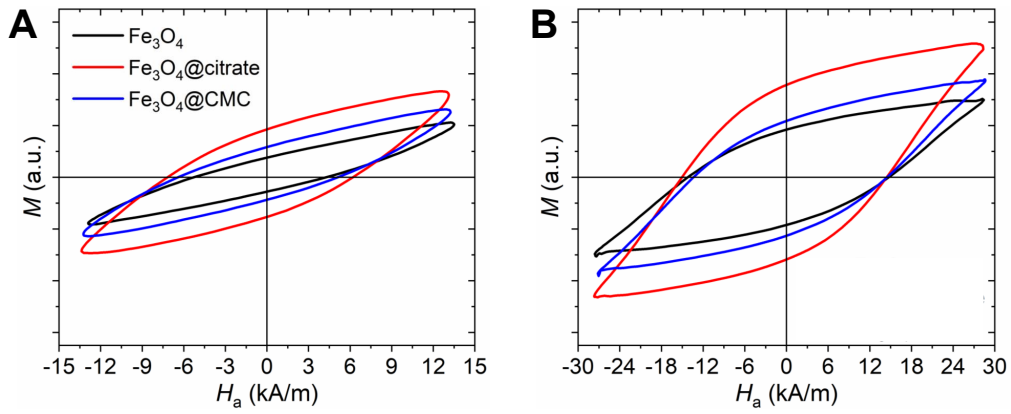



**Figure 3.8.** Dynamic minor hysteresis loops for uncoated (black), citrate-coated (red), and CMC-coated (blue) $Fe_3O_4$ NPs for a magnetic field with peak amplitude $\hat{H}_a$ of (**A**) 13.3 kA/m and (**B**) 28.4 kA/m. All of the hysteresis curves are normalized to the $Fe_3O_4$ mass and reported in arbitrary units with the same inferior and superior limits to enable direct comparison.

For all samples, under dynamic conditions (see Figure 3.7), it is possible to observe that the coercivity $H_C$ varies with the variation of $\hat{H}_a$. Moreover, the $H_C$ values are higher than those of the corresponding static major hysteresis loops (as shown in the inset of Figure 3.6) due to relaxation effects associated with the dynamic response to AC excitation. These effects give rise to a well-defined hysteretic behavior, characterized by loops with a significant area, thereby facilitating an effective release of energy that can be harnessed for magnetic hyperthermia applications. [146]
Figure 3.9 illustrates the areas of the dynamic hysteresis loops plotted as a function of $\hat{H}_a$ in the range of approximately 12-38 kA/m for all examined samples. Citrate-coated $Fe_3O_4$ NPs (red curve) exhibit a larger loop area, indicating higher heating efficiency, across the entire range of $\hat{H}_a$ values compared to the other two samples. Conversely, the CMC-based coating (blue curve) results in a slight increase in loop area values with respect to the uncoated MNPs (black curve). These findings might be attributed to the ability of the citrate-based coating to contribute to a decrease in the size of MNP aggregates, thus enhancing dispersion properties, as shown by DLS analysis (Figure 3.5).

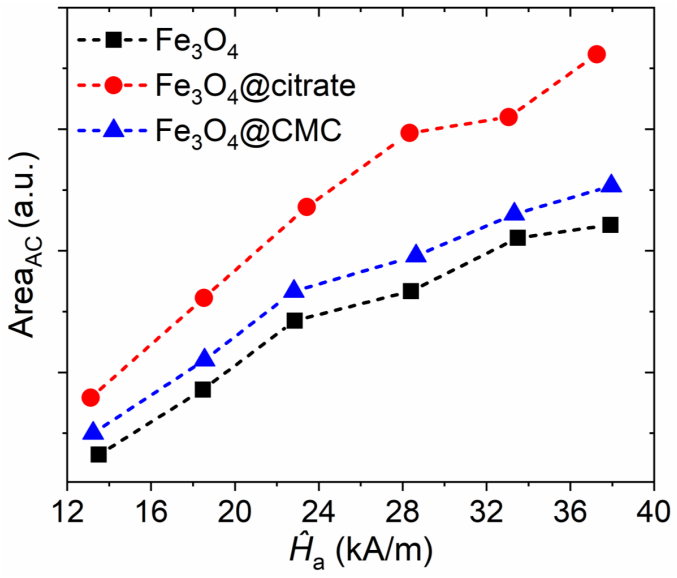



**Figure 3.9.** Areas of the dynamic hysteresis loops versus $\hat{H}_a$, evaluated for all of the considered samples at a $f$ of 69 kHz.

### 3.2.3 Thermometric characterization

Thermometric measurements are conducted to provide a quantitative assessment of the coating effect on the heating efficiency of the MNPs under investigation. The characterization involves liquid suspensions housed in a polypropylene test tube immersed in a water bath held within a quartz holder as shown in Figure 2.1 in Chapter 2. Figure 3.10 depicts the heating and cooling transients recorded with a fiber optic probe for aqueous solutions containing uncoated, citrate- and CMC-coated $Fe_3O_4$ NPs. These thermal profiles are recorded after exposing the MNP samples for 60 min to an AC magnetic field with a frequency of 100 kHz and a peak amplitude in the range 24-48 kA/m, thus satisfying the Hergt–Dutz limit. [70, 71] The NP concentration used is 12 mg/mL to ensure both the stability of the magnetic solution and the maintenance of temperature within an appropriate range during the measurements. Utilizing an analytical thermodynamic model [125] that accounts for the various heat exchange mechanisms within the experimental setup (detailed in Section 2.1.4 in Chapter 2), the experimental curves are fitted to estimate the SLP of the MNPs as an indicator of their heating efficiency. These findings are validated through simulations conducted with the in-house heat-transfer finite element solver, outlined in Appendix A.

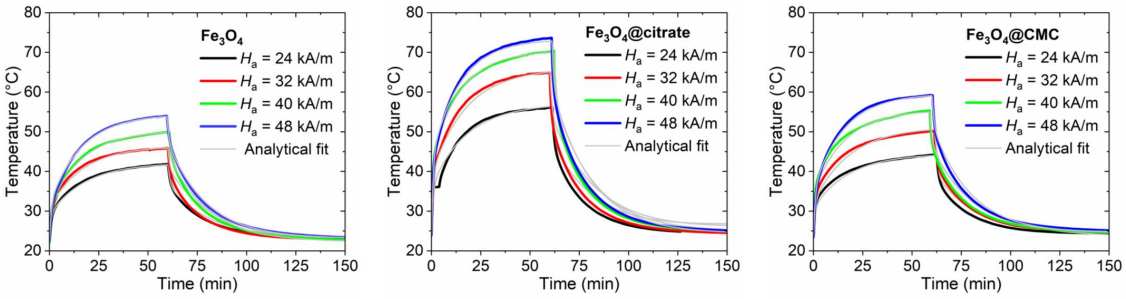



**Figure 3.10.** Time evolutions of the temperature of the magnetic suspensions containing the uncoated NPs, the citrate- and CMC-coated NPs following the application of an AC magnetic field with different peak amplitudes $\hat{H}_{\mathrm{a}}$ variable in the range 24-48 kA/m and frequency fixed to 100 kHz. The cooling transients, after the switching off of the field, are also reported. The graphs contain the experimental data and the best fit outputs of the analytical thermodynamic model.

The SLP values, obtained from fitting the experimental data and validated through numerical modeling, are shown in Figure 3.11 and Table 3.3, illustrating their dependence on $\hat{H}_{\mathrm{a}}$ for all the samples under investigation. Consistent with the results of the dynamic hysteresis loop measurements (refer to Figure 3.9), the citrate-coated $Fe_3O_4$ NPs demonstrate the highest thermal efficiency across the entire range of $\hat{H}_{\mathrm{a}}$, exhibiting an SLP of approximately 170 W/g at $\hat{H}_{\mathrm{a}} = 48$ kA/m, which is about 50% higher than that of the uncoated MNPs. In contrast, the CMC-coated NPs show marginal enhancement in heating efficiency, with an SLP nearing 100 W/g at $\hat{H}_{\mathrm{a}} = 48$ kA/m. Meanwhile, the uncoated NPs exhibit an SLP around 85 W/g, a value already attained at $\hat{H}_{\mathrm{a}} = 32$ kA/m.

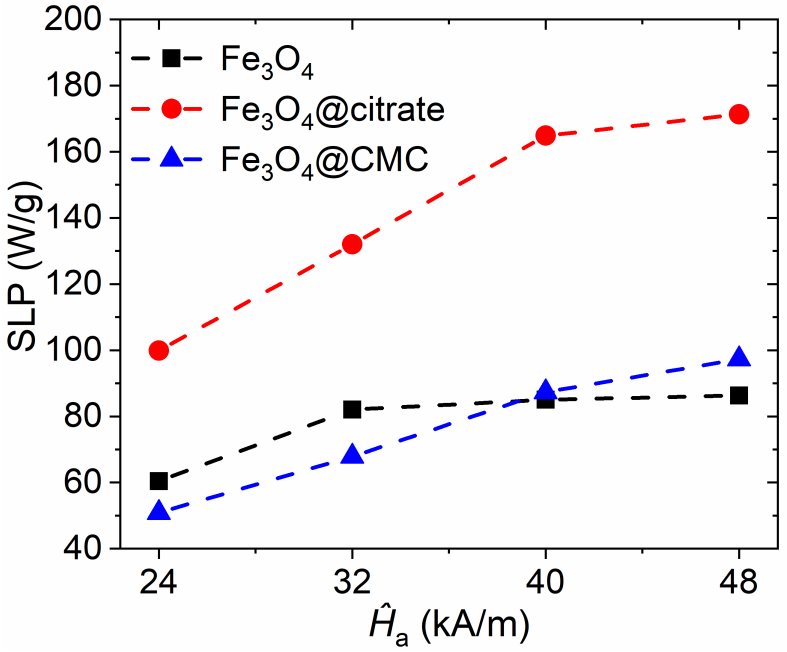



**Figure 3.11.** SLP values for uncoated and coated $Fe_3O_4$ NPs obtained at different peak amplitudes $\hat{H}_a$ of the AC magnetic field, fixing the frequency $f$ to 100 kHz.

**Table 3.3.** SLP values for uncoated and coated $Fe_3O_4$ NPs, obtained at different peak amplitudes $\hat{H}_a$ of the AC magnetic field (24-48 kA/m), setting the frequency $f$ at 100 kHz.

| **Sample** | $\hat{H}_a$ | | | |
|---|---|---|---|---|
| | 24 kA/m | 32 kA/m | 40 kA/m | 48 kA/m |
| $Fe_3O_4$ | 60.4 | 82.0 | 85.0 | 86.3 |
| $Fe_3O_4$@citrate | 99.8 | 132.0 | 164.9 | 171.3 |
| $Fe_3O_4$@CMC | 50.8 | 67.8 | 87.4 | 97.3 |

## 3.3 Comparison with data in literature

In this section, a comparison with the current state of the art is conducted, analyzing the influence of surface coating on the heating properties of MNPs. The findings regarding heating efficiency are primarily linked to hysteresis losses. Despite the thermometric measurements are conducted on MNPs dispersed in a liquid, the Brown relaxation mechanism is significantly impeded due to the substantial hydrodynamic volume of the MNPs aggregates (as illustrated in Figure 3.5). Specifically, the Brown relaxation time, roughly estimated for each sample, is orders of magnitude longer than the relaxation time $\tau = 1/(2\pi f)$ associated with the operating

frequency used, resulting in a minimal impact. [147] The heating contribution from the hysteresis losses is influenced by the effective volume of the magnetic structures that collectively respond to the AC magnetic field. The discrepancies observed in the SLP values between the citrate-coated NPs and the other two samples can be attributed to the varying sizes of the NP aggregates (95 nm compared to 130 and 150 nm for the uncoated and CMC-coated NPs, respectively). A simple model demonstrates that the heating efficiency in samples containing clusters of NPs with a diameter less than 15 nm decreases as the aggregate size increases (i.e., with an increase in the number of NPs within the aggregate). [148]

In essence, the 50% enhancement in the SLP achieved through the citrate-based surface treatment post-preparation stands as a highly promising outcome, especially when compared to existing data for spherical $Fe_3O_4$ NPs as summarized in Table 3.4. This table also presents the values of the intrinsic loss power (ILP), defined as the SLP normalized to $\hat{H}_a^2$ and $f$, under the assumption of a linear relationship between SLP and $(\hat{H}_a^2 \cdot f)$ as a first approximation. However, this relationship is not suitable for all applied field amplitudes and frequencies, resulting in an ILP that remains relatively constant only within certain ranges of low field amplitude and frequency. [43, 71, 149] This explains why the ILP values for both the uncoated and coated $Fe_3O_4$ NPs synthesized here are not constant for the $\hat{H}_a$ values employed in thermometric characterization (within the range of 24–48 kA/m). Nonetheless, the ILP determined for the citrate-coated NPs (ranging from 0.74 to 1.73) is notably high across all considered magnetic field peak amplitudes, as evidenced by comparisons with other literature data.

In prior studies, the post-synthesis application of citrate, typically employed to enhance colloidal stability, does not result in a significant enhancement of hyperthermia properties compared to the uncoated NPs. [150, 151] Conversely, the utilization of chitosan leads to an approximate 48% increase in the SLP; however, this observation is made under conditions exceeding the Hergt–Dutz limit. [152] Post-synthesis coatings may also contribute to a reduction in NPs heating efficiency. For instance, reductions in SLP of up to 12%, 26%, and 52% are reported for treatments with dextran, oleic acid, and polyethylene glycol (PEG), respectively. [150, 151, 153]

Regarding *in situ* treatment or synthesis processes conducted in an environment containing coating agents, it is observed that in most cases, MNPs synthesized in the presence of citrate, dextran, PEG, polyacrylic acid (PAA), and hyaluronic acid (HA) exhibit lower SLP values compared to uncoated NPs. [154, 155] Particularly noteworthy is the case of *in situ* PAA coating, which results in a 98% reduction in SLP. However, this decrease can reasonably be attributed to a significant reduction in the average diameter of the NPs, from 12 to 5 nm, along with a consequent decrease in the final saturation magnetization. [155] The decline in SLP may also

be linked to a reduction in magnetocrystalline anisotropy and, subsequently, coercivity, as a result of the alteration of the magnetic order of the surface layers. [154] Slight enhancements in heating efficiency are noted for the *in situ* oleic acid coating of iron oxide NPs at a concentration of 1% v/v, primarily due to improved dispersion in water. [156] Conversely, significant increases in SLP are observed with *in situ* coatings using polyvinylpyrrolidone (PVP) or fucoidan treatments, reaching approximately 60% and 230%, respectively. This substantial improvement is attributed to the dual role of coating agents in surface stabilization of NPs and as growth modifiers influencing NP size, which in turn affects saturation magnetization. [155, 157]

**Table 3.4.** Comparison of the results from our study to data from the literature regarding the heating efficiency of spherical $Fe_3O_4$ NPs. PVP = polyvinylpyrrolidone, PEG = polyethylene glycol, PAA = polyacrylic acid, HA = hyaluronic acid.

| **Ref** | **Size** [nm] | **Coating** | **Coating procedure** | $\hat{H}_a$ [kA/m] | $f$ [kHz] | **SLP** [W/g] | **ILP** [nH$^2$/kg] |
|---|---|---|---|---|---|---|---|
| Our study | 10 | / | / | 24 | 100 | 60.4 | 1.05 |
| | | citrate | post | | | 99.8 | 1.73 |
| | | CMC | post | | | 50.8 | 0.88 |
| | | / | / | 48 | 100 | 86.3 | 0.37 |
| | | citrate | post | | | 171 | 0.74 |
| | | CMC | post | | | 97 | 0.42 |
| [150] | 13 | / | / | 15.9 | 252 | 63.4 | 0.99 |
| | | citric acid | post | | | 65.8 | 1.03 |
| | | APTES | post | | | 67.2 | 1.05 |
| | | dextran | post | | | 55.6 | 0.87 |
| [151] | 8.5 | / | / | 24 | 418 | 125 | 0.52 |
| | | oleic acid | post | | | 60 | 0.25 |
| | | citrate | post | | | 120 | 0.50 |
| [152] | 21.8 | / | / | 26.6 | 265 | 80 | 0.43 |
| | 15.1 | chitosan | post | | | 118.8 | 0.63 |
| [153] | 20 | / | / | 26.6 | 265 | 38.4 | 0.20 |
| | 5 | oleic acid | post | | | 33.5 | 0.18 |
| | 10 | PEG | post | | | 28.3 | 0.15 |
| [154] | 21 | / | / | 23.9 | 765 | 440 | 1.01 |
| | 8 | citrate | *in situ* | | | 190 | 0.44 |
| | 20 | CTAB | *in situ* | | | 95 | 0.22 |
| | 22 | dextran | *in situ* | | | 360 | 0.83 |
| [155] | 12.5 | / | / | 13.5 | 333 | 100 | 1.65 |
| | 5.9 | dextran | *in situ* | | | 36 | 0.59 |
| | 11 | PVP | *in situ* | | | 160 | 2.64 |
| | 9.5 | PEG | *in situ* | | | 70 | 1.15 |
| | 5 | PAA | *in situ* | | | 2 | 0.03 |
| | 7.5 | HA | *in situ* | | | 40 | 0.65 |
| [156] | 8 | / | / | 23.5 | 312 | 39.5 | 0.23 |
| | 9.3 | oleic acid 0.2% | *in situ* | | | 34.81 | 0.20 |
| | 8.3 | oleic acid 0.5% | *in situ* | | | 23.36 | 0.14 |
| | 10 | oleic acid 1.0% | *in situ* | | | 45.98 | 0.21 |
| [157] | 10.2 | / | / | 14.7 | 276 | 30 | 0.50 |
| | 11.7 | fucoidan | post | | | 156 | 2.62 |
| | 6.4 | fucoidan | *in situ* | | | 100 | 1.68 |

## 3.4 Analysis of nanoparticle solution stability

In concluding our experimental investigations, the stability of the MNPs in solution, a critical parameter for the development of biomedical applications, is examined. Figure 3.12A illustrates the comparison of various magnetic suspensions six months after their preparation. With uncoated NPs, a complete precipitation is observed, with sedimentation initiating within the first few hours following solution sonication. Although sedimentation of a portion of CMC-coated NPs is observed, they exhibit improved stability. However, once again, the utilization of sodium citrate yields the most favorable solution, ensuring NP dispersion and long-term storage without precipitation.
Similar results are noted concerning the encapsulation of MNPs in hydrogels and a comparison of the obtained samples is depicted in Figure 3.12B. Once again, the surface coating proves to be pivotal in facilitating the effective dispersion of NPs. While uncoated MNPs exhibit the precipitation of large MNP aggregates (visible at the bottom of the test tube), sodium citrate leads to superior dispersion with MNPs uniformly distributed, as evidenced by visual inspection. This observation underscores the potential for further material advancements, particularly in applications requiring optimal dispersion, such as hyperthermia studies in solid environments used as tissue mimicking materials (to emulate interaction with biological tissues) or the controlled release of molecules (e.g., drugs) from thermoresponsive gels.

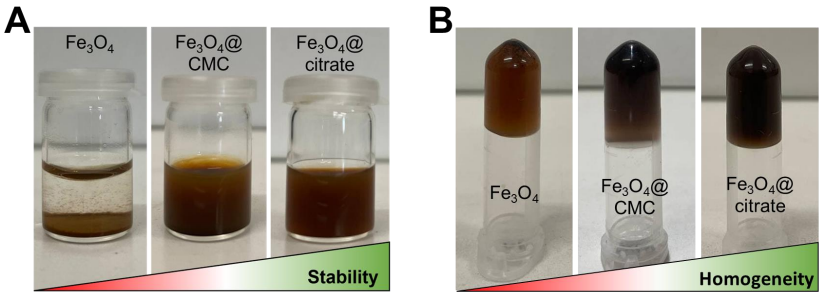



**Figure 3.12.** (**A**) Images of magnetic solutions, taken after 6 months from their synthesis. (**B**) Images of agarose gels with encapsulated MNPs. The comparison was made between uncoated, citrate-coated, and CMC-coated NPs.

## 3.5 Conclusions

$Fe_3O_4$ NPs, fully characterterized in the previous chapter, were subjected to different surface coatings employing sodium citrate or CMC. The investigation aimed to assess their potential application in magnetic hyperthermia, focusing on heating efficiency and colloidal stability.

It was demonstrated that both surface coatings contribute to the long-term stability and dispersion of $Fe_3O_4$ NPs in solution, facilitating their homogeneous encapsulation in more viscous materials such as hydrogels. Notably, sodium citrate exhibited superior performance, significantly enhancing both colloidal stability and heating efficiency compared to CMC. The improved dispersion of citrate-coated NPs resulted in the formation of smaller NP aggregates, leading to a substantial enlargement of the AC loop area and a consequent 50% increase in SLP compared to uncoated NPs.
In conclusion, this study provides valuable insights into the enhancement of $Fe_3O_4$ NPs' performance for magnetic hyperthermia applications through surface coatings, offering promising prospects for their practical implementation in various biomedical contexts.

# Chapter 4

# *In vitro* experiments of magnetic hyperthermia

In the previous Chapter, the optimization of heating efficiency of $Fe_3O_4$ NPs *via* surface coating treatments was explored. This advancement paved the way for a comprehensive exploration into the effects of these MNPs on cellular cultures following magnetic hyperthermia treatments.
In this Chapter, the investigations initially focus on assessing the biocompatibility and potential cytotoxic effects of $Fe_3O_4$ and $CoFe_2O_4$ NPs at different concentrations, both with and without citrate coating, which has demonstrated a greater effect on increasing the SLP of the MNPs. Subsequently, a protocol is developed for conducting *in vitro* magnetic hyperthermia experiments using $Fe_3O_4$ NPs on adherent cultures of human lung cancer cell line.

## 4.1 Materials and Methods

### 4.1.1 Reagents

Heat-inactivated fetal bovine serum (FBS) and penicillin-streptomycin were obtained from Sigma-Aldrich (St Louis, Missouri, USA). High glucose (1 g/L) Dulbecco's Modified Eagle's Medium (DMEM) w/o L-glutamine w/ sodium pyruvate was purchased from Biowest (Nuaillé, France). 200 mM L-glutamine was obtained from Lonza (Basel, Switzerland). Resazurin sodium salt was purchased from Invitrogen by Thermo Fisher Scientific (Waltham, Massachusetts, USA). All chemicals were used without further purification .

### 4.1.2 Cell culture

A549 human lung cancer cell line (ATCC CCL-185) was purchased from the American Type Culture Collection. The cells were cultured in DMEM medium

containing 1 g/L of glucose, without L-glutamine, and with sodium pyruvate. The culture medium was supplemented with 10% ($v/v$) heat inactivated FBS, 1% ($v/v$) L-glutamine, and 1% ($v/v$) penicillin/streptomycin. The cell cultures were maintained in an incubator at 37 °C with 5% $CO_2$. Cells were counted using the Neubauer cell counting chamber to determine the cell concentration.

### 4.1.3 Resazurine viability assay

To assess the cytotoxicity of certain molecules or nanomaterials, it is often necessary to employ high-throughput screening methods. There are numerous approaches available for evaluating cellular cytotoxicity and viability, such as flow cytometry, 3H-thymidine incorporation, fluorometric DNA assays, or cell counting with trypan blue. However, each of these methods presents some issues, as being expensive or time-consuming, and producing toxic or radioactive waste. [158]
Cellular viability and metabolic activity can also be assessed through the measurement of nicotinamide adenine dinucleotide (NADH) and nicotinamide adenine dinucleotide phosphate (NADPH) levels, as these pyridine nucleotides are synthesized during metabolic processes. While direct quantification of these reducing agents is feasible, their absolute concentrations may not serve as the most effective indicator of metabolic activity. Instead, the rate at which they are utilized, or the turnover rate, holds greater significance. This turnover rate can be measured by selectively reducing specific compounds, such as various tetrazolium salts (MTT, MTS, XTT, or WST) or resazurin. In these reactions, dehydrogenases utilize NADH/NADPH as a co-substrate, providing insight into metabolic activity. The outcome of reducing these compounds is the production of a colored and/or fluorescent product that can be detected using simple spectroscopic techniques. [158]
The resazurin assay, also known as the Alamar Blue assay, is a fluorometric-based method utilized for quantifying the population of viable cells within a sample. This assay is widely employed in both mammalian cells and bacteria to assess cell viability and cytotoxicity. [159] The principle behind the assay involves the reduction of resazurin, a non-fluorescent blue dye, to resorufin, a vividly fluorescent pink compound, by dehydrogenase or reductase enzymes present in the cytoplasm of living cells. This reduction, depicted in Figure 4.1, occurs in various cellular compartments such as cytosol, microsomes, and mitochondria. [160] The fluorescence emitted by resorufin is directly proportional to the number of viable cells in the sample, allowing for straightforward measurement using a plate reader. [161]

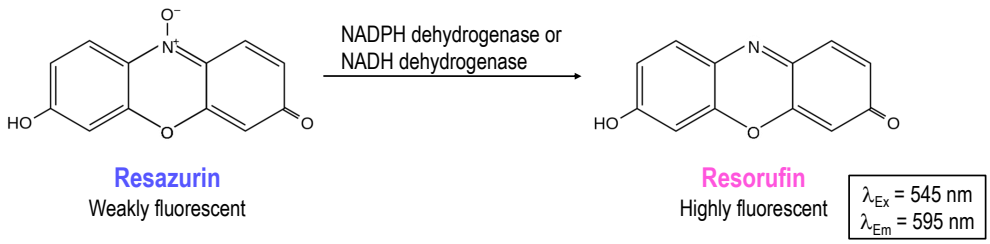



**Figure 4.1.** Enzymatic reduction of resazurin to resorufin.

The advantages of the resazurin assay lie in its versatility and effectiveness. Firstly, resazurin can be dissolved in physiological buffers, allowing for direct testing within cell cultures. This facilitates ease of use and eliminates the need for additional steps in sample preparation. Secondly, the resazurin assay is a cost-effective solution and demonstrates higher sensitivity compared to tetrazolium assays. [158, 162] Lastly, resazurin exhibits non-toxicity to cells at low concentrations and for short incubation periods, rendering it suitable for time-lapse investigations, as cells can return to culture or be used for other purposes after undergoing this viability assay.

### 4.1.4 *In vitro* cytotoxicity tests

$Fe_3O_4$ and $CoFe_2O_4$ NP cytotoxicity, with and without the coating of citrate, was tested *in vitro* on A549 human lung cancer cell line using the resazurin assay. Cells were seeded in 48-well plates (15,000 cells per well) and incubated overnight under standard conditions. Subsequently, the cells were treated with uncoated and citrate-coated NPs at four different concentrations dispersed in the culture medium (0.5, 1, 1.5, 2 mg/mL). Cell viability was assessed after 24, 48, and 72 h of treatment.
A 44 $\mu$M solution of resazurin in complete DMEM was freshly prepared before each experiment. After the culture medium was removed, 250 $\mu$L of resazurin solution was added to each well, and the cells were incubated for 1.5 h at standard conditions. Then, the metabolized resazurin solution was collected and transferred to a 96-well plate for fluorescence intensity (FI) measurement.
FI measurements were conducted using the Spark multimode microplate reader (Tecan, Hombrechtikon, Switzerland) using an excitation wavelength ($\lambda_{Ex}$) of 545 nm and an emission wavelength ($\lambda_{Em}$) of 595 nm. [163–166] For each experiment, the RFU (Relative Fluorescence Units) was collected. Results from samples treated with NPs were normalized on the control sample (without NPs), considered as 100% viability. Therefore, the results were expressed as a percentage of cell viability relative to the control sample.
Additionally, for all sample groups, a cell sample was treated with 15% $v/v$ dimethyl sulfoxide (DMSO) as a positive control.

**Statistical analysis**

The data were presented as the mean ± standard deviation (SD) obtained from three biological replicates. Differences in cell viability between treated and untreated cells were determined using one-way ANOVA with Tukey's post-hoc multiple comparison test. Differences were considered statistically significant at $p-\text{value} < 0.05$: $^{*}p \leq 0.05$; $^{**}p \leq 0.01$; $^{***}p \leq 0.001$; $^{****}p \leq 0.0001$.

### 4.1.5 *In vitro* magnetic hyperthermia tests

Magnetic hyperthermia experiments on cell lines were conducted using a custom-built setup capable of generating a uniform AC magnetic field with a frequency of 100 kHz and a peak amplitude of 48 kA/m. To expose cell samples to the AC magnetic field, sample containers with appropriate dimensions (diameter of 18 mm and height of 8 mm) were used, tailored to fit within the setup. Since these sample containers were not pre-treated for cell cultures, it was necessary to modify the experimental protocol by sterilizing the containers through immersion in 96% ethanol for at least 72 h. Additionally, sterile glass coverslips with a diameter of 10 mm were placed at the bottom of the containers to facilitate cell adhesion.
Two distinct experiments of magnetic hyperthermia on cell cultures were conducted. The first experiment (Experiment#1), similar to those documented in literature [167–173], involved incubating cells with a known concentration of MNPs, exposing the sample to the AC magnetic field, and assessing cellular viability 48 h post-treatment. The second experiment (Experiment#2) involved incubating cells with MNPs for a duration necessary for internalization into the cytoplasm or interaction with the cell membrane, followed by washes to remove excess MNPs. Subsequently, cells were exposed to the AC magnetic field, and cellular viability was assessed after 72 h. This approach allows for the evaluation of cellular damage caused by internalized MNPs or those in close proximity to the cell membrane. The internalization of MNPs within the cells was assessed using a Zeiss Axio Observer Z1/7 inverted microscope (Carl Zeiss, Oberkochen, Germany), and the images were analyzed with Zeiss software ZEN 2.6.
Before proceeding with magnetic hyperthermia treatment on cell cultures, preliminary experiments were conducted to evaluate the temperature reached by the culture medium (DMEM) when exposed to the AC magnetic for 30 min. Furthermore, tests were conducted with different MNP concentrations under the same field conditions to determine the most suitable concentration for subsequent magnetic hyperthermia experiments.
In Experiment#1, which involves magnetic hyperthermia treatment with dispersed MNPs in the culture medium, cells were seeded (30,000 cells per well) on coverslips within sterilized containers using the procedure mentioned above and incubated for 24 h under standard conditions. Subsequently, the culture medium was removed,

and 400 $\mu$L of 1.5 mg/mL solutions of $Fe_3O_4$ NPs with and without citrate coating dispersed in DMEM were added to the wells. Cells were then incubated for an additional 24 h under standard conditions before being exposed to the AC magnetic field for 30 min. Cell viability was assessed using a resazurin assay at 24 and 48 h post-treatment, with results normalized against the untreated control sample to express cellular viability relative to the control.
In Experiment#2, which involves magnetic hyperthermia treatment with internalized MNPs followed by removal of excess MNPs, cells were seeded in 24-well plates (100,000 cells per well) and incubated for 24 h under standard conditions. Subsequently, cells were exposed to 450 $\mu$L of 1.5 mg/mL NP solution for 40 h. After trypsinization and centrifugation, cells were seeded on coverslips within sterilized containers and incubated for 24 h under standard conditions. Cell viability was assessed using a resazurin assay to determine the number of cells seeded, excluding variability due to any cell loss during the preceding wash steps. Cells were then exposed to the AC magnetic field for 60 min, with viability assessed using a resazurin assay 72 h post-treatment. Results from treated samples were normalized against the control sample comprising cells without MNP exposure but treated with the AC magnetic field. Additionally, results from treated samples were compared with samples exposed to NPs but without exposure to the AC magnetic field.

## 4.2 Results

### 4.2.1 *In vitro* cytotoxicity tests

MNPs, especially those made of iron oxides, are generally considered biocompatible. [174–177] However, their surface chemistry, along with shape, size, and aggregation state, can influence toxic effects and consequently the biocompatibility of MNPs. [177–180] One of the most well-known mechanisms induced by MNPs causing cytotoxicity is the production of reactive oxygen species (ROS). Indeed, MNPs, due to their small sizes, can easily penetrate cells, and their high surface area to volume ratio leads to increased chemical reactivity, resulting in elevated ROS production upon contact with biological tissues. [181–184] ROS production is triggered via Fenton and Haber-Weiss reactions, inducing oxidative stress within cells in terms of lipid peroxidation, protein oxidation, and DNA damage. [180, 184] Hence, it is necessary to investigate the biosafety of nanomaterials used in biomedicine through *in vitro* cytotoxicity tests, which allow an understanding of the effects of MNPs on cell lines. [177] Noteworthy is the statement presented in ISO 10993-5:2009, according to which a survival rate above 70% is not considered toxic. [185]
In the literature, there are many studies on the cytotoxicity of MNPs conducted on two-dimensional cell cultures, but most of these evaluate the effects of very low

concentrations of MNPs, i.e., less than 0.5 mg/mL, [167, 172, 177, 180, 186–188] and consider very short treatment times with MNPs, i.e., less than or equal to 24 h. [167, 168, 186, 187] Below, cytotoxicity on the previously described MNPs is evaluated after incubation for up to 72 h and at higher concentrations, up to 2 mg/mL.

In this experiment, the cytotoxicity of $Fe_3O_4$ and $CoFe_2O_4$ NPs, with and without citrate coating, is evaluated *in vitro* using the A549 human cancer cell line. Cells are exposed to four different concentrations of each MNP sample ranging from 0.5 to 2 mg/mL for 72 h, and cell viability is assessed using the resazurin assay every 24 h. Figure 4.2 and Figure 4.3 depict the results obtained from the *in vitro* cytotoxicity tests conducted on $Fe_3O_4$ and $CoFe_2O_4$ NPs, respectively.

In the case of $Fe_3O_4$ NPs, cellular viability is minimally affected, both for uncoated and citrate-coated NPs. As depicted in Figure 4.2A, there is a dose-dependent decrease in cellular viability after 72 h of treatment, while consistently maintaining values above 70% for all concentrations, except for the highest concentrations (1.5 mg/mL and 2 mg/mL). However, in Figure 4.2B, which represents the 72-h treatment data, a statistically significant difference is observed for citrate-coated $Fe_3O_4$ NPs, particularly at higher concentrations ranging from 1.5 to 2 mg/mL, as indicated by the ANOVA test. There are no significant differences in terms of toxicity between uncoated and citrate-coated $Fe_3O_4$ NPs; although the cell viability values for the citrate-coated NPs are slightly lower, the standard deviation ranges make the data comparable.

Concerning $CoFe_2O_4$ NPs, Figure 4.3A illustrates a dose-dependent decrease in cellular viability across all treatment time points (24, 48, and 72 h), with more pronounced cytotoxic effects on cells compared to $Fe_3O_4$ NPs. In Figure 4.3B, focusing on the 72-h treatment, a decrease in cellular viability below 70% is observed starting from the concentration of 1 mg/mL, reaching values as low as around 20% for the highest concentration (2 mg/mL). Particularly noteworthy is the statistically significant difference observed for all tested concentrations, as indicated by the ANOVA test. In the case of citrate-coated $CoFe_2O_4$ NPs, there are greater cytotoxic effects compared to uncoated ones, demonstrating a negative effect on cell viability of citrate, as confirmed in some works in the literature. [189, 190]

In all experiments, a cell sample treated with 15% $v/v$ DMSO as an apoptosis inducer is used as the positive control.

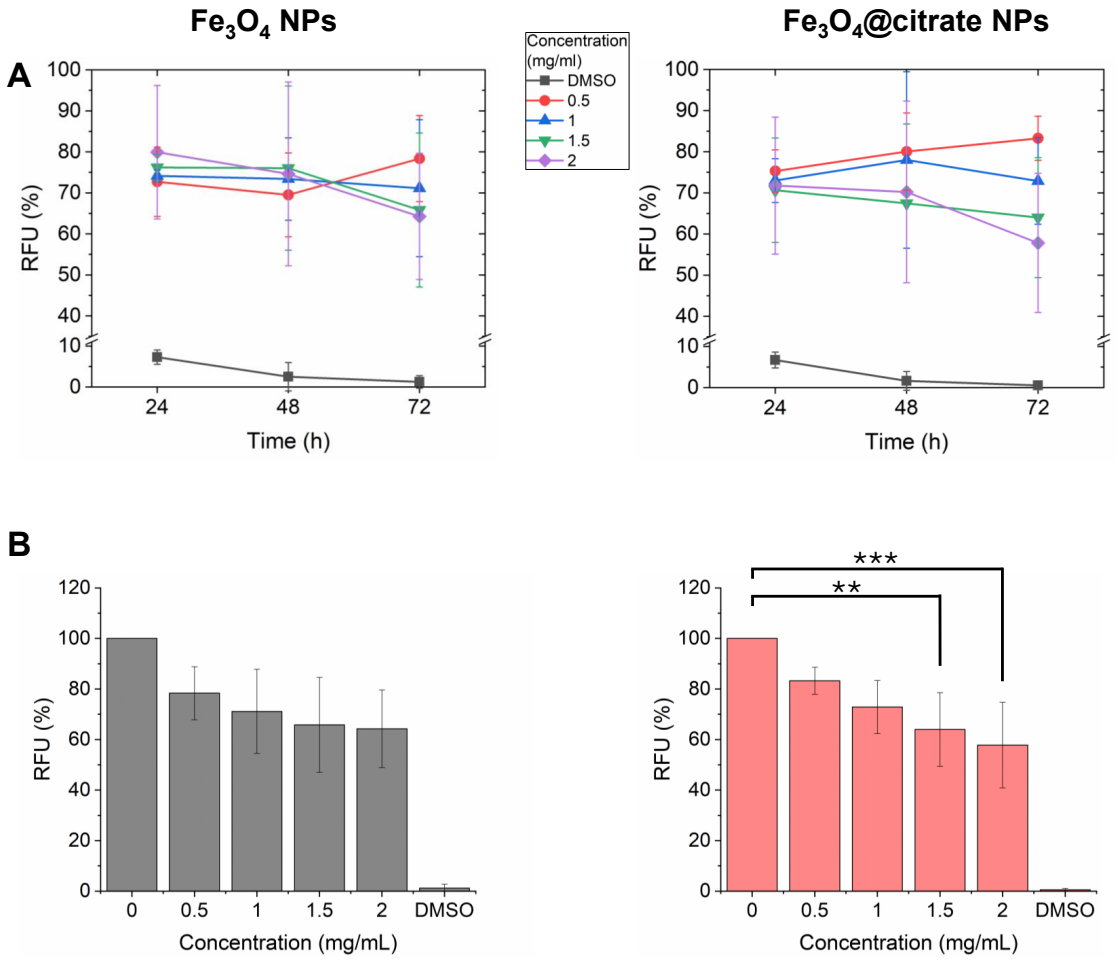



**Figure 4.2.** Cell viability assessment on A549 cell cultures after incubation with uncoated (left) and citrate-coated (right) $Fe_3O_4$ NPs. (**A**) Cell viability after 24, 48, and 72 h of treatment with different concentrations of $Fe_3O_4$ NPs, in the range 0-2 mg/mL, dissolved in the culture medium. (**B**) Histograms of cell viability at 72 h of treatment. Cell viability is evaluated using the resazurin assay and is quantified as a percentage of relative fluorescence units (RFU). In both cases, the reported data are normalized with respect to the control (without NP treatment), which is considered as 100%. RFU data are indicated as mean ± SD (biological replicate n° = 3). All the analyses with a $p$-value $< 0.05$ were indicated as statistically significant ($^*p \leq 0.05$; $^{**}p \leq 0.01$; $^{***}p \leq 0.001$; $^{****}p \leq 0.0001$).

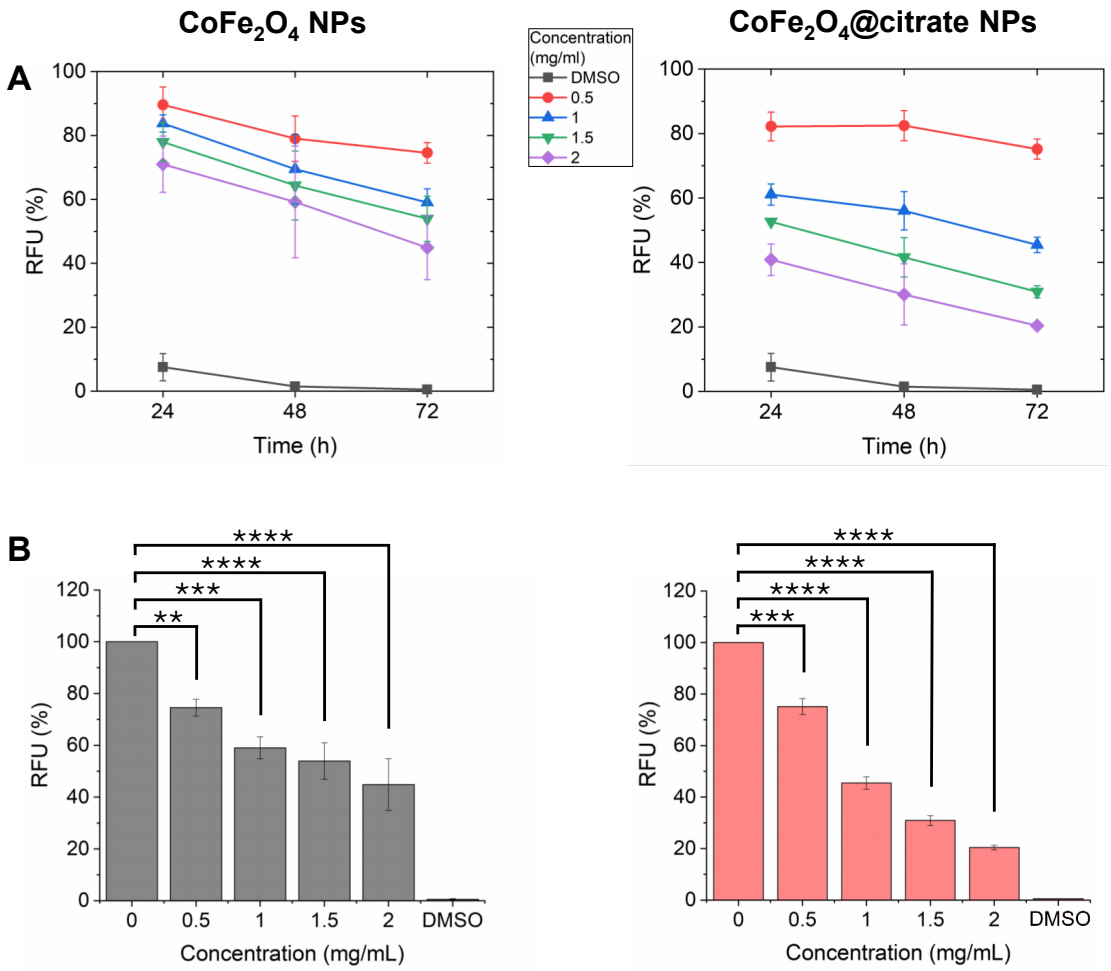



**Figure 4.3.** Cell viability assessment on A549 cell cultures after incubation with uncoated (left) and citrate-coated (right) $CoFe_2O_4$ NPs. (**A**) Cell viability after 24, 48, and 72 h of treatment with different concentrations of $CoFe_2O_4$ NPs, in the range 0-2 mg/mL, dissolved in the culture medium. (**B**) Histograms of cell viability at 72 h of treatment. Cell viability is evaluated using the resazurin assay and is quantified as a percentage of relative fluorescence units (RFU). In both cases, the reported data are normalized with respect to the control (without NP treatment), which is considered as 100%. RFU data are indicated as mean ± SD (biological replicate n° = 3). All the analyses with a $p$-value $< 0.05$ were indicated as statistically significant ($^*p \leq 0.05$; $^{**}p \leq 0.01$; $^{***}p \leq 0.001$; $^{****}p \leq 0.0001$).

### 4.2.2 *In vitro* magnetic hyperthermia tests

Several studies in the literature have investigated the effects of *in vitro* magnetic hyperthermia, providing insights into its impact on cellular viability. These studies vary in terms of the cell lines used, the types and concentrations of MNPs analyzed, and the parameters of the AC magnetic field applied during the treatment. Additionally, differences exist in the treatment protocols, including single or repeated exposures to the AC magnetic field over time. [171] However, they generally follow a similar procedure, involving cell incubation with specific MNP concentrations followed by exposure to an AC magnetic field. [167–173]
Most of the studies do not take into account important aspects that can affect cellular viability during magnetic hyperthermia treatments. Some papers solely assess the effect of temperature on cell lines by immersing them in a thermal bath with a temperature in the range 42-50 °C for varying durations, without the use of MNPs for heat generation. Other studies conduct similar experiments by heating cells in an incubator at 45 °C in the presence of known MNP concentrations, although these MNPs are not utilized for heat generation. [168, 169] Furthermore, some studies evaluate effects on cellular viability only 24 h after magnetic hyperthermia treatment, without examining longer-term effects. [168–171] Finally, some studies achieve high cellular mortality rates, up to nearly 90%, [173] but employ field parameters exceeding the Hergt-Dutz limit. [70, 71] Conversely, certain studies demonstrate significant efficacy, reducing cellular viability by 50% with very low MNP concentrations of 0.1 mg/mL. [167]
A noteworthy study focuses on evaluating the effects of magnetic hyperthermia induced by MNPs internalized within cells or in close proximity to them. [172] To achieve this, following the incubation of cells with MNPs, the cells are washed with PBS, and excess MNPs within the culture medium are removed via centrifugation. Subsequently, the suspended cells are exposed to the AC magnetic field. However, this study presents some issues due to the experimental setup involving suspended cells, which deviates even further from physiological conditions compared to adherent cell cultures. Additionally, the potential loss of cells during the washing and reseeding of cell cultures after field exposure is not taken into account.
To account for all these variables, two different experiments are presented in this section. The Experiment#1 aims to test the effects of magnetic hyperthermia on cells incubated for 24 h with MNPs and exposed to the AC magnetic field for 30 min. This experiment is conducted to compare the results with those found in the literature, although cellular viability is assessed up to 48 h post-treatment. No distinction is made between internalized MNPs and MNPs in the extracellular environment.
The Experiment#2, on the other hand, focuses on evaluating the effects of magnetic hyperthermia induced solely by MNPs internalized within cells or closely associated with cell membranes. To assess these effects, a protocol is developed, as described

in Figure 4.4, involving cells incubated for 40 h with MNPs, a duration demonstrated sufficient for their internalization into the cytoplasm, followed by washing to remove excess MNPs from the culture medium. The cells are reseeded for adherence and incubated overnight. Subsequently, cellular viability is evaluated to account for potential cell loss during washing, and the cells are then exposed to the AC magnetic field for 60 min. Finally, cellular viability is assessed 72 h after magnetic hyperthermia treatment.
Both *in vitro* magnetic hyperthermia experiments are conducted using both uncoated and citrate-coated $Fe_3O_4$ NPs, excluding $CoFe_2O_4$ NPs, as they have not demonstrated good biocompatibility in previous tests.

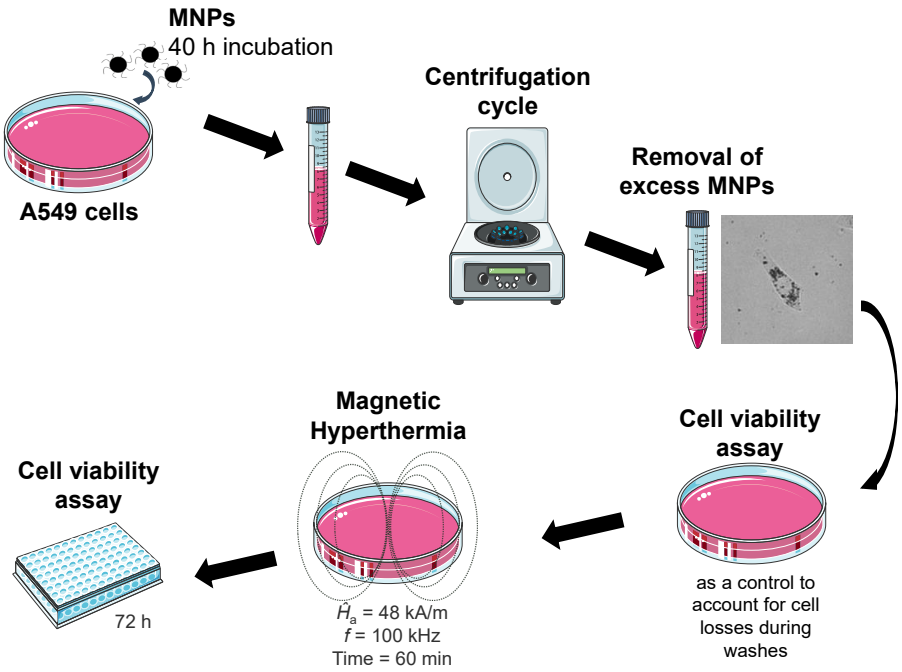



**Figure 4.4.** Schematic of Experiment#2 conducted to evaluate the effects of magnetic hyperthermia induced by MNPs internalized within the cellular cytoplasm or closely associated with cell membranes.

Before conducting magnetic hyperthermia experiments, preliminary analyses are performed to exclude temperature rises resulting from exposure to the AC magnetic field of the cell culture medium (DMEM) and to assess temperature variations induced by the presence of MNPs. Furthermore, these tests enable us to determine the necessary MNP concentration to achieve the desired temperature. Figure 4.5 presents temperature curves obtained by exposing samples of deionized water, DMEM, and suspensions of $Fe_3O_4$ NPs, with and without citrate coating, to the AC magnetic field. Temperature measurements for all the samples are collected

in containers used for magnetic hyperthermia treatment on cell cultures. Additionally, equilibrium temperature ($T_{eq}$) and $\Delta T$ values obtained for DMEM suspensions of MNPs with different concentrations are reported in Table 4.1 and Figure 4.6. When exposed to the AC magnetic field, DMEM exhibits no significant heating compared to deionized water, as demonstrated in Figure 4.5A. Thus, it is possible to exclude the occurrence of eddy current effects due to the presence of salts in the sample during exposure to the field. This confirms that DMEM is a suitable culture medium for conducting these experiments as it does not raise the sample temperature. The increase in temperature of deionized water, as well as of DMEM, is due to the Joule effect of the coil when it is powered with alternating current. Conversely, preliminary experiments conducted with suspensions of MNPs in DMEM show a temperature increase with increasing concentration, tested in the range of 0.1-2 mg/mL, as depicted in Figure 4.5B-C and Table 4.1. Particularly, as illustrated in Figure 4.5B, the lowest concentration of 0.1 mg/mL does not differ much from the sample with only DMEM, although a slight temperature increase is notable in the case of citrate-coated $Fe_3O_4$ NPs compared to the uncoated ones; this phenomenon aligns with the SLP values for the MNP samples obtained in Chapter 2. On the other hand, with the highest concentration of 2 mg/mL, a $T_{eq}$ of 42.6 °C is observed after 30 min of exposure to the AC magnetic field, corresponding to a $\Delta T$ of 20.8 °C, as reported in Table 4.1.

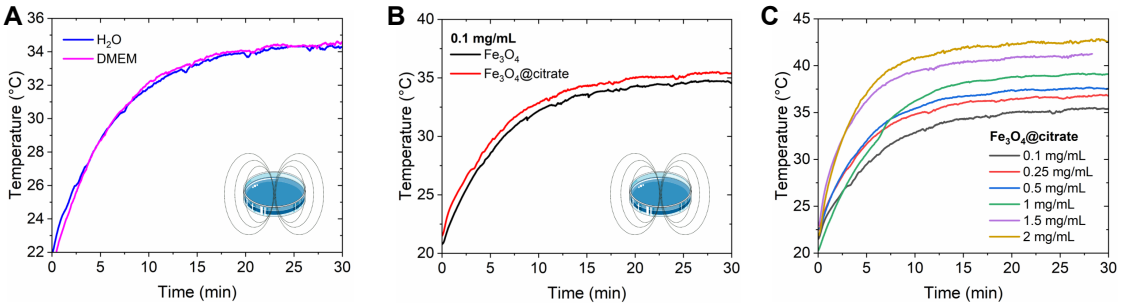



**Figure 4.5.** Time evolution of the temperature of 0.4 mL of (**A**) distilled water and DMEM, (**B**) $Fe_3O_4$ NP solutions in DMEM at concentration of 0.1 mg/mL, with and without citrate coating, and (**C**) $Fe_3O_4$ NP solutions in DMEM with citrate coating at different concentrations (in the range 0.1-2 mg/mL) contained in the containers used for magnetic hyperthermia treatment under the exposure of the AC magnetic field. In all reported conditions, the AC magnetic field has a peak amplitude of 48 kA/m and a frequency of 100 kHz.

**Table 4.1.** Initial temperature ($T_i$), equilibrium temperature ($T_{eq}$) and temperature variation ($\Delta T$) values for different concentrations of citrate-coated $Fe_3O_4$ NPs dispersed in DMEM, exposed to an AC magnetic field with a peak amplitude of 48 kA/m and a frequency of 100 kHz for 30 min.

| **Concentration** [mg/mL] | $T_i$ [°C] | $T_{\mathbf{eq}}$ [°C] | $\Delta T$ [°C] |
|---|---|---|---|
| 0.1 | 20.8 | 34.8 | 14.0 |
| 0.25 | 22.5 | 36.8 | 14.3 |
| 0.5 | 22.6 | 37.6 | 15.0 |
| 1 | 20.3 | 38.8 | 18.5 |
| 1.5 | 22.4 | 41.3 | 18.9 |
| 2 | 21.8 | 42.6 | 20.8 |

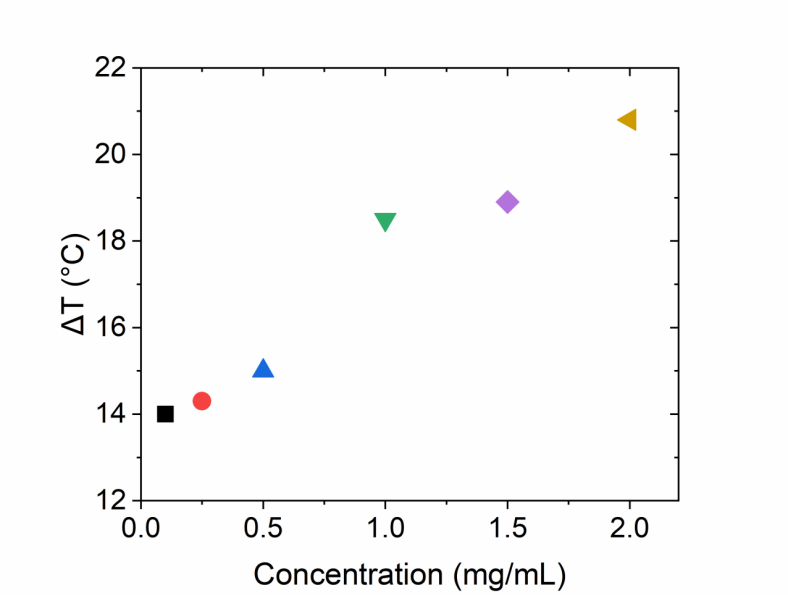



**Figure 4.6.** Temperature variation ($\Delta T$) values for different concentrations of citrate-coated $Fe_3O_4$ NPs, exposed to an AC magnetic field with a peak amplitude of 48 kA/m and a frequency of 100 kHz for 30 min.

Based on the results obtained from these preliminary tests, it has been decided to utilize a concentration of 1.5 mg/mL of MNPs dispersed in DMEM for conducting the *in vitro* magnetic hyperthermia experiments. This concentration enables reaching a $T_{eq}$ of 41.3 °C, corresponding to a $\Delta T$ of 20.8 °C in the magnetic solution.

Figure 4.7 presents the results obtained from *in vitro* magnetic hyperthermia treatment using MNPs dispersed in the culture medium (Experiment#1). The experiment is conducted on four different samples: a control group consisting of untreated cells, a group treated with an AC magnetic field in the absence of MNPs to assess

the potential effects of the magnetic field on cellular viability, and two groups incubated with two different $Fe_3O_4$ NPs samples (uncoated and citrate-coated). All samples, except the control, are subjected to an AC magnetic field with a peak amplitude of 48 kA/m and a frequency of 100 kHz for 30 min. Subsequently, cell viability data are collected using the resazurin assay at 24 and 48 h post-treatment. The data are normalized to the control, which is set to 100% cell viability. As illustrated in the results, cells exposed to the AC magnetic field without MNPs do not show negative effects on cell viability; a slight increase in viability is observed. Conversely, both the samples treated with uncoated and citrate-coated $Fe_3O_4$ NPs and exposed to the AC magnetic field exhibit a reduction in cell viability by more than 80% after 24 h and exceeding 90% after 48 h. Unfortunately, the data reported represent a single experiment, as other replicates are unfeasible at the time of thesis writing due to malfunctioning of the experimental setup utilized for generating the AC magnetic field.

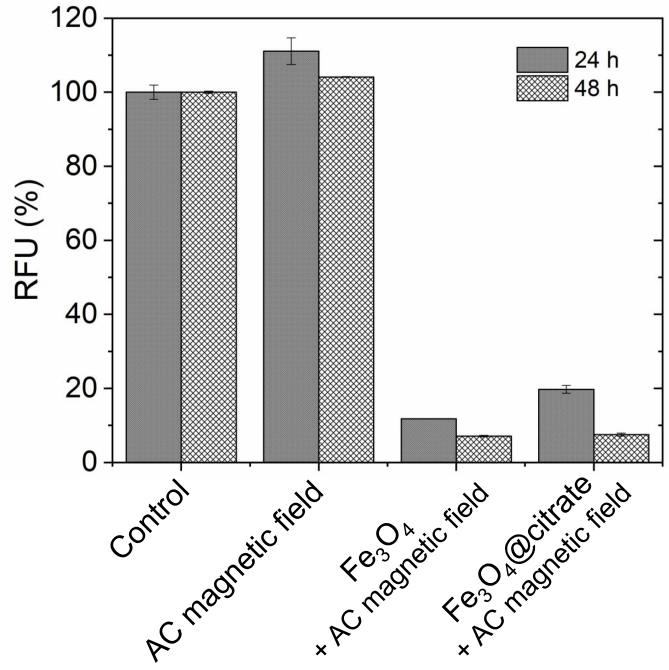



**Figure 4.7.** Cellular viability assessment on A549 cell cultures following magnetic hyperthermia treatment with 1.5 mg/mL of uncoated and citrate-coated $Fe_3O_4$ NPs dispersed in the culture medium (Experiment#1). Cellular viability is evaluated using the resazurin assay at 24 and 48 h after a 30-min exposure to an AC magnetic field with a peak amplitude of 48 kA/m and a frequency of 100 kHz; the data are reported as a percentage of relative fluorescence units (RFU) normalized with respect to the control (untreated cells), which is set at 100%. RFU data are indicated as the mean ± SD of three technical replicates. Additionally, a control sample exposed to the AC magnetic field in the absence of MNPs is included to evaluate the potential effects of the magnetic fields on the cells.

Figure 4.8 illustrates the outcomes following magnetic hyperthermia treatment *in vitro* induced by MNPs internalized within the cellular cytoplasm or closely associated with cellular membranes. The experiment is conducted using both uncoated and citrate-coated $Fe_3O_4$ NPs (i.e. using experimental methodology #2). Additionally, cell samples treated with MNPs but not exposed to the AC magnetic field served as controls. Specifically, cells are incubated with MNPs, washed to remove excess nanoparticles, and then reseeded. Subsequently, cellular viability is assessed to account for any cell loss during washing and reseeding, and the treatment samples are exposed to an AC magnetic field with a peak amplitude of 48 kA/m and a frequency of 100 kHz for 1 hour. Cellular viability data are collected using the resazurin assay at 72 h post-treatment, normalized relative to cellular viability measured before magnetic hyperthermia treatment, and further normalized relative to the control (cells treated with MNPs but not exposed to the AC magnetic field), which exhibited 100% cellular viability, as depicted in Figure 4.8. As evident from the results obtained, both uncoated and citrate-coated $Fe_3O_4$ NPs exhibit a drastic reduction in cellular viability following exposure to the AC magnetic field compared to control samples merely in contact with MNPs without magnetic field exposure. Specifically, $Fe_3O_4$ NPs without coating demonstrate an approximately 80% reduction in cellular viability after 72 h post-treatment, whereas those with citrate coating exhibit a reduction of approximately 99%. Also in this case, the data reported represent a single experiment, as other replicates are unfeasible at the time of thesis writing due to malfunctioning of the experimental setup utilized for generating the AC magnetic field.

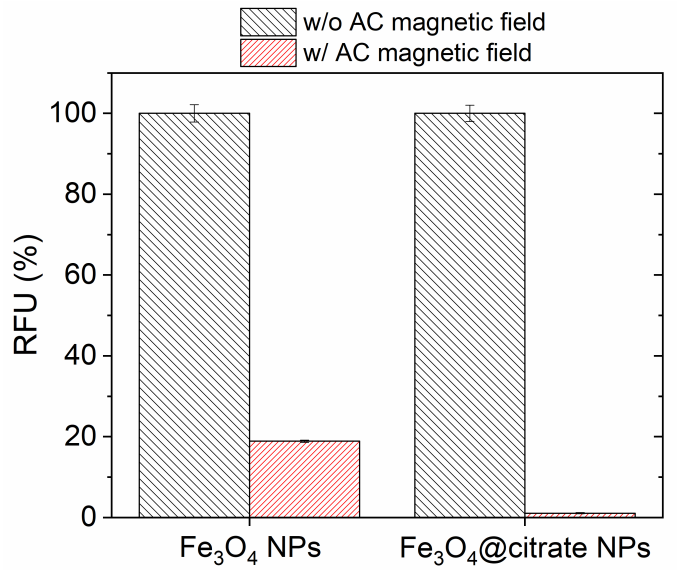



**Figure 4.8.** Cellular viability assessment on A549 cell cultures following magnetic hyperthermia treatment induced by MNPs internalized within the cellular cytoplasm or closely associated with cell membranes (Experiment#2). The experiment is conducted with both uncoated and citrate-coated $Fe_3O_4$ NPs. Cellular viability is evaluated using the resazurin assay at 72 h after a 1-h exposure to an AC magnetic field with a peak amplitude of 48 kA/m and a frequency of 100 kHz; the data are reported as a percentage of relative fluorescence units (RFU) normalized with respect to the control (cells treated with MNPs but not exposed to the AC magnetic field), which is set at 100%. RFU data are indicated as the mean ± SD of three technical replicates.

## 4.3 Conclusions

In this Chapter, we evaluated the cytotoxicity of $Fe_3O_4$ and $CoFe_2O_4$ NP samples on cell cultures. Our findings indicate that $Fe_3O_4$ NPs exhibit significantly higher biocompatibility compared to $CoFe_2O_4$ NPs. Additionally, the presence of citrate coating, especially on $CoFe_2O_4$ NPs, increases the negative effects on cell viability. Consequently, subsequent *in vitro* hyperthermia experiments were conducted exclusively on $Fe_3O_4$ NP samples.
Before initiating the cell experiments, we performed a study to determine the optimal MNP concentration for achieving the desired temperatures for magnetic hyperthermia, which was found to be 1.5 mg/mL. Initial hyperthermia experiments conducted on cells in culture medium containing 1.5 mg/mL of MNPs demonstrated a notable decrease in cell viability for both samples (with and without coating of citrate).
Furthermore, this Chapter presented an *in vitro* magnetic hyperthermia protocol to assess the effects of heat generated by internalized nanoparticles or those in

close contact with cell membranes, aiming to better mimic physiological conditions. These experiments also showed effective cell mortality induction, with a greater reduction in cell viability observed for the $Fe_3O_4$ sample with citrate coating. This aligns with the higher SLP value for this sample, indicating enhanced efficacy in reducing cell viability through magnetic hyperthermia.
From a future perspective, the results obtained for the *in vitro* magnetic hyperthermia experiments on cell cultures need further investigation to ensure the validity of the data by conducting other replicates. Additionally, it would be valuable to explore the response of other cell lines to this treatment and to investigate whether subjecting cells to repeated sessions of magnetic hyperthermia could potentially reduce the dosages of MNPs used. Furthermore, another goal would be to assess the level of MNP internalization within the cells using a quantitative method based on fluorescence imaging.

# Chapter 5

# Magnetic oxygen-loaded nanodroplets

In this Chapter, $Fe_3O_4$ NPs are employed to decorate the surface of oxygen-loaded nanodroplets (OLNDs), nanocarriers designed to transport and release oxygen for drug delivery applications, particularly in the treatment of hypoxic tissues. [85] These nanovectors are based on a fluorocarbon core to store oxygen molecules and a polysaccharide coating to provide stability to the nanostructrure. In the literature, OLNDs are activated through ultrasound (US) fields to induce oxygen release. Moreover, previous studies have been conducted to investigate the oxygen-storing capacity of the OLNDs, revealing a loading of 0.45 mg/mL. [73, 80]
In this study, four different samples are employed using two types of coatings, chitosan or dextran, and two types of fluorocarbon cores, decafluoropentante (DFP) or perfluoropentane (PFP), each with distinct boiling points (DFP $- T_{boiling} = 51°C$, PFP $- T_{boiling} = 29°C$). In this work, the magnetic decoration is utilized to harness the heat generated by $Fe_3O_4$ NPs when exposed to an AC magnetic field, inducing the magnetic droplet vaporization (MDV) process, allowing for oxygen release. Thus, the decoration enables the synthesis of dual-responsive nanosystems - magnetic oxygen-loaded nanodroplets (MOLNDs) - for controlled oxygen release via both ultrasound and magnetic stimulations. A comprehensive physicochemical characterization is conducted to investigate the effects of $Fe_3O_4$ NP inclusion on the nanodroplet properties. Furthermore, experiments are performed to assess the effectiveness of the magnetic decoration and to evaluate the oxygen release induced by MDV. Finally, *in vitro* cytotoxicity tests are conducted to investigate the biocompatibility of these nanohybrid systems.

The content of this Chapter has been published in:

[88] *S. Galati, M. Vassallo, M. Vicentini, M. Vallino, F. Celegato, G. Barrera, D. Martella, E. S. Olivetti, A. Sacco, J. Petiti, C. Divieto, P. Tiberto, A. Manzin,*

*A. Troia. Dual-responsive magnetic nanodroplets for controlled oxygen release via ultrasound and magnetic stimulation.* Nanoscale, ***2024**, 16, 1711-1723.*

Further investigations regarding the acoustic response of OLND and MOLND samples, numerical modeling of the MOLND behavior under a magnetic field gradient, and the analysis of the oxygen release stimulated by US field have been reported in Appendix B.

## 5.1 Materials and Methods

### 5.1.1 Reagents

PVP, and palmitic acid were obtained from Fluka (Buchs, Switzerland). Epikuron 200 (soya phosphatidylcholine 95%) was purchased from Degussa (Hamburg, Germany). DFP, PFP, chitosan (low molecular weight), dextran, heat-inactivated FBS, and penicillin-streptomycin were obtained from Sigma-Aldrich (St Louis, Missouri, USA). Uranyl acetate was purchased from Electron Microscopy Sciences (Hatfield, Pennsylvania, USA). High glucose (1 g/L) DMEM w/o L-glutamine w/ sodium pyruvate was obtained from Biowest (Nuaillé, France). 200 mM L-glutamine was purchased from Lonza (Basel, Switzerland). Resazurin sodium salt was obtained from Invitrogen by Thermo Fisher Scientific (Waltham, Massachusetts, USA). All chemicals were used without further purification.

### 5.1.2 Synthesis of oxygen-loaded nanodroplets and decoration with $Fe_3O_4$ NPs

For the synthesis of the liquid formulation of OLNDs, DFP or PFP (1.5 mL), an aqueous solution of polyvinylpyrrolidone (0.5 mL, 0.5%), and a solution of Epikuron 200 (1.8 mL, 1%) solved in a solution of ethanol (1%) and palmitic acid (0.3%) were added to 30 mL deionized water. The mixture was homogenized for 2 min at 24000 rpm in an ice bath using the IKA Ultra-Turrax SG215 homogenizer (Staufen, Germany). Then, the suspension was saturated with a flow of $O_2$ for 2 min reaching a final $O_2$ concentration of 35 mg/L. Finally, a polymeric solution of chitosan or dextran (1.5 mL, 2.7%) was added dropwise to the mixture during the final homogenization process at 13000 rpm for 2 min in an ice bath.
The MOLND samples were obtained by the magnetic decoration of OLNDs, described above, with $Fe_3O_4$ NPs, whose synthesis and characterization were detailed in Chapter 2. [38] To obtain a formulation of MOLNDs, $Fe_3O_4$ NPs were dispersed in the same solution used for the OLND preparation, without the fluorocarbon compound (DFP or PFP). The mixture was added to the OLNDs suspension to reach a final concentration of $Fe_3O_4$ NPs of 1 mg/mL. Lastly, the mixture was

sonicated for 20 s in an ice bath to facilitate magnetic functionalization, ultimately leading to the synthesis of MOLNDs.

### 5.1.3 Characterization

#### Physicochemical characterization

The morphology of the nanodroplet samples was evaluated by SEM, with an Inspect - F microscope (FEI, Hillsboro, Oregon, USA) employing backscattered electron imaging, and by TEM, using an 80 kV Philips CM 10 microscope (Philips Electronics, Eindhoven, Netherlands). To prepare samples for SEM, a nanodroplet suspension was drop-cast onto a silicon substrate and evaporated at room temperature. This step was pivotal in ensuring the sample stability and integrity under the high-vacuum conditions within the SEM chamber. For TEM sample preparation, a drop of the suspension was placed on a Pelco® carbon and formvar-coated grid, left to adsorb for 5 min, and subsequently rinsed several times with deionized water. Lastly, the grid was negatively stained using a 0.5% (w/v) aqueous uranyl acetate solution.
The hydrodynamic size distribution and $\zeta$ potential of the nanodroplets were assessed at room temperature using the Zetasizer Ultra instrument (Malvern Panalytical, Malvern, UK) through DLS. The calculation of the mean hydrodynamic diameter focused only on values falling within the range of 100–900 nm from the size distributions. Values outside this range were disregarded, as they represented either residual reagents from the synthesis process ($< 100$ nm) or microbubbles that underwent spontaneous vaporization ($> 900$ nm), especially in the case of PFP due to its lower vaporization threshold ($T_{boiling} = 29\ °C$).

#### Assessment of magnetic decoration

To confirm the successful decoration of OLNDs with $Fe_3O_4$ NPs, we examined the magnetic behavior of the resulting MOLNDs in terms of streaming trajectory when subjected to a magnetic field gradient generated by a permanent magnet. This investigation involved the utilization of two distinct experimental setups, as displayed in Figure 5.1.

The first setup (see Figure 5.1A) involves a SonixTouch ultrasonic research scanner (Ultrasonix, Richmond, BC) connected to a SA4-/21 ecographic linear probe (Ultrasonix, Richmond, Canada), and a SU-103 US transducer (Sonic Concepts, Bothell, Washington, USA), operating at 3.3 MHz, with the focus precisely at the center of the parallelepipedal sample holder containing the nanodroplet suspension. With this setup, the experiment was conducted by recording frames of MOLND samples moving under exposure to US field and after the switching off of excitation, in the presence or absence of the magnet. Then, the obtained frames underwent post-processing using the tracking plug-in of ImageJ software [123], and

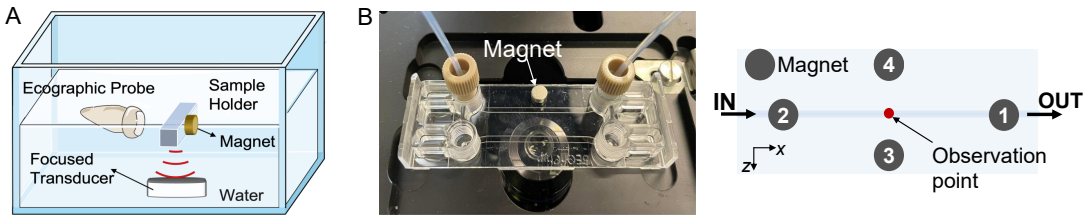



**Figure 5.1.** (**A**) Visual representation of the setup employed to observe the droplet behavior using an ecographic imaging probe, in the absence and presence of a magnet. (**B**) Image and schematic of the microfluidic setup designed to examine MOLND trajectories under the influence of a magnet, located in four distinct positions.

the droplet streaming velocity was extrapolated. Each average value was derived from 30 measurements.
The second setup (see Figure 5.1B) consists of a Flow EZ microfluidic pump (Fluigent, Le Kremlin-Bicêtre, France) utilized to create a laminar flow within a Be-Flow single microchannel chip (BEOnChip, Fluigent, Le Kremlin-Bicêtre, France), which possesses a rectangular cross-section and its specific details are provided in Table 5.1. A IX73 optical microscope (Olympus, Tokyo, Japan) connected to an external camera is employed to capture the passage of MOLNDs. In this case, the experiment is based on observing the trajectory of MOLND samples within the microchannel in the absence and presence of a magnetic field gradient by placing a magnet in four different positions, as illustrated in Figure 5.1B. From the frames recorded at the observation point, located at the center of the channel where an average flow between the inlet (11 $\mu$L/min) and outlet (8.5 $\mu$L/min) values is assumed, the trajectories of the MOLNDs under various experimental conditions were tracked and processed using the ImageJ software tracking plugin [123]. Streaming velocities and deflection angles of the nanodroplets were thus estimated and each average value was obtained from 30 measurements.
The magnetic field gradient used in the two setups described above is generated by two different magnets, both with a disk shape and magnetized out-of-plane. The characteristics of these magnets are detailed in Table 5.2, while Table 5.3 reports the magnetic field produced by the magnets at different points along a line orthogonal to the magnet plane.

**Table 5.1.** Dimensions of the microchannel (BeFlow, BEOnChip) utilized in the microfluidic setup.

| **Height** [$\mu$m] | **Width** [mm] | **Lenght** [mm] | **Total volume** [$\mu$L] |
|---|---|---|---|
| 375 | 1.5 | 43 | 28.5 |

**Table 5.2.** Composition and dimensions of the magnets used to generate magnetic field gradients.

| **Magnet** | **Composition** | **Diameter** [mm] | **Thickness** [mm] |
|---|---|---|---|
| Setup A | NdFeB | 12 | 6 |
| Setup B | NdFeB | 5 | 2 |

**Table 5.3.** Magnetic field generated by the magnets as a function of the distance. The measurements are performed with a hole probe.

| **Magnet A** | | **Magnet B** | |
|---|---|---|---|
| Distance [mm] | Magnetic field [T] | Distance [cm] | Magnetic field [T] |
| 4 | 0.160 | 0 | 0.256 |
| 6 | 0.111 | 2 | 0.056 |
| 10 | 0.044 | 6 | 0.013 |

### 5.1.4 Oxygen release through magnetic droplet vaporization

The magnetic droplet vaporization process of MOLNDs was induced by exposing the sample to an AC magnetic field, generated by a custom-built setup (shown in Figure 5.2) capable of producing a uniform field with a peak amplitude of 72 kA/m and a frequency of 100 kHz. Specifically, the experiment was conducted by placing 1 mL of the sample in a test tube within a thermally insulated support, and the magnetic field was switched on while monitoring the temperature of the suspension with a PRB-G20 fiber optic thermometer (Osensa Innovation, Burnaby, Canada). The treatment was halted at specific temperatures based on the boiling points of the fluorocarbon cores: 25, 27, 29, and 37 °C for MOLNDs with PFP-core, and 37, 45, 48, and 51 °C for MOLNDs with DFP-core. Then, the sample was promptly examined under an ARISTOMET optical microscope (Leitz, Ostfildern, Germany) to verify the existence of vaporized bubbles, confirming the magnetic droplet vaporization occurrence.
The oxygen release due to the magnetic droplet vaporization process was assessed using a NEOFOX-GT oximeter (Ocean Insight, Orlando, Florida, USA) equipped with a small optical fiber probe (3 mm). Oxygen levels in the samples were measured for 5 min before and after the vaporization process. To ensure accuracy, the sample holder remained tightly sealed throughout the measurement, facilitating the attainment of saturation equilibrium within the suspension. This allowed for the determination of oxygen variations with respect to the initial concentrations.

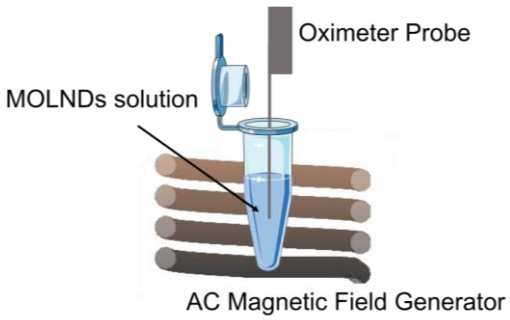



**Figure 5.2.** Visual depiction of the experimental system to evaluate oxygen release induced by the AC magnetic field stimulus.

### 5.1.5 *In vitro* test of cytotoxicity

#### Cell culture

A549 human lung cancer cell line (ATCC CCL-185) was purchased from the American Type Culture Collection. The cells were cultured in high glucose (1 g/L) DMEM, without L-Glutamine, and with sodium pyruvate. The culture medium was supplemented with 10% (v/v) FBS, 1% (v/v) L-glutamine, and 1% (v/v) penicillin/streptomycin. The cell cultures were incubated at 37 °C with 5% $CO_2$. Cells were counted using the Neubauer cell counting chamber to determine the cell concentration.

#### Analysis of biocompatibility of magnetic oxygen loaded nanodroplets

The cell viability was determined using the resazurin assay, which is detailed in Chapter 4 (Section 4.1.3).
The biocompatibility was tested for 72 h at four different dilutions of MOLND samples in the culture medium: 1:20, 1:10, 1:8, and 1:5. These concentrations were selected to make them comparable to existing studies in the literature. [80, 93]
For the cytotoxicity test, cells were seeded in 48-well plates (15,000 cells/well) and incubated overnight under standard conditions. Subsequently, the cells were treated with MOLND samples and cell viability was assessed after 24, 48, and 72 hours of treatment. Cells in only medium were used as control and each treatment group consisted of 3 replicates.
A 44 µM solution of resazurin in complete DMEM was freshly prepared before each experiment. After the culture medium was removed, 250 µL of resazurin solution was added to each well, and the cells were incubated for 1.5 h. Then, the metabolized resazurin solution was collected and transferred to a 96-well plate for fluorescence intensity (FI) measurement. FI measurements were performed using

the Spark multimode microplate reader (Tecan, Hombrechtikon, Switzerland) using an excitation wavelength ($\lambda_{Ex}$) of 545 nm and an emission wavelength ($\lambda_{Em}$) of 595 nm. [163–165] For each experiment, the RFU (Relative Fluorescence Units) was collected and results from samples treated with MOLNDs were normalized on the control sample (without MOLNDs), considered as 100% viability. Therefore, the results were expressed as a percentage of cell viability with respect to the control sample.

### Statistical analysis

The data were presented as the mean ± SD obtained from three biological replicates. Differences in cell viability between treated and untreated control cells were determined using one-way ANOVA with Tukey's post-hoc multiple comparison test. Differences were considered statistically significant at $p$-value $< 0.05$: $^{*}p \leq 0.05$; $^{**}p \leq 0.01$; $^{***}p \leq 0.001$; $^{****}p \leq 0.0001$.

## 5.2 Results and Discussion

### 5.2.1 Synthesis of oxygen-loaded nanodroplets and magnetic decoration

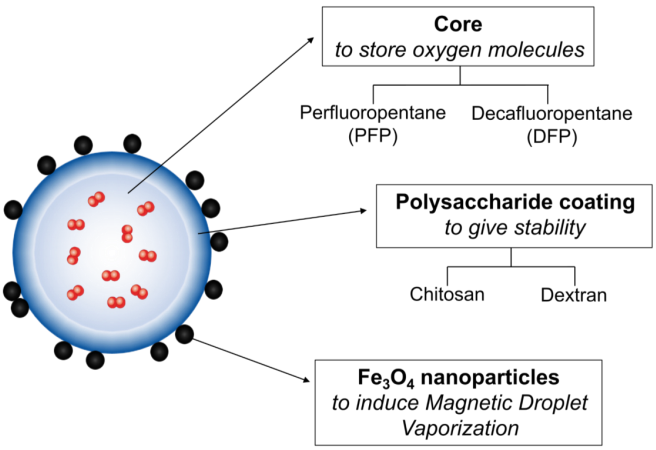



**Figure 5.3.** Schematic representation of MOLND structure.

As depicted in Figure 5.3, four distinct batches of OLNDs were produced in the liquid phase employing the sonication technique [73, 88], using two distinct fluorocarbons (DFP or PFP) as the core, and two different polymers (dextran or chitosan) as the coating. For each sample, MOLNDs were prepared by surface decoration with $Fe_3O_4$ NPs, whose synthesis and characterization were detailed in Chapter 2. [38]
Initially, the physicochemical properties of the prepared OLNDs and MOLNDs were analyzed through SEM and TEM microscopy. Representative SEM images of the marks left by OLNDs and MOLNDs are presented in Figure 5.4A and 5.4B, respectively, for the DFP-based nanodroplets with chitosan coating. In the SEM image of the OLND sample, distinctive quasi-circular halos with diameters measuring in the hundreds of nanometers are observable. These halos consist of solid residues left on the silicon support by the liquid nanodroplets after their evaporation. Regarding the SEM image of the MOLND sample, clusters of MNPs are observable close to the droplet halos. This observation suggests that the $Fe_3O_4$ NPs localize on the surface of the nanodroplets, indicating a successful magnetic functionalization.
Higher-resolution images were acquired by TEM, as shown in Figure 5.5 for DFP-core MOLNDs with chitosan coating. These images distinctly reveal the existence of aggregates of $Fe_3O_4$ NPs on the nanodroplet surface, validating SEM findings and supporting the efficacy of magnetic decoration.

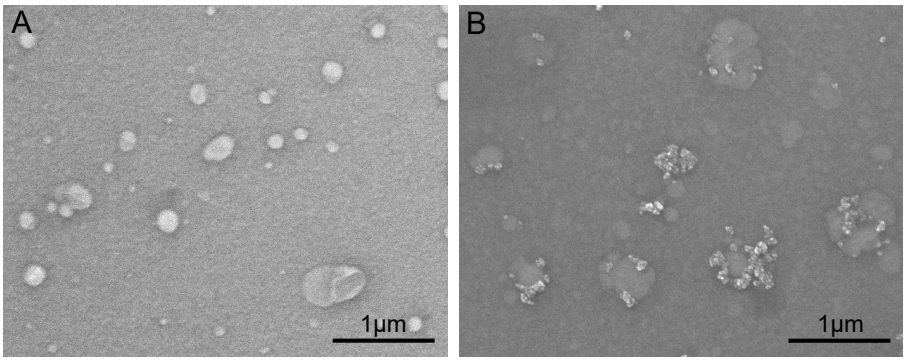



**Figure 5.4.** Representative SEM images of the marks left on a silicon substrate by (**A**) DFP-OLNDs and (**B**) DFP-MOLNDs, both with chitosan coating.

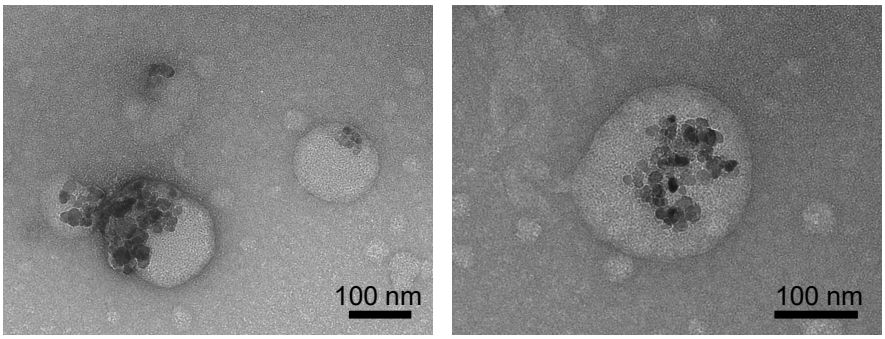



**Figure 5.5.** Representative TEM images of chitosan-coated DFP-MOLNDs.

The hydrodynamic size distributions obtained through DLS are depicted in the histograms in Figure 5.6, accompanied by their corresponding mean values and standard deviations derived from five measurements, as detailed in Table 5.4. The results suggest that the sizes of OLNDs with distinct cores (DFP or PFP) are comparable, therefore, the fluorocarbon composition does not significantly affect their dimension. [73] Conversely, the choice of coating impacts on the size of the droplets, as evidenced by the larger diameter of OLNDs coated with chitosan compared to those coated with dextran. Additionally, the surface decoration of OLNDs with $Fe_3O_4$ NPs is affirmed by an increase in their mean size, irrespective of the core and coating used.
Table 5.4 also presents the mean $\zeta$ potential values and their corresponding standard deviations for each sample, calculated based on five measurements. The choice of the coating agent significantly affects the $\zeta$ potential, leading to a positive value with chitosan and a negative one with dextran. Additionally, $Fe_3O_4$ NPs display a negative $\zeta$ potential, potentially leading to a higher MNP loading level with the chitosan coating, as attractive electrostatic forces arise from opposite surface

charges. Moreover, the addition of $Fe_3O_4$ NPs to the surface influences the $\zeta$ potential, resulting in a reduction in its absolute value for MOLNDs compared to their respective OLNDs. This suggests a decrease in the stability of the suspensions.

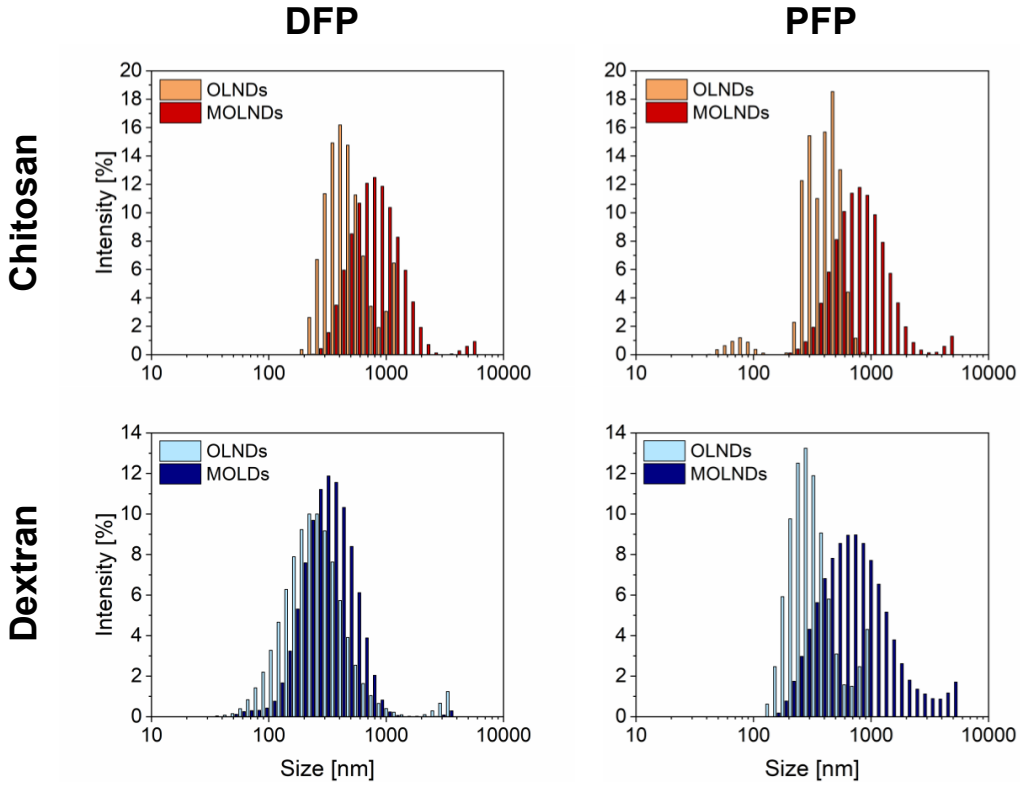



**Figure 5.6.** Hydrodynamic size distributions obtained through DLS for all samples of OLNDs and MOLNDs with both cores, DFP or PFP, and both coatings, chitosan or dextran.

**Table 5.4.** Mean hydrodynamic diameters and $\zeta$ potential values of all the studied samples.

| **Sample** | | | | **Mean hydrodynamic size** [nm] | $\zeta$ **potential** [mV] |
|---|---|---|---|---|---|
| $Fe_3O_4$ NPs | | | | $135 \pm 25$ | $-24.8 \pm 0.5$ |
| | **Core** | **Coating** | **Decoration** | | |
| **OLNDs** | DFP | Chitosan | ✗ | $419 \pm 15$ | $39.5 \pm 2.5$ |
| | | | ✓ | $627 \pm 22$ | $24.7 \pm 1.4$ |
| | | Dextran | ✗ | $285 \pm 16$ | $-21.7 \pm 1.4$ |
| | | | ✓ | $345 \pm 15$ | $-18.4 \pm 0.3$ |
| | PFP | Chitosan | ✗ | $407 \pm 11$ | $54.9 \pm 2.8$ |
| | | | ✓ | $638 \pm 21$ | $40.5 \pm 1.0$ |
| | | Dextran | ✗ | $292 \pm 12$ | $-50.9 \pm 1.8$ |
| | | | ✓ | $563 \pm 25$ | $-25.6 \pm 0.6$ |

### 5.2.2 Assessment of magnetic decoration

Following the physicochemical characterization of the samples, a crucial step involves the characterization of magnetic functionalization, which is essential to induce magnetic droplet vaporization and, consequently, the release of oxygen by MOLNDs. For this purpose, the streaming velocity of MOLNDs was assessed both in the absence and presence of a magnetic field gradient generated by a permanent magnet. Indeed, this parameter, along with trajectory deflections induced by the magnet, provides information about the magnetic response of MOLNDs. Two different setups were employed for this evaluation, as illustrated in Section 5.1.3.
The first experiment involves the excitation of the droplet sample by a US field, collected in a sample holder transparent to ecographic signals. Upon interacting with the acoustic field, MOLNDs are pushed towards fixed positions along the acoustic field lines, specifically nodes and antinodes, where they tend to agglomerate. [191] After the US excitation is turned off, the MOLNDs depart from these fixed points. Their trajectories are recorded in the absence or presence of a magnetic field gradient using an ecographic probe. Representative examples of the frames obtained through the ecographic approach are illustrated in Figure 5.7 and Figure 5.8 for MOLNDs with chitosan and dextran coating, respectively. In the absence of a magnetic field grandient (top sequence), MOLNDs exhibit chaotic motion in all directions over time without a preferential one. In the presence of a magnetic field grandient (bottom sequence), they follow a defined trajectory towards the magnet, as highlighted by green circles.

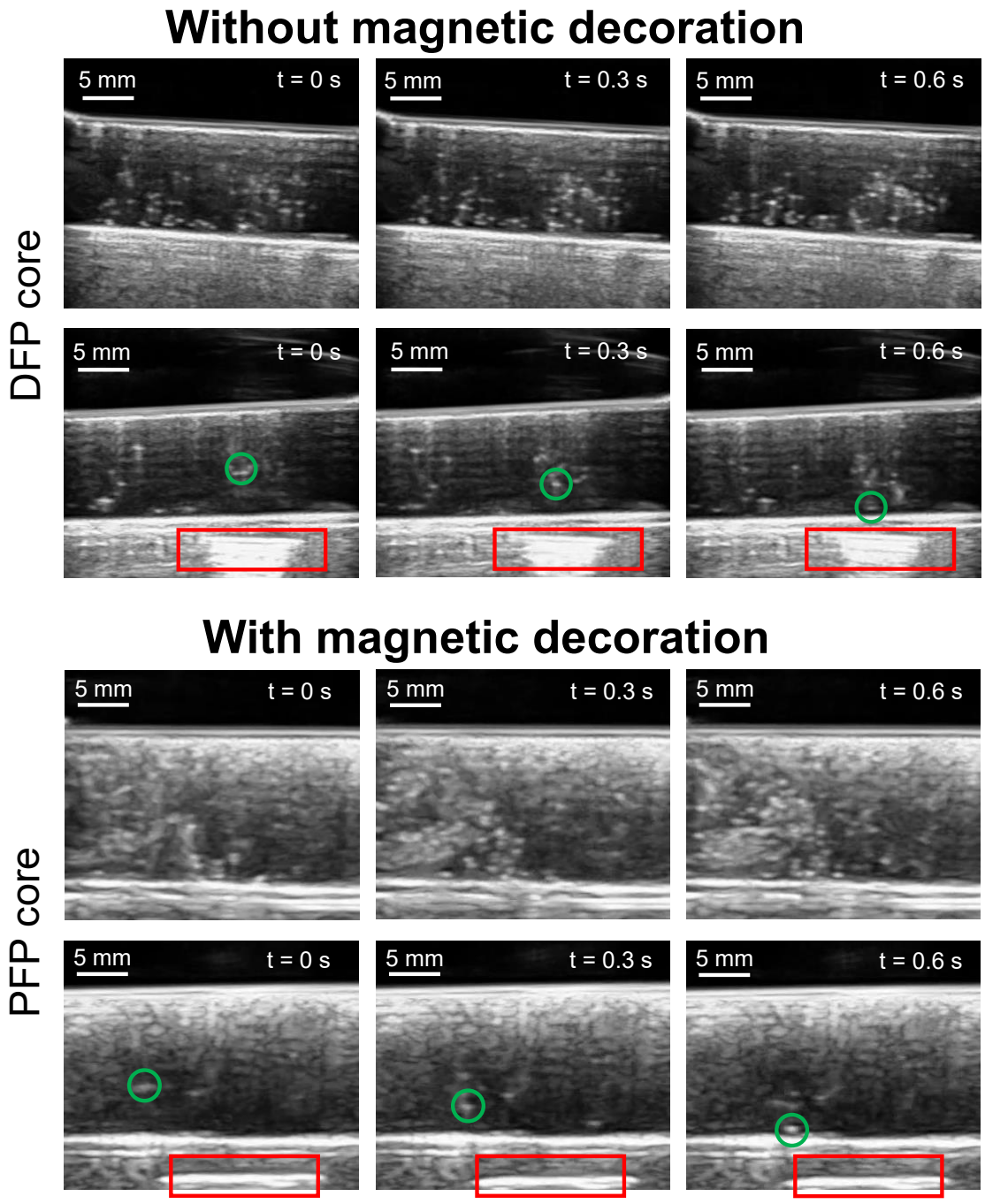



**Figure 5.7.** Frames showing the motion of DFP- or PFP-based MOLNDs with chitosan coating are presented in three subsequent frames following the exposure to a US field. In both cores, the upper sequence illustrates the behavior of droplet samples in the absence of a magnetic field gradient, while the lower sequence shows their behavior in the presence of a magnetic field gradient generated by a permanent magnet, indicated by the red box. Green circles are employed to emphasize the trajectory of a single droplet over time.

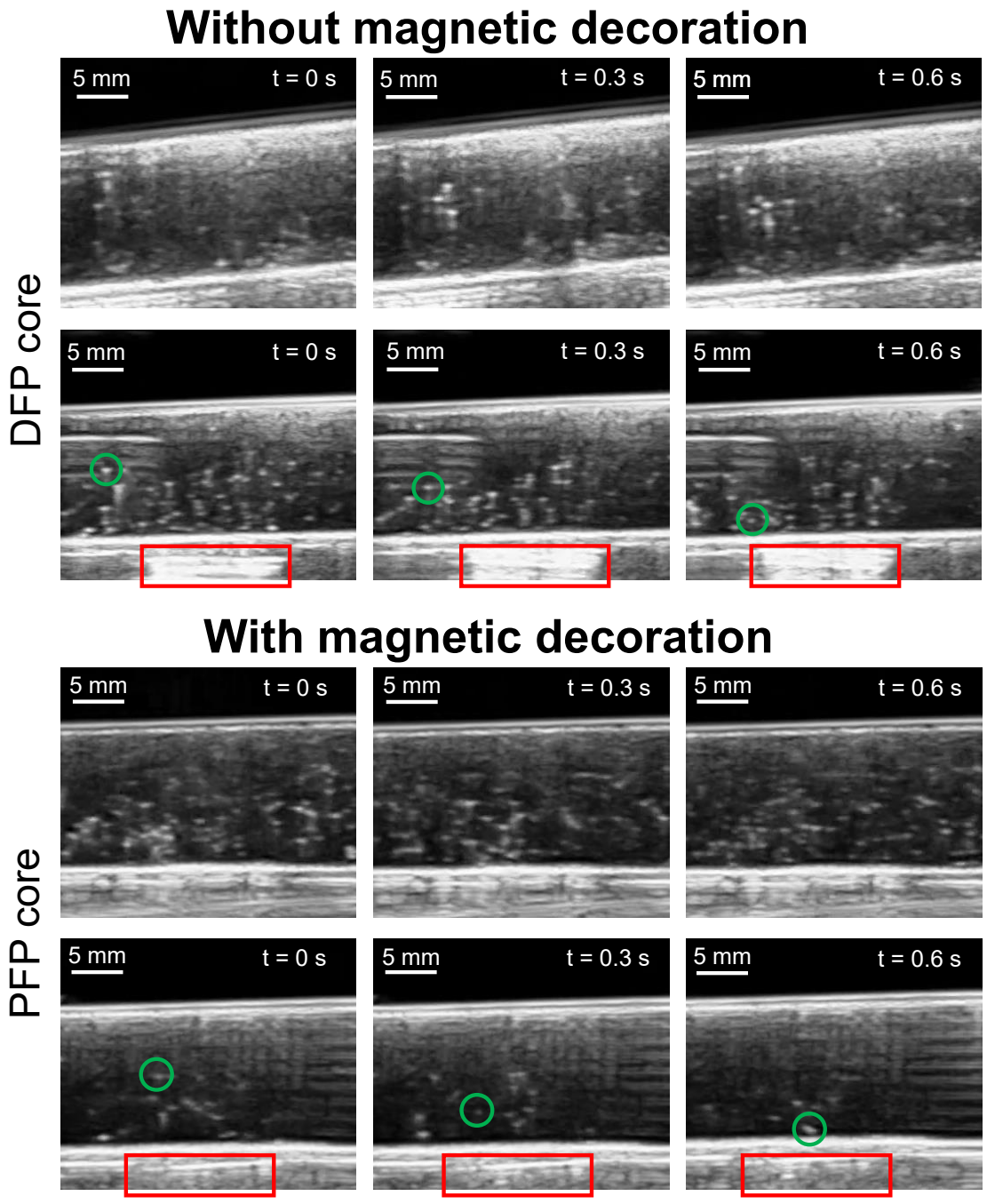



**Figure 5.8.** Frames showing the motion of DFP- or PFP-based MOLNDs with dextran coating are presented in three subsequent frames following the exposure to a US field. In both cores, the upper sequence illustrates the behavior of droplet samples in the absence of a magnetic field gradient, while the lower sequence shows their behavior in the presence of a magnetic field gradient generated by a permanent magnet, indicated by the red box. Green circles are employed to emphasize the trajectory of a single droplet over time.

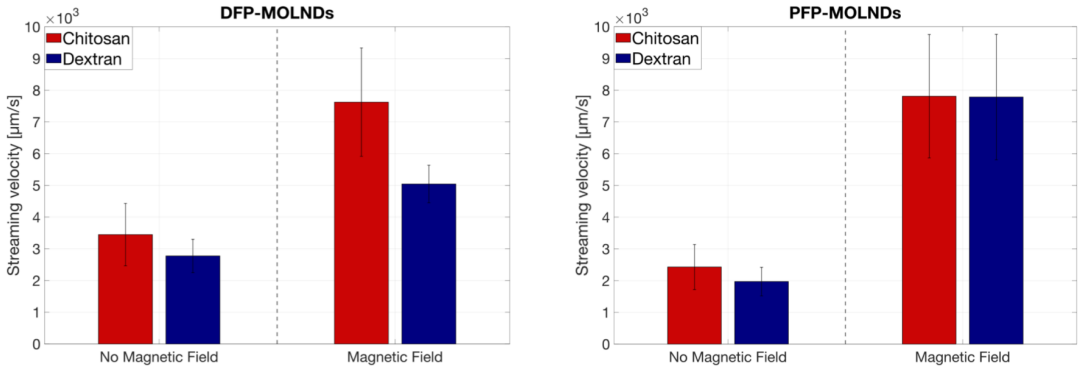



**Figure 5.9.** Average streaming velocities of DFP- and PFP-based MOLNDs in the absence or presence of a magnetic field gradient.

From the post-processing analysis of these frames, streaming velocities of the droplets are extrapolated and reported in Figure 5.9. The influence of the magnetic field leads to a significant increase in streaming velocity, at least twice, confirming the previous preliminary evidence and, thus, the successful magnetic decoration for all the samples. Furthermore, these results also point out a difference due to the coating type. In particular, the chitosan-coated MOLNDs are characterized by a higher streaming velocity than the dextran-coated ones, which could be associated with a higher MNP loading. This confirms the presence of electrostatic attraction forces between chitosan coating and $Fe_3O_4$ NPs, in accordance with the $\zeta$ potential values reported in Table 5.4.

The second experiment to assess the magnetic decoration involves the use of a microfluidic setup with a constant flow rate of the MOLND sample inside the microchannel and the observation of the MOLND trajectories in five different conditions, as illustrated in Figure 5.1B. The flow rate, denoted as $Q$, is considered equal to 9.8 $\mu$L/min, representing the average value between the measured inlet and outlet flow rates. In Figure 5.10, an example of two subsequent frames acquired with the above-described setup is shown. The green circles indicate the motion of a single nanodroplet, demonstrating that its trajectory is deflected by an $\alpha$ angle from the uniform flow (indicated by the dashed arrow).

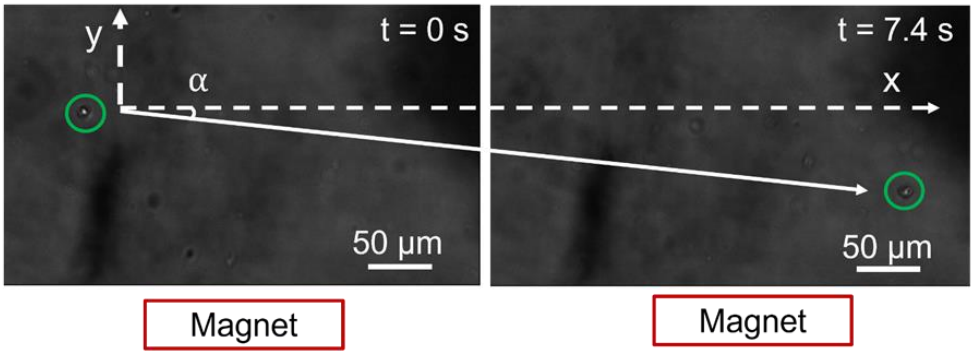



**Figure 5.10.** Frames at two subsequent time instants displaying the trajectory of a DFP-MOLND with chitosan coating (green circle) under the influence of a magnet placed next to the microchannel flow.

The deflection angle and the streaming velocity of DFP-MOLNDs for all magnetic field gradient conditions are extrapolated from the acquired images and are shown, respectively, in Figure 5.11 and Figure 5.12. The placement of the magnet laterally to the MOLNDs flow (positions 3 and 4) results in a deflection angle of approximately 15° from the original trajectory, accompanied by a slight decrease in the average values of the streaming velocity. Conversely, the variations in the deflection angle are not significant in the absence of the magnet or when the magnet is positioned along the flow directions (positions 1 and 2). When the magnet is positioned after the observation point (position 1), the attraction results in a substantial increase in the streaming velocity, which is approximately 25% for chitosan-coated MOLNDs and 8% for dextran-coated ones. On the contrary, for position 2, the streaming velocity is reduced by about 22% for chitosan-coated MOLNDs and 5% for dextran-coated ones. The stronger velocity variations observed for the chitosan-coated samples further confirm their greater MNP loading. As can be appreciated, the standard deviations of measured deflection angles and streaming velocities are significantly wide. This is a consequence of different aspects: the quite broad distribution of the MOLNDs size (as shown from DLS measurements reported in Figure 5.6); the variations in the magnetic moment of the MOLNDs due to different levels of MNP loading; the variable position of MOLNDs when injected within the microchannel; the strong spatial variation in the magnetic field that rapidly decays with the distance from the magnet. In particular, as depicted in Figure B.5 in the Appendix 6.3, the magnetic field amplitude decreases from 25 kA/m to around 10 kA/m along the 1.5 mm width channel, corresponding to a magnetic field gradient of $10 \times 10^3$ kA/m$^2$.

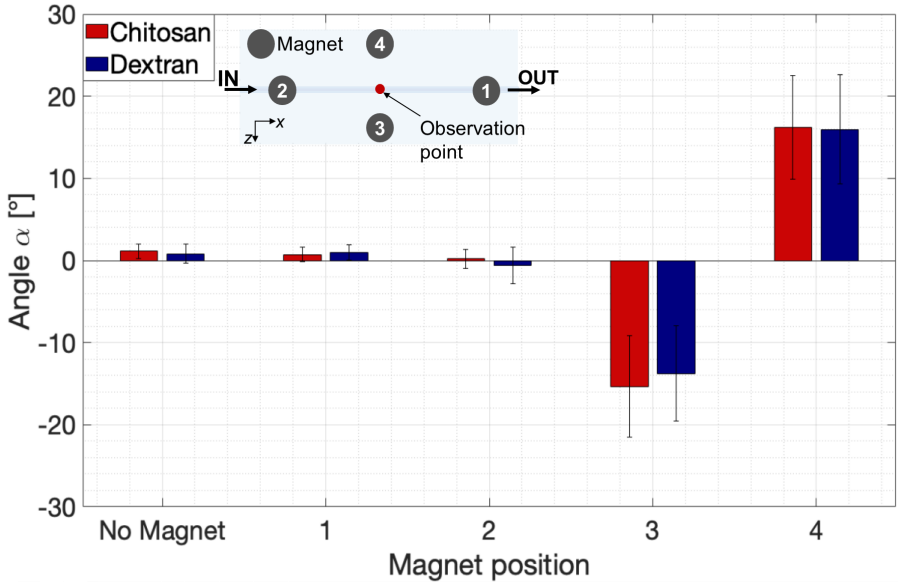



**Figure 5.11.** Mean deflection angle values obtained for DFP-core MOLNDs for all magnetic field gradient conditions.

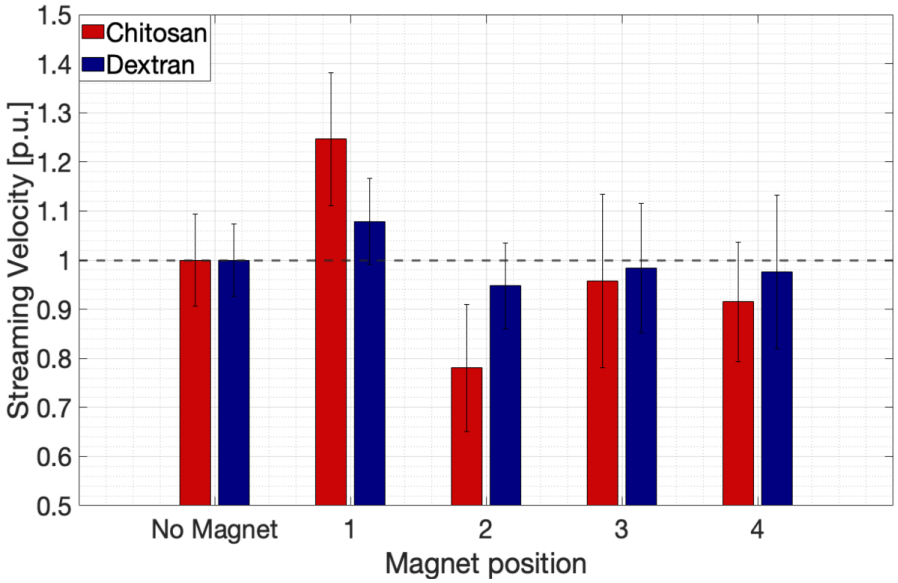



**Figure 5.12.** Mean values of streaming velocity obtained for DFP-core MOLNDs for all magnetic field gradient conditions. The values are normalized with respect to the "No Magnet" case.

### 5.2.3 Oxygen release through magnetic droplet vaporization

An essential characterization of MOLND samples involves assessing the oxygen release resulting from the magnetic droplet vaporization mechanism. To achieve this, the samples undergo exposure to an AC magnetic field until specific temperatures are reached, determined by the boiling point of the fluorocarbon core. The oxygen levels in the suspensions are then measured using an oxymeter probe, as detailed in Section 5.1.4.
The oxygen level of the suspension is assessed for 5 minutes both before and after the vaporization process, enabling the observation of oxygen variations relative to the initial concentrations. The corresponding oxygen concentration variations for each specific temperature are reported in Figure 5.13. The different temperatures at which oxygen is released are associated with the core property: for DFP-based MOLNDs, the oxygen concentration does not increase until 45 °C, while for PFP-based ones, it rises significantly starting from 27 °C. This behavior can be attributed to the different boiling points of the two fluorocarbons (51 °C for DFP, and 29 °C for PFP), even if the temperatures at which oxygen concentration starts to rise are slightly lower than the two boiling points. The reason is that the temperatures in the solution are recorded with a fiber optic probe, which provides a local measure of the temperature in the solution where the sensing point is placed [192], while on the decorated nanodroplet surfaces (i.e. near to the $Fe_3O_4$ NPs), it results in a higher temperature [193] and thus closer to the actual fluorocarbon boiling point. In terms of coating, chitosan-coated MOLNDs exhibit significant oxygen release at intermediate temperatures compared to dextran-coated ones. This behavior confirms the higher level of MNP loading shown by the chitosan-coated MOLNDs, as already supported by DLS measurements (see Figure 5.6).

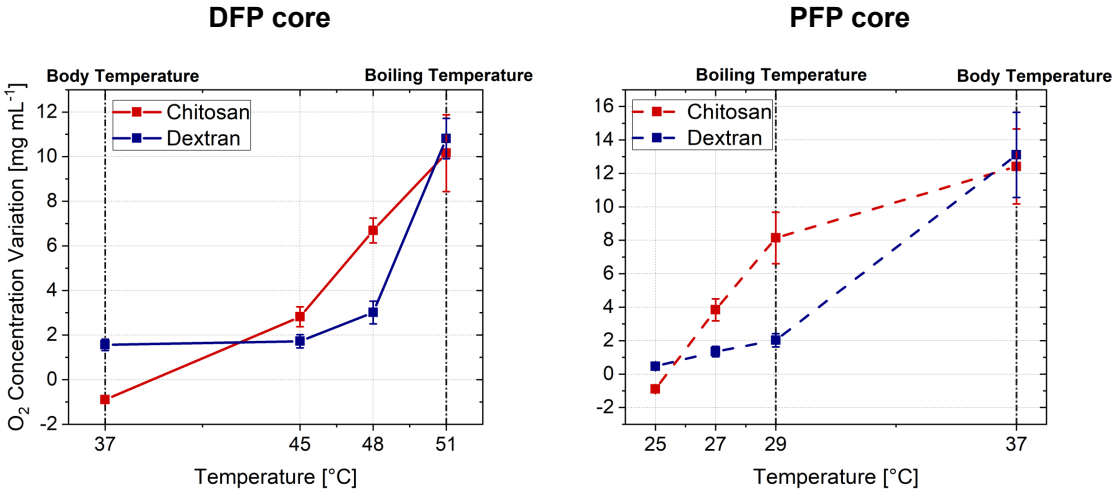



**Figure 5.13.** Variation in oxygen concentration observed for each MOLND sample at selected temperatures following AC magnetic field excitation. The uniform magnetic field applied has a peak amplitude of 72 kA/m and a frequency of 100 kHz.

To investigate the role of magnetic droplet vaporization role in oxygen release, MOLND samples are observed with an optical microscope following exposure to an AC magnetic field, reaching the target temperatures. Examples of heating curves for chitosan-coated MOLNDs with different fluorocarbon cores are shown in Figure 5.14. Figure 5.15 reports relevant images of the treated samples, clearly showing that, due to their increased dimensions (in the order of 10–20 $\mu$m), the MOLNDs have undergone the process of vaporization. Additionally, aggregates of $Fe_3O_4$ NPs are visible on the surface of the vaporized MOLNDs, confirming the magnetic decoration responsible for the heating release under the AC magnetic field excitation.
In addition, from a qualitative analysis, it is possible to derive the relationship between the temperature achieved in the solution through AC magnetic field excitation and the activation of the vaporization process specific for each sample. In particular, vaporization for PFP-MOLNDs starts around 27 °C, with the appearance of a few bubbles visible in the suspension. Their amount progressively increases with temperature, peaking at 29 °C, and then decreases when overcoming the PFP boiling point. For this reason, only a few bubbles can be observed at 37 °C. A similar behavior is observed for DFP-MOLNDs, but the vaporization process occurs at higher temperature. In particular, the nanodroplets start to vaporize at 45 °C, reach a maximum quantity at 48 °C, and start to diminish at 51 °C. Therefore, the different behavior of the DFP- and PFP-MOLNDs is consistent with the boiling temperature of the two fluorocarbons and with the results obtained in oxygen release analysis.

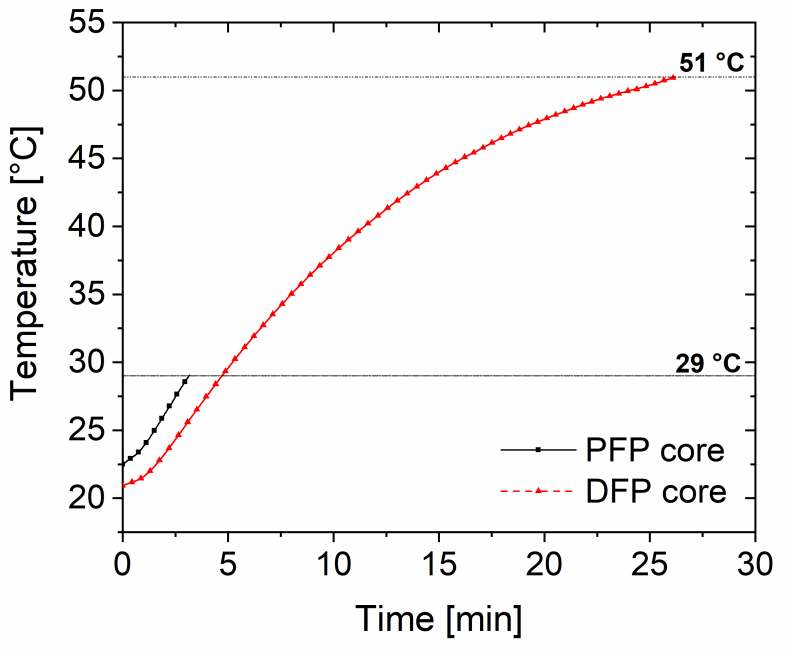



**Figure 5.14.** Heating curves of chitosan-coated MOLNDs with DFP- and PFP-core.

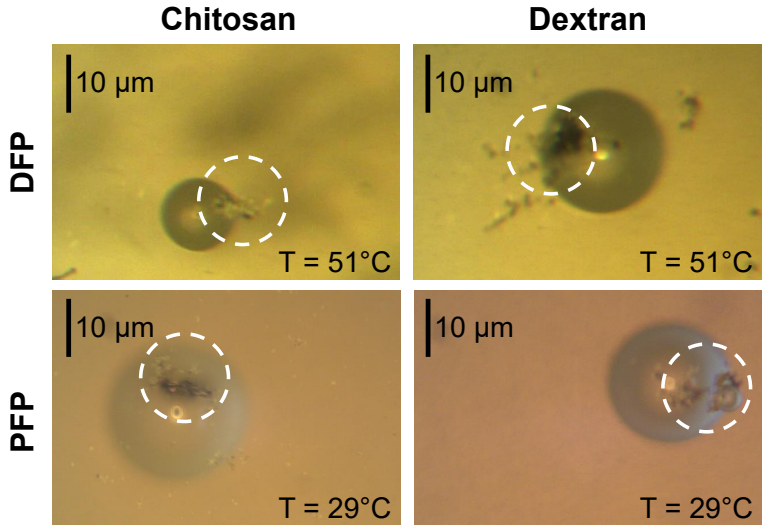



**Figure 5.15.** Optical microscope images of magnetically vaporized MOLNDs at the respective boiling points of both fluorocarbon cores.

### 5.2.4 *In vitro* cytotoxicity tests

After characterizing the physico-chemical properties and evaluating the oxygen-release ability, MOLNDs undergo *in vitro* cytotoxicity studies to assess the biocompatibility of these hybrid systems. The *in vitro* tests employ the resazurin assay on the A549 human lung cancer cell line, as detailed in Section 5.1.5. Cell viability is expressed in Relative Fluorescence Units (RFU %), and the results are normalized on the control sample, consisting of untreated cells considered as 100% viability. Cells are treated with four different dilutions of MOLND suspensions in the culture medium (1:20, 1:10, 1:8, and 1:5) for 72 hours. Figure 5.16 illustrates the cell viability results for all the samples after 24, 48, and 72 hours of treatment. For both the DFP- and PFP-cores, the cell viability is not reduced for the lowest MOLND concentration (1:20 and 1:10 dilutions). Notably, in the case of PFP-core MOLNDs with dextran coating, there is even an increase of nearly 20% in cell viability. However, for the 1:8 dilution we observed different behavior based on the composition of the core and coating of the MOLND samples. In particular, cell viability is not affected by the 72-h treatment with PFP-core nanodroplets coated with dextran, while a reduction of approximately 20% is noticed in the case of chitosan coating. On the contrary, for the DFP-core MOLNDs a decrease of about 40% in cell viability is observed for both coatings. Lastly, at the highest MOLND concentration (1:5 dilution), cell viability drastically decreases within the range of 60–90%. Although the limited number of samples analyzed, these reductions are statistically significant as demonstrated by one-way ANOVA with Tukey's post-hoc multiple comparison test.

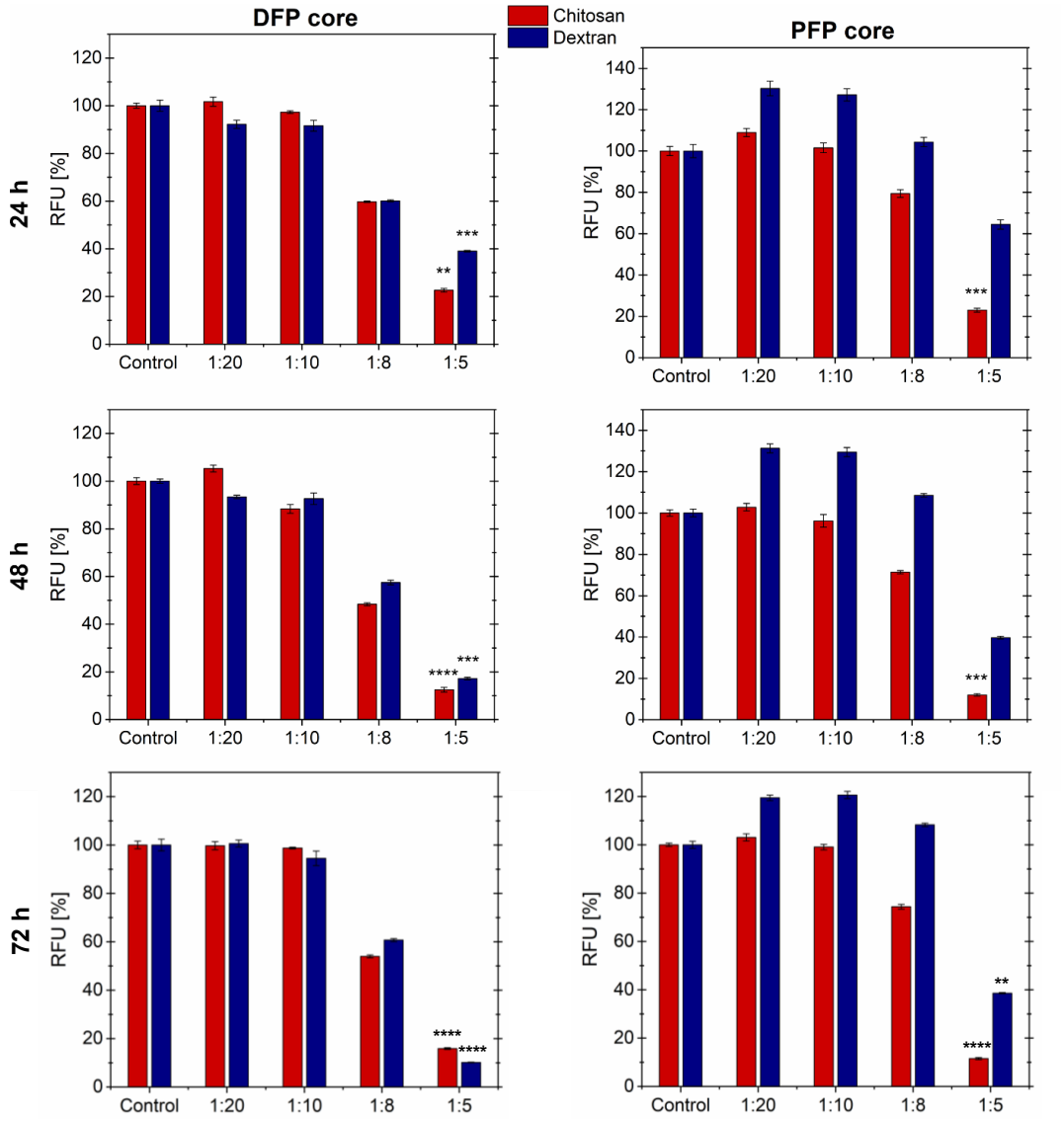



**Figure 5.16.** Cell viability assessment (% RFU) on A549 cell culture after 24-, 48- and 72-hour incubation with MOLNDs using resazurin assay. Control refers to cells without MOLND treatment, while other cell samples were treated with four different dilutions of MOLNDs (1:20, 1:10, 1:8, and 1:5) in the culture medium. The reported data are normalized with respect to the control, which is considered as 100%. RFU data are indicated as mean ± SD (for a number of biological replicates equal to 3). All the analyses with a $p < 0.05$ were indicated as statistically significant ($^{*}$ $p \leq 0.05$; $^{**}$ $p \leq 0.01$; $^{***}$ $p \leq 0.001$; $^{****}$ $p \leq 0.0001$).

## 5.3 Conclusions

In this Chapter, a refined method for synthesizing OLNDs and magnetically decorating them with $Fe_3O_4$ NPs has been presented, addressing a research gap in utilizing magnetic droplet vaporization for therapeutic oxygen release. Various types of MOLNDs were examined, with differences in their fluorocarbon-based cores (DFP or PFP) and surface coatings (dextran or chitosan). The efficacy of the magnetic decoration process was confirmed through SEM and TEM characterization, alongside studying the deviation of MOLND trajectory under a magnetic field gradient. Magnetic droplet vaporization was investigated by exposing MOLNDs to AC magnetic fields, facilitating heat release from $Fe_3O_4$ NPs through hysteresis losses.

Moreover, analysis of magnetic stimuli for oxygen release highlights magnetic droplet vaporization as a highly promising therapeutic approach. The study underscores the critical role of selecting the appropriate fluorocarbon core and polymeric coating to optimize the decoration process and enhance the oxygen release capability of MOLNDs. Specifically, investigations into different core and coating types revealed that DFP-core MOLNDs are more suitable for biomedical applications at body temperature compared to PFP-based ones due to their higher boiling point. Additionally, chitosan coating has demonstrated superior ability in providing controlled and efficient oxygen release, attributed to its more rigid structure compared to dextran.

Furthermore, *in vitro* cytotoxicity studies indicate that MOLNDs interact non-toxically with A549 cells, especially when applied at dilutions of $1:8$ or lower.

These findings offer promising prospects for the future utilization of MOLNDs in the biomedical field as drug-delivery nanocarriers responsive to dual stimuli (magnetic and US fields). Moreover, their hybrid composition holds potential for integrating additional theranostic functionalities such as US-based imaging and magnetic hyperthermia.

# Chapter 6

# Application of magnetic hyperthermia in radical polymerization processes

This Chapter introduces an innovative method exploiting the thermal energy released by MNPs under the influence of an AC magnetic field to induce radical polymerization of hydrogels. Radical polymerization is important in the field of materials science, offering a versatile way to engineer materials with precise properties and responsiveness. Specifically, the utilization of $CoFe_2O_4$ (cobalt ferrite) NPs, characterized in the Chapter 2, to polymerize polyacrylamide hydrogels represents a good alternative to conventional techniques to promote the radical polymerizations, i.e. thermal heating or light irradiation. Magnetic hyperthermia appears also as a versatile tool for controlling temperature within confined regions of the sample, a notable example is its application in selective volume polymerization within a thermo-sensitive environment. Furthermore, these findings set the stage for the production of non-magnetic materials, wherein $CoFe_2O_4$ NPs are initially concentrated in a small solution volume by a permanent magnet, subsequently facilitating the activation of polymerization across the entire material by an AC magnetic field.

The content of this Chapter has been published in:

[115] *M. Vassallo, M. Vicentini, M. Salzano De Luna, G. Barrera, P. Tiberto, A. Manzin, D. Martella. Magnetic hyperthermia to promote acrylamide radical polymerizations.* ACS Applied Polymer Materials, ***2024**, 6(8): 4696–4707.*

Part of the work was conducted at the Istituto Nazionale di Ricerca Metrologica (INRiM), in collaboration with the Department of Chemistry "Ugo Schiff" at the University of Florence and the Department of Chemical, Materials, and Industrial Production Engineering at the University of Naples Federico II.
Further investigations regarding rheological and mechanical characterizations of

polyacrylamide hydrogels, and heat transfer numerical modeling are reported in Appendix C.

## 6.1 Materials and Methods

### 6.1.1 Reagents

Acrylamyde, *N*,*N*'-methylen-bis-acrylamide, ammonium persulfate (APS), and ultra-low gelling temperature agarose were purchased from Sigma-Aldrich (St Louis, Missouri, USA).

### 6.1.2 Hydrogel preparation

The hydrogel monomer formulation was prepared by dissolving 200 mg of acrylamide, 10 mg of bis-acrylamide, and 10 mg of APS in deionized water, resulting in a final volume of 2 mL. In the case of the magnetic hydrogel, an aqueous suspension of $CoFe_2O_4$ NPs at a concentration of 14 mg/mL was substituted for deionized water.
The induction of hydrogel polymerization varied depending on the sample (detailed in Table 6.1). In one method, bulk heating was achieved by immersing the sample in a water bath set at 60 °C for 10 min. Alternatively, polymerization was triggered by exposing the sample to an AC magnetic field with a peak amplitude of 40 kA/m and a frequency of 100 kHz for 7 min, exploiting the heating capabilities of $CoFe_2O_4$ NPs. All polymerizations were conducted in glass cylindrical vials with an internal diameter of 12 mm or plastic cylindrical vials with an internal diameter of 17 mm.
The thermo-responsive hydrogel was prepared by dissolving 1% ($w/w$) of ultra-low gelling point agarose in water at 80 °C, followed by cooling to room temperature to induce gelation.

### 6.1.3 Hydrogel characterization

The gel fraction and swelling degree of the hydrogel were assessed using gravimetric methods. The gel fraction was calculated by dividing the weight of the dried gel post-immersion in water (to eliminate any unpolymerized components) by the weight of the dried gel before immersion in water, as shown in the subsequent equation:

$$\text{Gel fraction } (\%) = \frac{W_\text{f}}{W_\text{d}}\ 100 \tag{6.1}$$

where $W_\text{f}$ represents the weight of the hydrogel after being immersed in water for seven days and subsequently dried at 60 °C for 24 hours, while $W_\text{d}$ indicates the

weight of the hydrogel dried after polymerization at 60 °C for 24 hours.
Another crucial aspect of hydrogel characterization is the swelling degree, which reflects its capacity to absorb water. This parameter is determined by calculating the ratio of the weight acquired after rehydrating the gel to the weight of the dried gel, as illustrated in the subsequent equation:

$$\text{Swelling degree } (\%) = W_\text{s} - \frac{W_\text{d}}{W_\text{s}}\, 100 \tag{6.2}$$

where $W_\text{s}$ is the weight of the hydrogel in the swollen state, and $W_\text{d}$ is the weight of the hydrogel in the dried state.
Attenuated total reflectance (ATR) spectroscopy was conducted on both monomers and polymerized materials (after drying) using a Spectrum Two FT-IR Spectrometer (Perkin Elmer, Waltham, Massachusetts, USA).
Further investigations regarding rheological and mechanical properties of polyacrylamide hydrogels are detailed in Appendix C.

## 6.2 Results

### 6.2.1 Concept of radical polymerization *via* magnetic hyperthermia

Figure 6.1 illustrates the approach used for achieving radical polymerization via magnetic hyperthermia and a schematic of the experimental setup for temperature monitoring of MNPs-based heating. The formulation consists of acrylamide-based molecules as monomers and a thermal iniziator dissolved in a solvent. Additionally, a precise quantity of MNPs is incorporated into the mixture to regulate the heating when exposed to an AC magnetic field, thereby initiating the polymerization process.

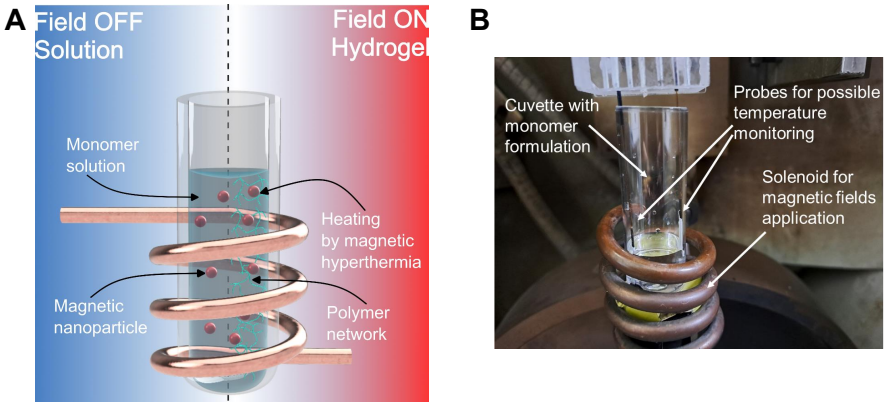



**Figure 6.1.** (**A**) Schematic of magnetic hyperthermia based heating to activate a radical polymerization. (**B**) Picture of the setup for radical polymerization by magnetic hyperthermia.

In particular, we opted for a model formulation consisting of an aqueous solution comprising acrylamide, *N*,*N*'-methylen-bis-acrylamide (referred to later as bis-acrylamide) as a cross-linker, and ammonium persulfate (APS) as a thermal initiator. This composition was chosen for its stability at room temperature over several hours, without any observed spontaneous polymerization. The material was selected due to its broad range of applications, spanning from biological studies (e.g., as a support for electrophoresis or cell scaffolding) [194, 195] to water purification processes. [196] The versatility of this formulation enables the attainment of various mechanical properties by adjusting the monomer concentration and allows the utilization of different polymerization conditions by modifying the APS concentration or incorporating additional co-initiators. [195]
The solution without MNPs undergoes various treatments to initiate polymerization, as depicted in Figure 6.2A. Alternatively, the formulation is either exposed to a heating bath (set at 60 °C) or exposed to an AC magnetic field with a frequency of 100 kHz. In each case, the achievement of successful polymerization is qualitatively assessed by a simple vial inversion test, as the radical reaction results in the formation of a solid, gel-like material.
Initially, the formulation undergoes exposure to various magnetic fields, culminating in the application of a 40 kA/m field for 30 min. However, in all cases, no polymerization has occurred, as the solution has remained in a liquid state throughout the tests. This outcome demonstrates that utilizing AC magnetic fields without suitable susceptors is ineffective for controlling radical polymerization, primarily due to the negligibility of eddy current effects. Conversely, when employing a conventional heating bath, a gel-like material is successfully obtained. The concentration of APS has been adjusted to achieve complete polymerization within a 10-min reaction period at 60 °C, and all hydrogels later referred to as prepared by bulk heating are synthesized under these conditions.

The same experiment is conducted with the inclusion of MNPs in the formulation, as reported in Figure 6.2B. In this scenario, magnetic hyperthermia proves to be effective in producing a hydrogel. Specifically, 14 mg/mL of $CoFe_2O_4$ NPs are added to achieve complete polymerization within 7 min under the application of a field with a peak amplitude of 40 kA/m, as evidenced by the vial inversion test. Figure 6.2C illustrates the temperature profile recorded throughout this polymerization process. Upon activation of the field, the temperature increases linearly until reaching 60 °C (after 5.8 min). Subsequently, a more rapid rise in temperature is observed, likely attributable to the heat release from the polymerization process [197], peaking at 75 °C. The magnetic field is deactivated after 7.2 min, when the solid hydrogel has already formed.

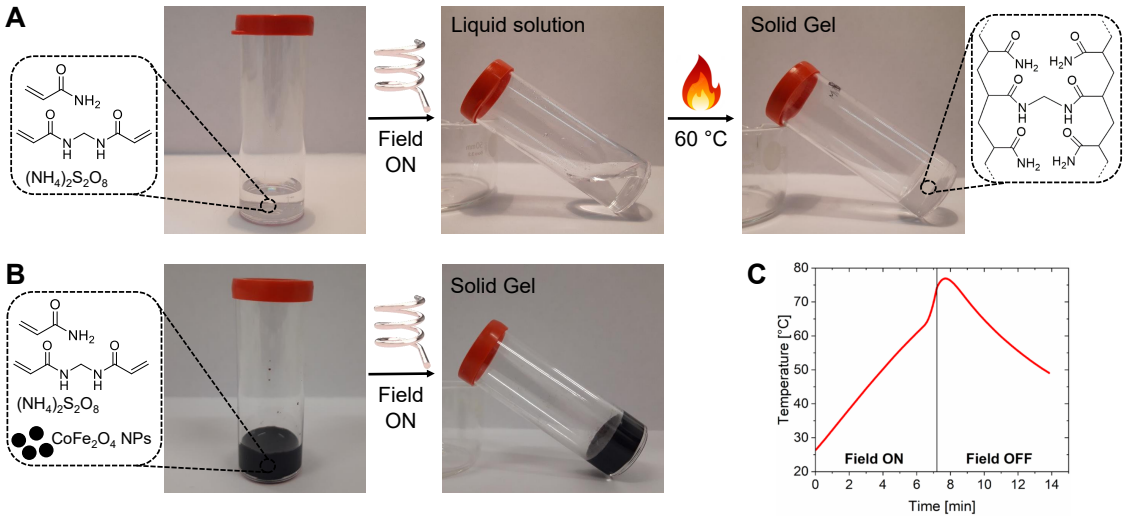



**Figure 6.2.** (**A**) Images of the initial hydrogel formulation, and the same after AC magnetic field application or immersion in a heating bath at 60 °C. In the first case, the image depicts a liquid state of the material during the vial inversion test, indicating no polymerization. Conversely, a solid hydrogel was observed to form through conventional heating. (**B**) Pictures of the initial hydrogel formulation doped with $CoFe_2O_4$ NPs and the same after AC magnetic field application. In this case, the picture demonstrates a solid material during the vial inversion test. (**C**) Temperature time evolution during the AC magnetic field exposure in a formulation containing the $CoFe_2O_4$ NPs. The temperature behaviour after the magnetic field switching off is also reported.

### 6.2.2 Characterization of magnetic hydrogel

To confirm the success of the polymerization, in addition to the vial inversion test, an analysis has been conducted using FTIR spectroscopy in combination with Attenuated Total Reflectance (ATR) sampling methodology (ATR-FTIR), as shown

in Figure 6.3. In this analysis, the absence of characteristic bands associated with the acrylamide group, such as the C=C bending at 816 $cm^{-1}$, in the resulting material compared to the monomers, is evidence of complete polymerization.

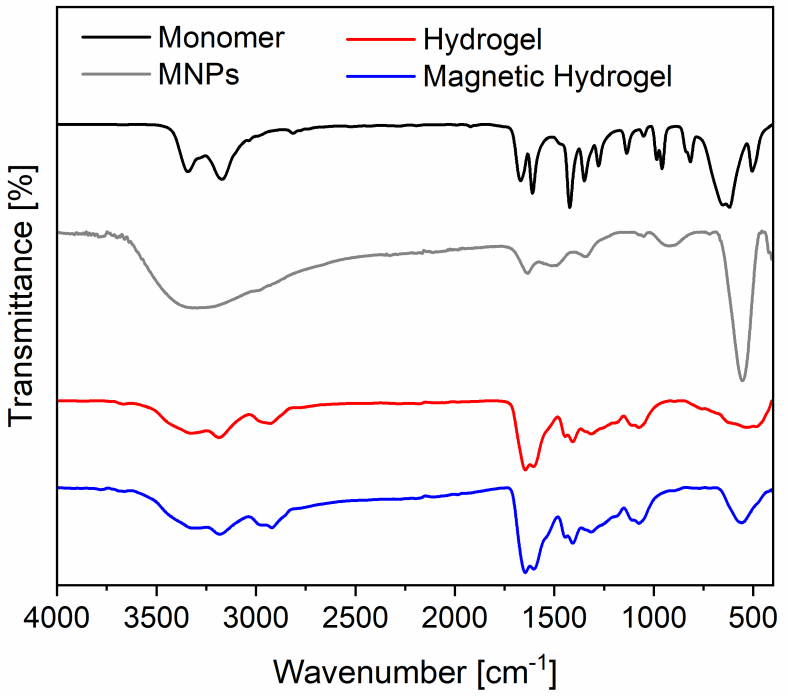



**Figure 6.3.** The ATR spectrum of the acrylamide monomer exhibits the characteristic peak at 816 $cm^{-1}$ corresponding to the C=C bending. For MNPs, the band at 530 – 580 $cm^{-1}$ (554 $cm^{-1}$) can be attributed to the stretching vibration of Fe-O and Co-O bonds. In both the hydrogels, the disappearance of the peak at 816 $cm^{-1}$ demonstrates complete polymerization.

In order to evaluate the impact of MNP presence and polymerization conditions on the properties of the hydrogel, a comprehensive characterization has been conducted. This involves gravimetric analysis on three types of hydrogels: two incorporating $CoFe_2O_4$ NPs, prepared through either magnetic hyperthermia or traditional bulk heating methods, and one without MNPs (prepared via bulk heating). Additionally, the magnetic properties of the two magnetic hydrogels have been assessed using VSM.
Beginning with the gravimetric analysis, the findings regarding gel fraction and swelling degree are summarized in Table 6.1. The gel fraction indicates the percentage of the monomer mixture that successfully undergoes polymerization, while the swelling degree estimates the maximum water absorption capacity of the resulting materials. In all samples, a gel fraction exceeding 96% is measured, indicating nearly complete polymerization and no inhibition of the radical process by the

presence of MNPs. Examining the hydrogels prepared via bulk heating, the introduction of MNPs results in a slight reduction in gel fraction (from 98% to 96%), accompanied by a minor increase in swelling degree. Conversely, when comparing the magnetic hydrogels, although the gel fraction remains consistent, the swelling degree is reduced by approximately 5% in the sample prepared through magnetic hyperthermia. These findings suggest that distinct hydrogel structures are formed during the different polymerization processes, resulting in slightly different mechanical properties, as reported in Appendix C.

**Table 6.1.** Parameters obtained by gravimetric characterization of the hydrogels.

| **Hydrogel** | **MNPs** | **Type of polymerization** | **Gel fraction** (%) | **Swelling degree** (%) |
|---|---|---|---|---|
| 1 | ✓ | Magnetic hyperthermia | 96.1 | 84.4 |
| 2 | ✓ | Bulk heating | 96.3 | 89.6 |
| 3 | ✗ | Bulk heating | 98 | 86.3 |

When comparing the magnetic properties of the hydrogels containing $CoFe_2O_4$ NPs, they exhibit nearly identical characteristics despite undergoing different initiation processes for polymerization. This observation is confirmed by Figure 6.4, which depicts the $M(H)$ curves obtained with VSM at room temperature, showing a perfect overlap.

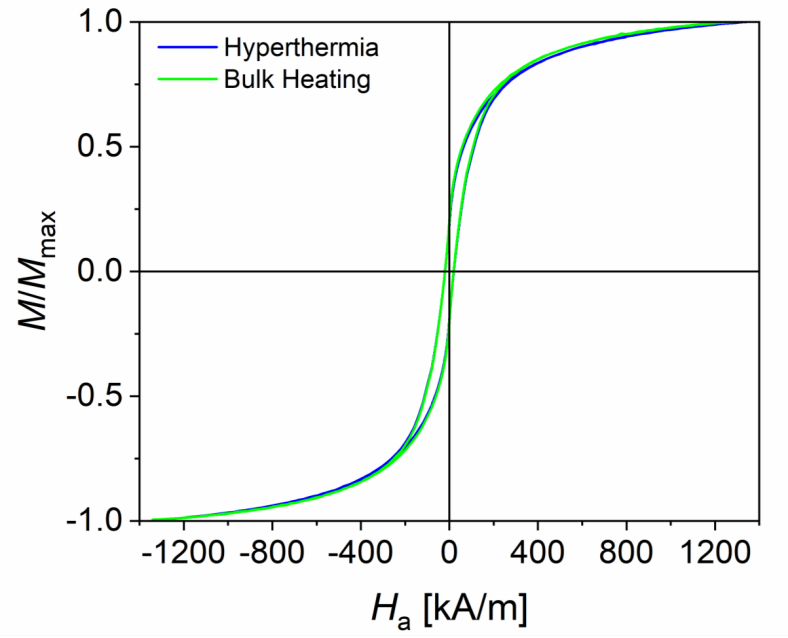



**Figure 6.4.** Comparison between static hysteresis loops at room temperature of magnetic hydrogels prepared by MNP based heating and classical bulk heating.

The characterization analysis reveals that magnetic hyperthermia-induced polymerization affects material properties, although not as significantly as modulating the formulation, such as varying concentration of monomer or initiator. [198] It's important to note that using magnetic hyperthermia requires a more complex hydrogel preparation protocol. However, by harnessing the properties of MNPs and employing magnetic fields to control polymerization, alternative possibilities to traditional methods could be introduced. For instance, achieving polymerization within thermosensitive environments or obtaining the polymerization of non-magnetic hydrogels, as demonstrated in the following paragraphs.

### 6.2.3 Polymerization in thermosensitive environments *via* magnetic hyperthermia

In certain contexts, it might be useful to achieve polymerization in thermosensitive environments, which cannot exceed a certain temperature threshold, or in opaque environments where photopolymerization cannot be employed. To accomplish this, the potential to concentrate heat primarily within a defined volume containing a specific quantity of MNPs is utilized. In this demonstration of concept, an ultra-low gelling point agarose hydrogel is employed as a thermosensitive medium. This substance is a physical hydrogel formed by homogenizing a 1% ($w/w$) solution of agarose through heating, solidifying into a gel at room temperature. The chosen

agarose allows the hydrogel to melt around 50 °C, making it impossible to combine this material with the bulk thermal heating polymerization method.
Figure 6.5 depicts the sequential stages involved in achieving selective volume polymerization through magnetic hyperthermia. Initially, a vial is filled with a heated agarose solution and allowed to solidify around a conical mold at room temperature. Upon removal of the mold, an agarose hydrogel shell with an empty conical space is obtained (Figure 6.5A), which can be filled by the magnetic acrylamide formulation (Figure 6.5B).
Subsequently, different heating treatments are applied to the sample. In the first case, employing a thermal bath set at 60 °C causes the agarose shell to melt, facilitating the blending of both hydrogel formulations before acrylamide polymerization. As the system cools to room temperature, only the formation of a hydrogel with MNPs either deposited at the bottom of the vial or dispersed throughout the hydrogel is observed (see Figure 6.5). This experiment confirms the inability of the bulk thermal heating to achieve spatial selectivity for polymerization.
Alternatively, various magnetic hyperthermia treatments are experimented until achieving only the polymerization of the acrylamide mixture. Figure 6.5D shows two examples of successful polymerization of the magnetic formulation without causing the agarose shell to melt. Consequently, the hydrogel retained the shape assumed by the monomer mixture before the application of the AC magnetic field, and the two materials result unmixed by the conclusion of the process.

It's worth mentioning that the presence of the agarose shell significantly alters the heat dissipation of the system compared to the hydrogels obtained through the bulk thermal heating, as illustrated in Figure 6.2. In this case, achieving polymerization requires an increase in peak amplitude and exposure time to the AC magnetic field (56 kA/m for 20 min). Figure 6.6 shows the temperature profile recorded at the center of the acrylamide solution during the magnetic field application. This measurement highlights the impact of the environment on the effectiveness of MNP heating, as evidenced by reaching a maximum temperature of 65 °C only after 20 min of field application.

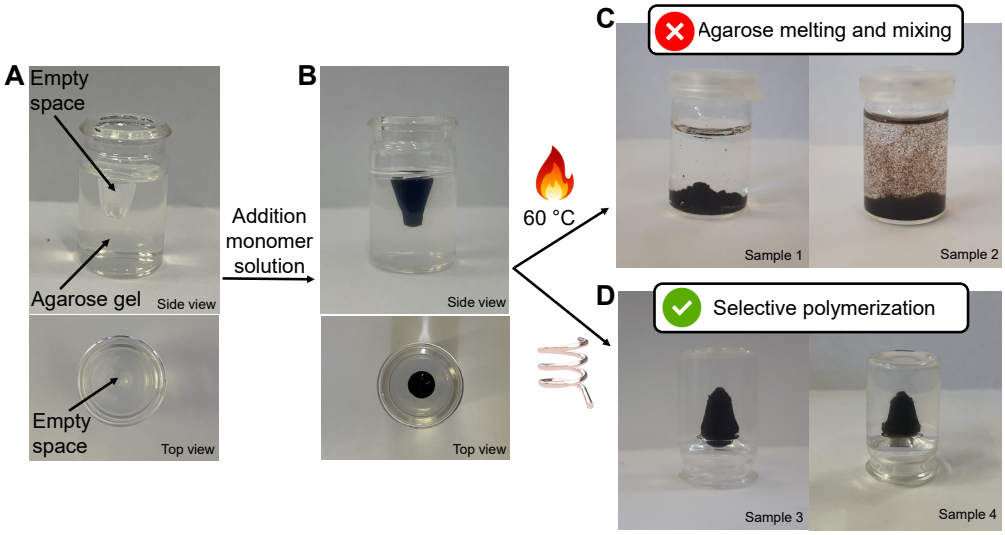



**Figure 6.5.** Possible application to induce polymerization in thermo-sensitive environments. An ultra-low gelling temperature agarose hydrogel shell (**A**) was filled with the acrylamide formulation (**B**). The samples were subjected to: (**C**) heating in a thermal bath (obtaining agarose melting and mixing of the materials); (**D**) magnetic hyperthermia (to achieve selective acrylamide polymerization). The vial inversion showed the formation of a solid hydrogel.

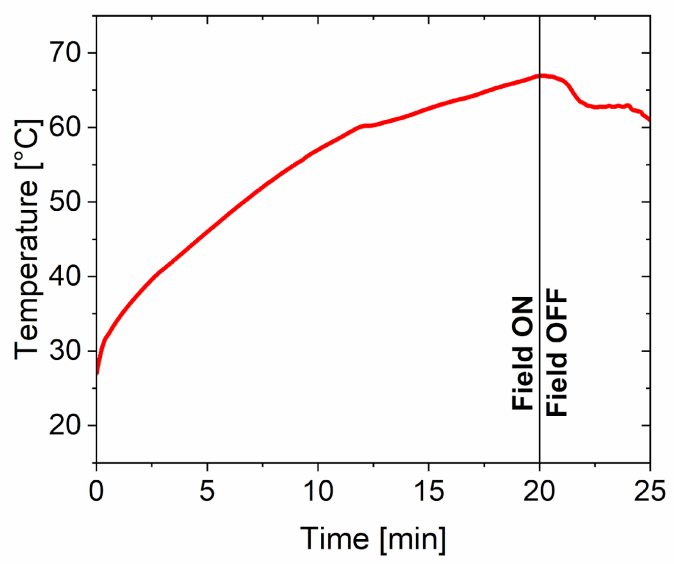



**Figure 6.6.** Time evolution of the temperature inside the acrylamide formulation during magnetic hyperthermia application. In this case, the formulation was placed inside an agarose shell during AC magnetic field application with a peak amplitude of 56 kA/m and a frequency of 100 kHz.

### 6.2.4 Preparation of non-magnetic hydrogel *via* magnetic hyperthermia

For some applications, the presence of $CoFe_2O_4$ NPs in the polymer material may not be desired. Therefore, they could be removed through selective dissolution, for instance, by using strong acids (an illustrative proof-of-concept is provided in Figure 6.7).

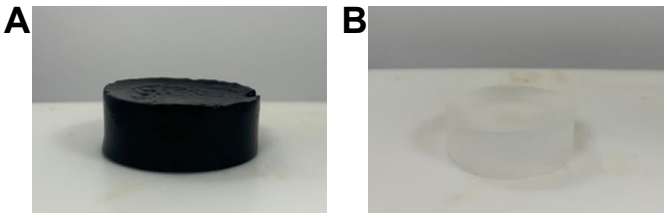



**Figure 6.7.** Picture of the hydrogel before (**A**) and after (**B**) dissolution of $CoFe_2O_4$ NPs by soaking the hydrogel in HCl (1M) for 3 days.

However, this study also considers more innovative strategies for producing materials that do not incorporate MNPs via magnetic hyperthermia. The proposed method is depicted in Figure 6.8A: localized heating generated by MNPs concentrated within a small volume of the monomeric formulation is used to polymerize the entire volume. This experiment complements the conditions illustrated in Figure 6.5, where spatially selective heating is demonstrated by manipulating the concentration of MNPs and the field parameters.
In this particular scenario (depicted in Figure 6.8A), the monomer formulation is initially infused with a small quantity of $CoFe_2O_4$ NPs (1.4 mg). However, under the previously mentioned field application conditions, polymerization does not occur due to the low concentration of MNPs. Subsequently, the MNPs are gathered (using a permanent magnet) to one side of the formulation, and the AC magnetic field is activated. Following a 20-min exposure to a 56 kA/m field, complete polymerization of the liquid volume is observed. It's worth noting that the heat generated by the MNPs positioned on one side of the vial is sufficient to polymerize various material volumes. In these experiments, 1.4 mg of $CoFe_2O_4$ NPs successfully polymerizes 2 to 6 mL of acrylamide solution within 20 min. Therefore, while employing a larger quantity of dispersed particles (as shown in Figure 6.2) reduces the required field amplitude and exposure time for polymerization, the latest experiments reveal the possibility of attaining non-magnetic materials through the indirect heating of MNPs positioned exclusively at a specific point in the sample.

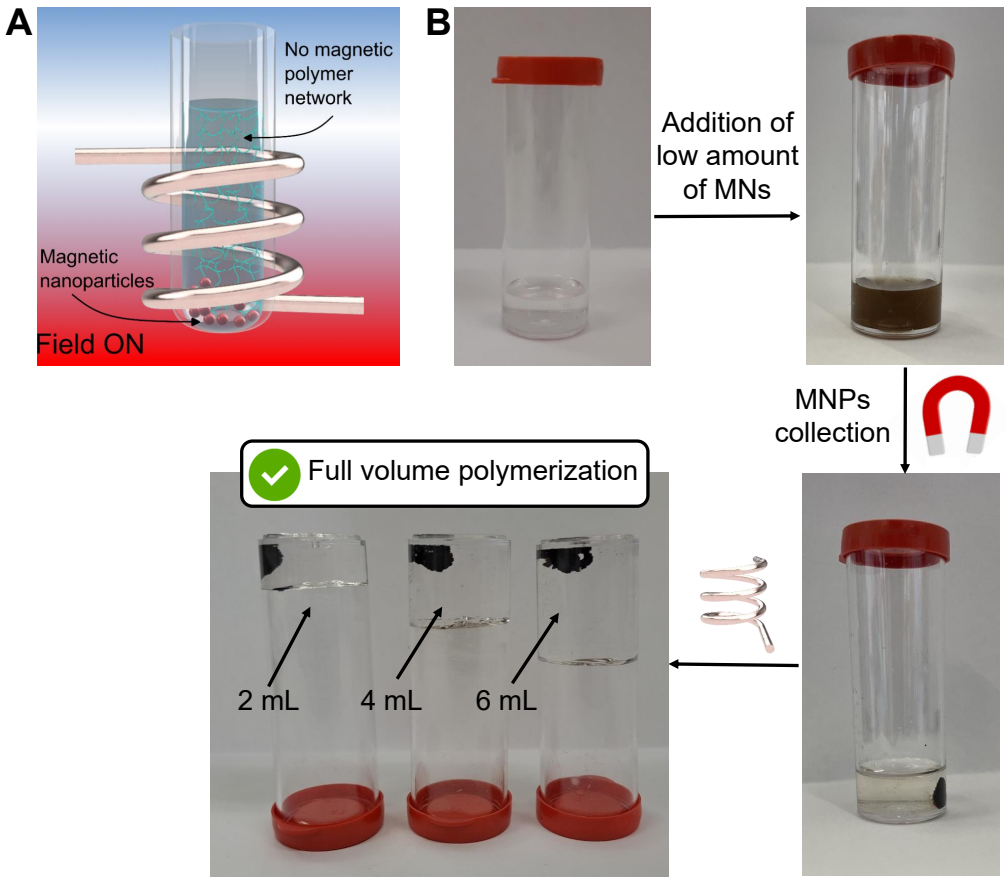



**Figure 6.8.** Possible application to prepare non-magnetic hydrogels. (**A**) Scheme of polymerization due to magnetic hyperthermia by MNPs concentrated on the bottom of the vial. (**B**) Sequence of pictures showing the protocol followed to obtain non-magnetic hydrogels polymerized by the action of the MNPs concentrated on one side.

Further insights have been investigated and detailed in Figure 6.9. Firstly, we confirm that MNPs are indispensable in all our experimental procedures to achieve acrylamide polymerization through exposure to the AC magnetic field. As depicted in Figure 6.9B, two vials containing 2 mL of the monomeric mixture undergoes identical field applications (56 kA/m for 20 min). Polymerization occurrs and results in the formation of solid material only when MNPs are present in the mixture. In the absence of MNPs, the formulation remains liquid, as indicated by vial inversion. Secondly, we have explored whether the heat generated around the MNPs would lead to selective polymerization of the volume around them during short field applications. Indeed, Figure 6.9B demonstrates how varying the duration of field application results in partial polymerization around the aggregates of MNPs, forming a solid hydrogel. This experiment does not allow for precise control over the partially polymerized volume and its shape, but it confirms that polymerization is initiated around the MNPs.

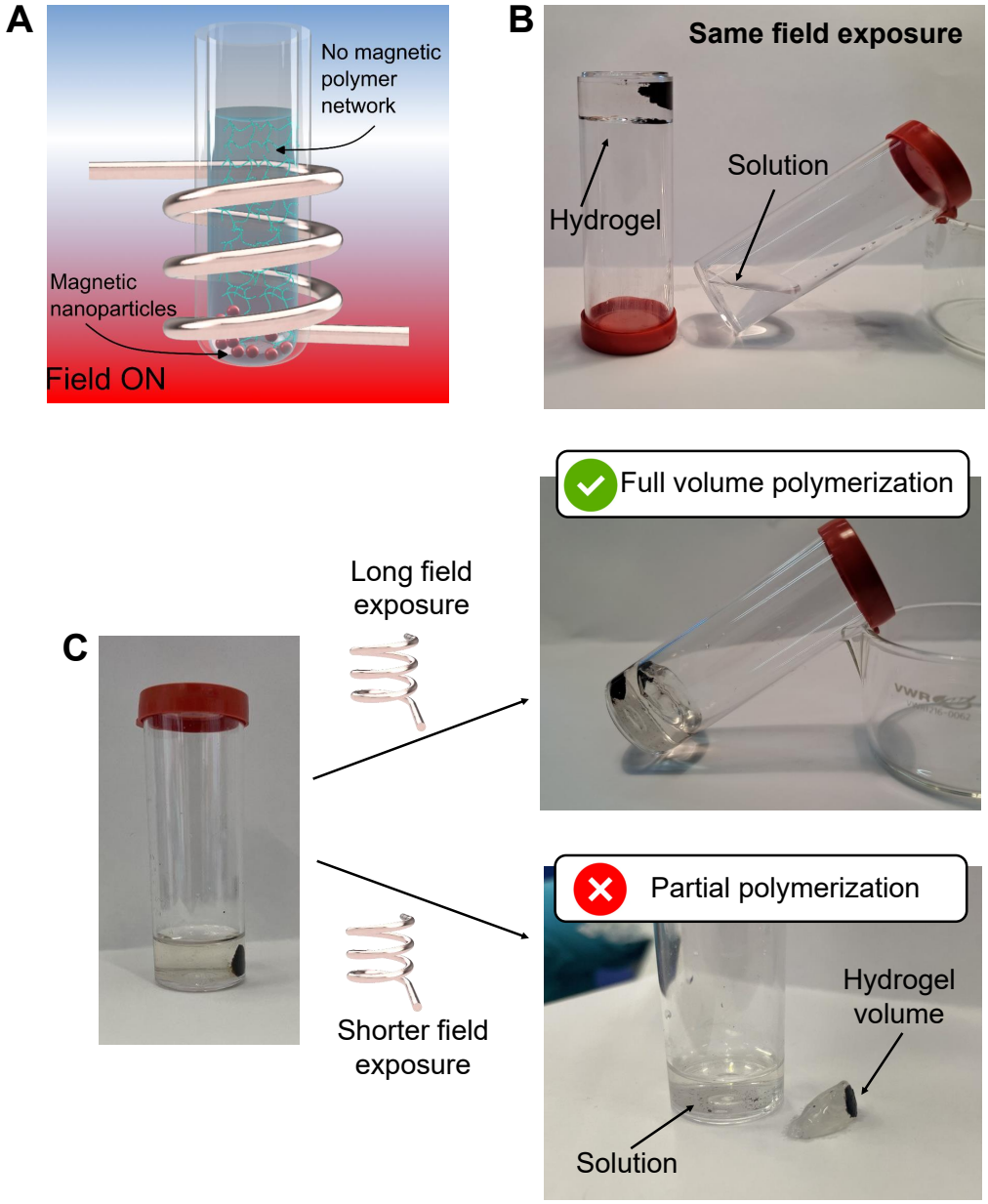



**Figure 6.9.** (**A**) Scheme of polymerization applied in the experiments in the other panels. The reaction has been carried out by magnetic hyperthermia when the MNPs are concentrated on the bottom of the vial; (**B**) Picture of two samples after exposure to the same field application (56 kA/m for 20 min). Only if MNPs were present in the formulation, a solid hydrogel was formed; (**C**) Picture of two samples after exposure to the AC magnetic field (56 kA/m) for different times. After 20 min of application, the whole solution was converted into a solid hydrogel. For a shorter time (10 min), only a partial polymerization was detected. The formed hydrogel was extracted from the solution to take the picture.

## 6.3 Conclusions

The incorporation of MNPs into an acrylamide formulation proves to be useful for initiating the radical polymerization reaction via magnetic hyperthermia under an AC magnetic field. This preparation method results in minimal variations in hydrogel properties compared to those prepared through bulk thermal heating polymerization, suggesting the importance of considering other parameters to modulate material characteristics, such as varying cross-linker amounts.
This polymerization approach demonstrates great versatility, with potential applications even in thermosensitive environments. Although demonstrated in a simple agarose hydrogel shell, with a melting temperature of 50 °C, this sets the stage for various applications, including more complex biological environments. To this end, comprehensive investigation of MNPs is essential to reduce the strenght of applied fields or the MNP content in the final materials.
Furthermore, the heat generated by MNPs can also be used to polymerize non-magnetic hydrogels if a small quantity of MNPs is concentrated in a confined volume and subjected to prolonged field exposure. The localized heat is then dispersed throughout the formulation, initiating the radical reaction. Even in this scenario, improvements in the SLP of MNPs and adjustments in monomer concentration (to increase heat release during polymerization) can aid in achieving polymerization.

# Future perspectives

From a materials science perspective, future efforts will aim to synthesize new MNPs with varied compositions and sizes to enhance heating properties for applications such as magnetic hyperthermia. This effort will involve the exploration of different elemental combinations and synthesis techniques to optimize the magnetic properties and heating efficiency of these nanomaterials. Additionally, investigating surface coating techniques, such as silica coating, that enable the functionalization of MNPs with molecules like fluorophores for imaging, or specific peptides to facilitate cellular targeting, will be of great interest. These coatings could provide stability, biocompatibility, and the ability to attach various functional groups that enhance the versatility of the MNPs in biomedical applications. Comprehensive characterization of these nanoparticles, as performed in Chapters 2 and 3, will be crucial for understanding their magnetic properties, surface chemistry, stability, and interactions with biological systems. Techniques such as TEM, DLS, and magnetic measurements will provide detailed insights into their structural and functional properties.

From a biological point of view, evaluating the cytotoxicity and effects of magnetic hyperthermia *in vitro* treatments, using protocols developed in Chapter 4, will be essential to assess their safety and efficacy. Furthermore, a study on cellular internalization using fluorescent tracers that bind to intracellular iron could provide quantification and localization of internalized MNPs within intracellular organelles. Additional research on different cell cultures, including both cancerous and healthy cells, will help elucidate cellular responses to magnetic hyperthermia. This comparative analysis will provide insights into the selectivity and efficiency of the treatment, potentially resulting in optimized protocols that enhance therapeutic effects on cancer cells while minimizing damage to healthy tissues.

Lastly, exploring further applications of MNPs, as discussed in Chapters 5 and 6, could lead to the development of novel multifunctional hybrid nanosystems. These systems could integrate magnetic properties with other functionalities, such as drug delivery or imaging capabilities, to create versatile tools for theranostics. For instance, magnetic field-mediated drug delivery systems could be engineered to deliver therapeutic agents precisely to target sites, reducing systemic side effects and improving treatment outcomes. Additionally, the production of tissue-mimicking

materials that incorporate MNPs could facilitate the creation of advanced models for simulating tissue behavior under magnetic hyperthermia conditions. In particular, these models would be useful for calibrating instruments and conducting *in vitro* tests.

# List of Publications

- M. Vicentini, M. Vassallo, R. Ferrero, A. Manzin. In silico experiments as a tool to reduce preclinical tests of magnetic hyperthermia. *Biomedical Science and Engineering*, **2021**, 2(1).

- M. Vicentini, M. Vassallo, R. Ferrero, I. Androulakis, A. Manzin. *In silico* evaluation of adverse eddy current effects in preclinical tests of magnetic hyperthermia. *Computer Methods and Programs in Biomedicine*, **2022**, 223, 106975.

- M. Vassallo, D. Martella, G. Barrera, F. Celegato, M. Coïsson, R. Ferrero, E. S. Olvetti, A. Troia, H. Sözeri, C. Parmeggiani, D. S. Wiersma, P. Tiberto, A. Manzin. Improvement of Hyperthermia Properties of Iron Oxide Nanoparticles by Surface Coating. *ACS Omega*, **2023**, 8(2): 2143-2154.

- S. Galati, M. Vassallo, A. Manzin, A. Troia. Magnetic Oxygen-Loaded Nanodroplets: Role of Perfluorocarbon Core and Polymeric Coating in Magnetic Droplet Vaporization for Oxygen Release. *Proceedings of the 8th World Congress on Recent Advances in Nanotechnology (RAN'23)*, **2023**.

- S. Galati, M. Vassallo, M. Vicentini, M. Vallino, F. Celegato, G. Barrera, D. Martella, E. S. Olivetti, A. Sacco, J. Petiti, C. Divieto, P. Tiberto, A. Manzin, A. Troia. Dual-responsive magnetic nanodroplets for controlled oxygen release via ultrasound and magnetic stimulation. *Nanoscale*, **2024**, 16(4), 1711-1723.

- M. Vassallo, M. Vicentini, M. Salzano De Luna, G. Barrera, P. Tiberto, A. Manzin, D. Martella. Magnetic Hyperthermia to Promote Acrylamide Radical Polymerizations. *ACS Applied Polymer Materials*, **2024**, 6(8), 4696-4707.

- G. Barrera, F. Celegato, M. Vassallo, D. Martella, M. Coïsson, E. S. Olivetti, L. Martino, H. Sözeri, A. Manzin, P. Tiberto. Microfluidic Detection of SPIONs and Co-ferrite Ferrofluid Using Amorphous Wire Magneto-Impedance Sensor. Accepted for publication on *Sensors*.

# Appendix A

# Influence of surface coating on the hyperthermia properties of $Fe_3O_4$ nanoparticles

In this Appendix, the results of simulations conducted with heat-transfer finite element solver on uncoated and coated $Fe_3O_4$ NPs, discussed in Chapter 3 are presented.

## A.1 Simulations with heat-transfer finite element solver

The thermometric characterization of MNPs were supported by thermal simulations carried out with an in-house 3D finite element code, which solves the heat transfer equation under the assumption of negligible convection phenomena. [55, 192] This result in:

$$\rho C_{\mathrm{p}} \frac{\partial T}{\partial t} = \nabla \cdot k \nabla T + Q_{\mathrm{ext}} + \frac{\mathrm{SLP} \cdot m_{\mathrm{NPs}}}{V_{\mathrm{water}}} \tag{A.1}$$

where $T$ is the temperature, $\rho$ is the mass density, $C_{\mathrm{p}}$ is the heat capacity, and $k$ is the thermal conductivity. SLP is the NP specific loss power estimated from the thermometric characterization, $m_{\mathrm{NPs}}$ is the mass of magnetic NPs within the particle-fluid suspension, where the NPs are assumed to be uniformly dispersed and $V_{\mathrm{water}}$ is the water volume. $Q_{\mathrm{ext}}$ is the heating power per unit volume due to the AC magnetic field source; this includes parasitic eddy current heating effects and is derived from preliminary thermometric measurements performed on a sample of water with volume $V_{\mathrm{water}}$.
Equation A.1 is completed by the following boundary condition:

$$k\nabla T \cdot \boldsymbol{n} = h(T_{\text{ext}} - T) \tag{A.2}$$

where $\boldsymbol{n}$ is the outward normal vector to the boundary surface, $h$ is the heat transfer coefficient, which considers convective cooling effects, and $T_{\text{ext}}$ is the time-dependent external temperature. At $t = 0$, $T = T_{\text{ext}}$ in all of the domains of analysis.

In Chapter 3, an analytical thermodynamic model [125], considering the multiple heat-exchange mechanisms occurring in the experimental setup, was used to fit the experimental curves and estimate the SLP of NPs. The obtained results (reported in Chapter 3 in Figure 3.10 and Figure 3.11) were corroborated by the simulations carried out with the heat-transfer finite element solver, allowing us to determine the spatial distribution of the temperature within the magnetic suspension during the heating–cooling transients. The numerical simulations were performed under nonadiabatic conditions on the system schematized in Figure A.1, considering the following material properties:

- polypropylene test tube: $\rho = 2600$ kg/m$^3$; $C_{\text{p}} = 820$ J/(kgK); $k = 3$ W/(mK);
- quartz holder: $\rho = 905$ kg/m$^3$; $C_{\text{p}} = 1900$ J/(kgK); $k = 0.185$ W/(mK);
- magnetic suspension: $\rho = 1020$ kg/m$^3$; $C_{\text{p}} = 4086$ J/(kgK); $k = 0.61$ W/(mK).

The coefficient of convective exchange $h$ between the holder surface and the surrounding air was set at 14 W/(m$^2$K). The heating power $Q_{\text{ext}}$ produced by the AC magnetic field sources was estimated to be 45 kW/m$^3$ from preliminary thermometric measurements on only water.
The fitting analytical curves and the numerical results are reported in Figure A.2A and A.2B, demonstrating a good reconstruction of the experimental data for both the uncoated and citrate-coated NP suspensions. In particular, the numerical curves were calculated in correspondence with the magnetic suspension center, where the sensing point of the fiber optic thermometer is expected to be placed. The uncertainty bars refer to the temperature variations within a volume around the suspension center, as depicted in Figure A.2C, which shows the temperature map at the end of the heating phase for the sample containing the uncoated NPs.

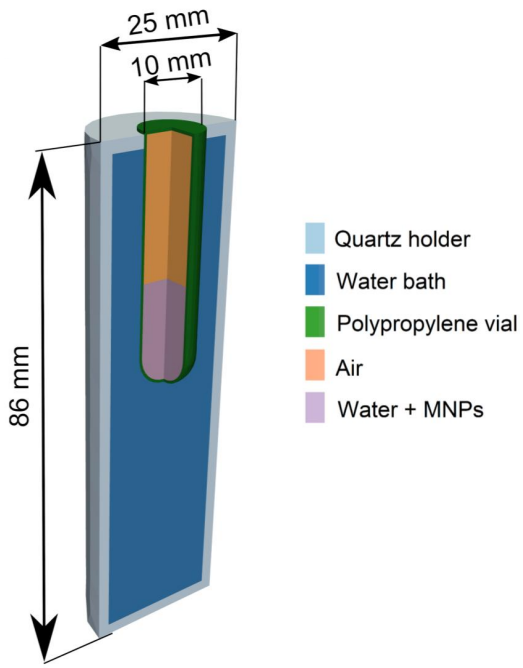



**Figure A.1.** Schematic of the sample container, corresponding to the domain considered for the heat-transfer numerical modeling.

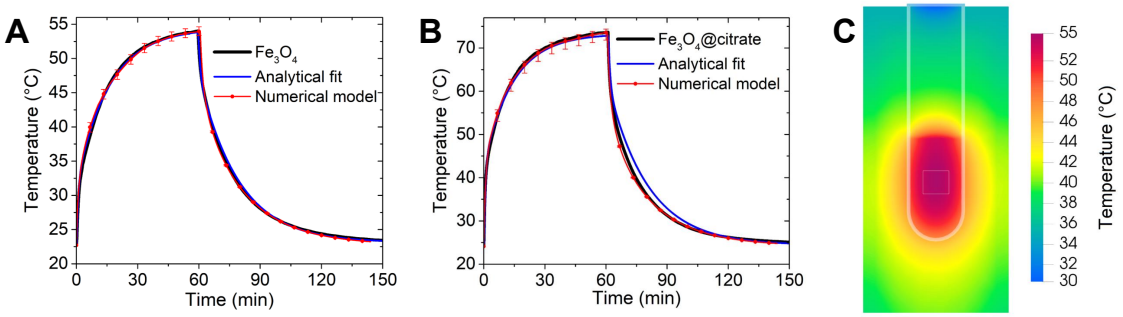



**Figure A.2.** Time evolutions of the temperature of the magnetic suspensions containing (**A**) the uncoated NPs and (**B**) the citrate-coated NPs, following the application for 60 min of an AC magnetic field with a peak amplitude of 48 kA/m) and a frequency of 100 kHz. The graphs contain the experimental data, the best fit outputs of the analytical thermodynamic model and the results obtained with the heat-transfer numerical model. (**C**) Spatial distribution of the temperature, calculated for the uncoated NP sample at the end of the heating interval.

# Appendix B

# Magnetic oxygen-loaded nanodroplets

In this Appendix, the results of additional investigations conducted on the samples of OLNDs and MOLNDs, discussed in Chapter 5, are presented. Specifically, the appendix covers acoustic responses of the samples, a numerical model illustrating the behavior of MOLNDs under magnetic field gradients, and an analysis of oxygen release following exposure of the samples to a US field.

## B.1 Acoustic response

To analyze the nanodroplet acoustic response, a custom-built setup was employed, as described in detail below. The US excitation was provided by a H-101 focused US transducer (Sonic Concepts, Bothell, Washington, USA) working at a fundamental frequency of 1.1 MHz and driven by a 800A3A amplifier (ar rf/microwave instrumentation, Bothell, Washington, USA), connected with a 33250A function generator (Agilent Technologies, Santa Clara, California, USA). Before performing the measurements on the OLNDs and MOLNDs samples, the peak rarefactional pressures were collected through a hydrophone coupled to an InfiniiVision 2000 X DSO-X 2022A oscilloscope (Keysight Technologies, Santa Rosa, California, USA) and stored on a Labview-provided computer, resulting in the range of 0.47–1.74 MPa. The solution was injected through a channel into a customized phantom able to mimic human soft tissue acoustic properties, by using a LLG-uniPERISTALTICPUMP flow controller (LLG-Labware, Meckenheim, Germany), and the acoustic activity was monitored by means of a focused passive cavitation detector (PCD) for the acquisition of the broadband acoustic signal in the range 0.5–5 MHz. From this analysis, Fast Fourier Transform (FFT) spectra were extracted to determine the acoustic response of the samples; each spectrum was obtained by averaging three acquisitions through Labview.

The acoustic response of OLNDs and MOLNDs was assessed by capturing the signal emitted during droplet excitation by US fields using a passive cavitation detector. The results obtained for nanodroplets with DFP-core are depicted in Figure B.1, while those for PFP-core are illustrated in Figure B.2. Three spectra were acquired at increasing acoustic pressures ranging from 0.47 MPa to 1.54 MPa for both OLNDs and MOLNDs. Notably, the outcomes from nanodroplets with DFP- or PFP-core exhibit similarities. The acoustic spectra reveal an elevation in harmonics bands as the ultrasonic pressure at 1.1 MHz increases, indicative of stable cavitation activity associated with forced bubble oscillations in the solution. Of particular interest is the observation that MOLND samples exhibit an increase in peak amplitude at the lowest acoustic pressures (0.47 MPa and 0.78 MPa), indicating a more robust emitted acoustic signal. This divergent behavior between OLNDs and MOLNDs can be attributed to the presence of $Fe_3O_4$ NPs in the solution, which enhances acoustic field scattering events, leading to a local increase in pressure and, consequently, heightened cavitation activity. However, this difference is less pronounced at the highest value of acoustic pressure considered here (1.54 MPa) due to the onset of inertial cavitation events for both samples.

To quantify inertial cavitation activity, the acoustic spectra were processed using cavitation noise spectrum analysis, assuming that the shock waves, generated during bubble collapse produce white noise in the spectrum. [199] The cavitation noise power (CNP) indicator obtained for nanodroplets with DFP- and PFP-core, respectively, is presented in Figure B.3 and Figure B.4. In this analysis, a large CNP value means a substantial acoustic signal generated by inertial cavitation. The results demonstrate that the increase in acoustic pressure causes the CNP to rise after reaching a specific threshold, which varies depending on the type of core and coating. The pressure range before the threshold allows the identification of optimal working conditions to prevent potential drawbacks from the inertial cavitation regime. Moreover, the type of coating used influences cavitation behavior, with chitosan coating providing a more rigid structure compared to dextran, resulting in the initiation of inertial cavitation at higher acoustic pressures for both OLNDs and MOLNDs. Additionally, magnetic decoration reduces the threshold for the inertial cavitation regime to lower pressures due to the enhancement of acoustic wave scattering events, as discussed earlier for stable cavitation. Concerning core type, PFP-core samples exhibit more intense signals from both stable and inertial cavitation analyses due to the lower boiling temperature of PFP compared to DFP, resulting in a higher percentage of cavitated nanodroplets.

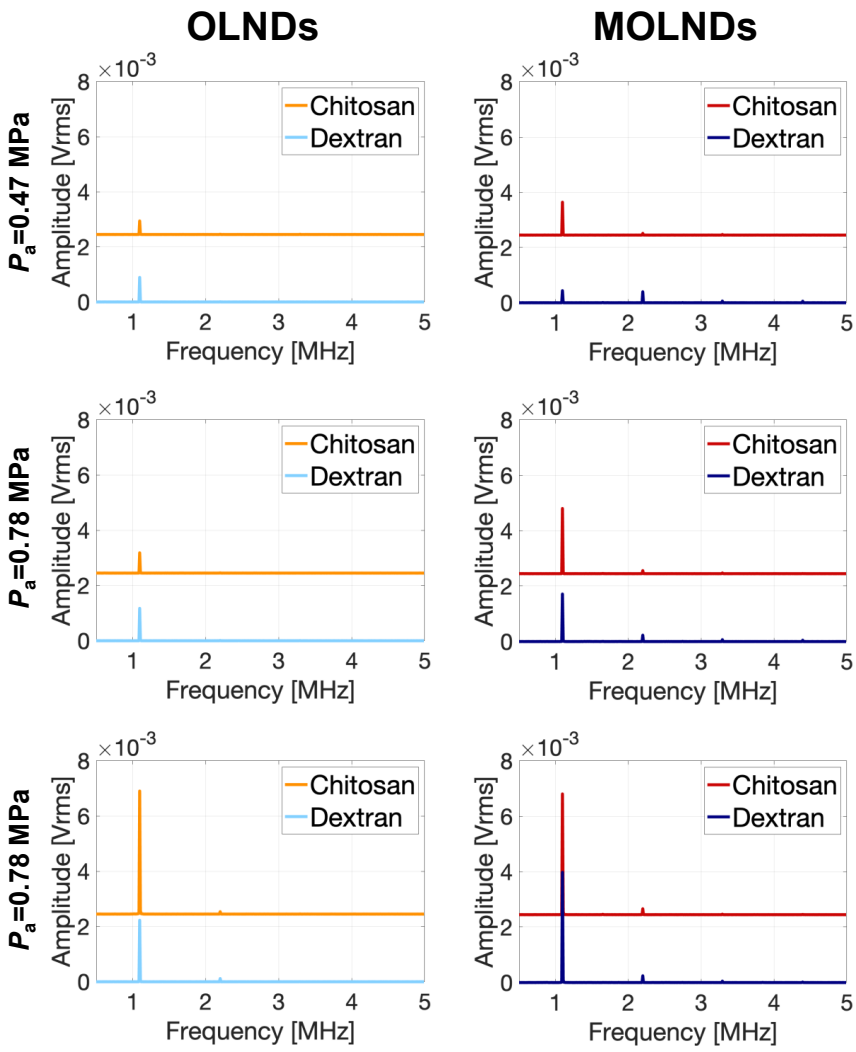



**Figure B.1.** Acoustic spectra of DFP-core OLNDs and MOLNDs with chitosan and dextran coating, measured at three acoustic pressures (0.47, 0.78 and 1.54 MPa). The reported results are based on the average of three acquired values.

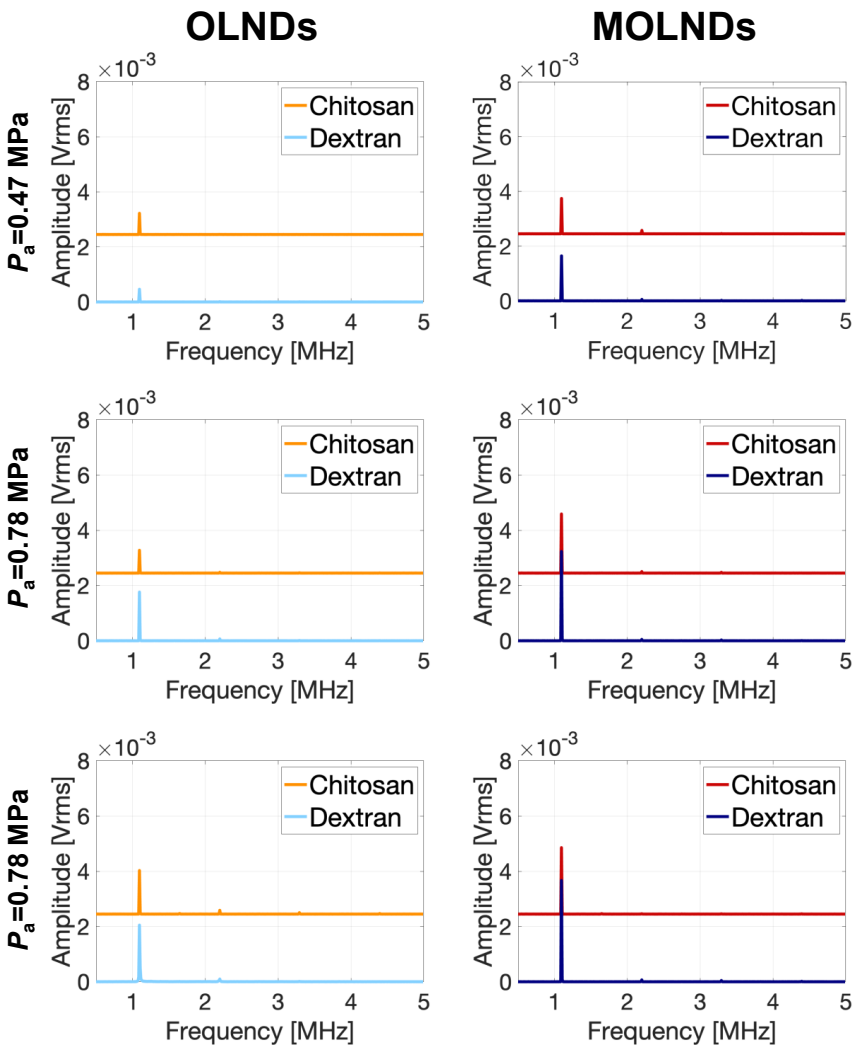



**Figure B.2.** Acoustic spectra of PFP-core OLNDs and MOLNDs with chitosan and dextran coating, measured at three acoustic pressures (0.47, 0.78 and 1.54 MPa). The reported results are based on the average of three acquired values.

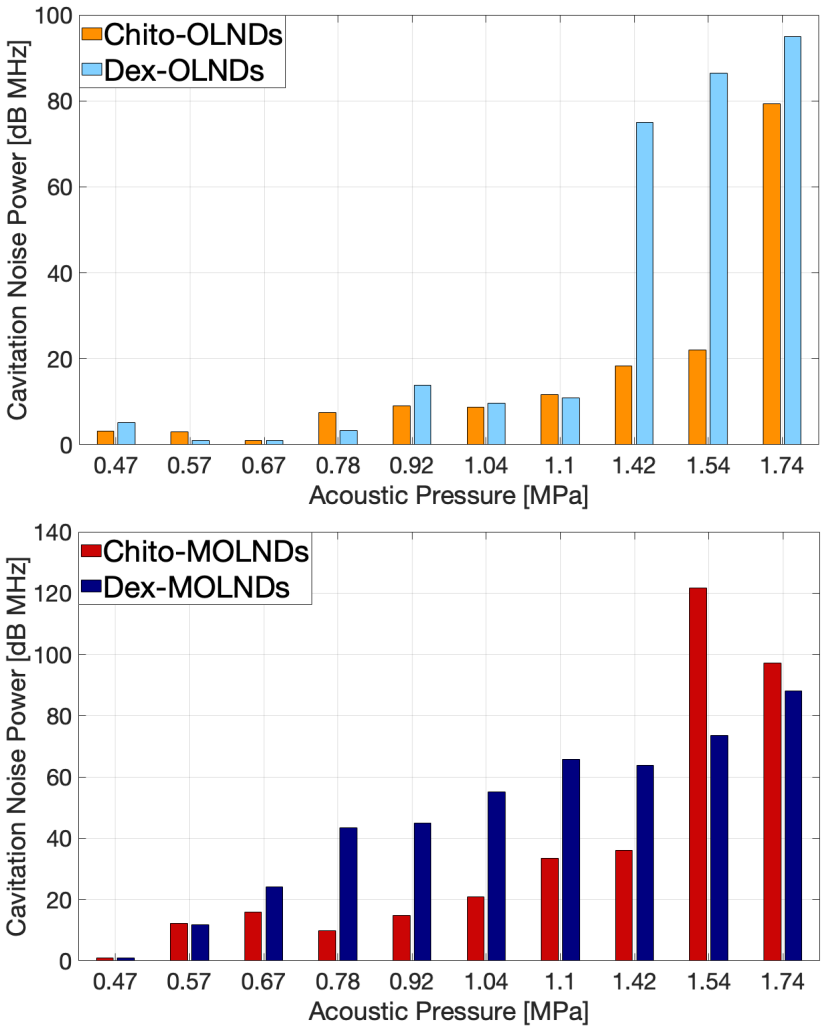



**Figure B.3.** Cavitation Noise Power (CNP) values evaluated in the acoustic pressure range 0.47-1.74 MPa for DFP-core nanodroplets: comparison between OLNDs (top) and MOLNDs (bottom). The reported results are based on the average of three acquired values.

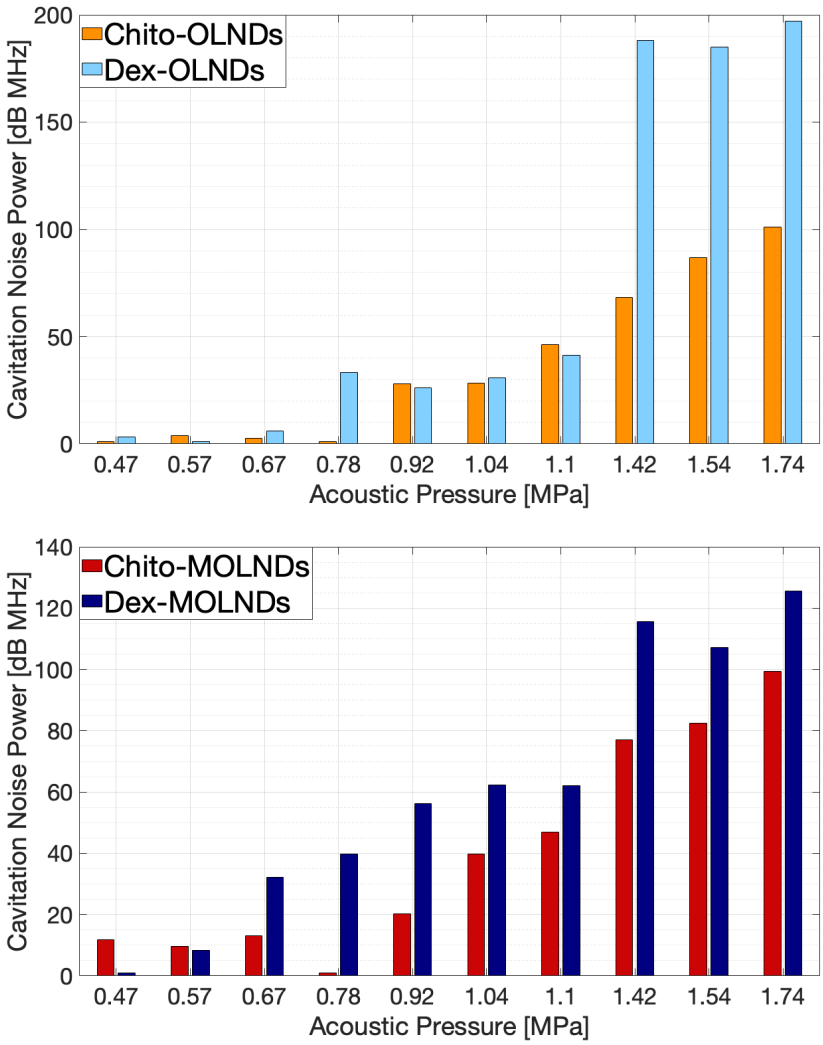



**Figure B.4.** Cavitation Noise Power (CNP) values evaluated in the acoustic pressure range 0.47-1.74 MPa for PFP-core nanodroplets: comparison between OLNDs (top) and MOLNDs (bottom). The reported results are based on the average of three acquired values.

## B.2 Numerical modeling of magnetic oxygen-loaded nanodroplet flow under magnetic field gradients

The simulation process unfolded through two steps, wherein the microfluidic flow of MOLNDs was simulated while subject to magnetic field gradients induced by a permanent magnet. After discretizing the magnet into $N$ hexahedral elements, the spatial distribution of its stray field was numerically calculated by integrating the following equation:

$$\mathbf{H}_{\text{magnet}}(\mathbf{r}) = \frac{1}{4\pi}\sum_{i=1}^{N}\int_{\partial\Omega_i}\mathbf{M}_{\text{magnet}}(\mathbf{r}_i)\cdot\mathbf{u}_i\frac{(\mathbf{r}-\mathbf{r}_i)}{\parallel\mathbf{r}-\mathbf{r}_i\parallel^3}ds \tag{B.1}$$

where $\mathbf{M}_{\text{magnet}}$ is the magnetization vector, $\partial\Omega_i$ is the surface of the $i$-th hexahedron having normal unit vector $\mathbf{u}_i$ and barycentre with vector position $\mathbf{r}_i$. [200]
Under the assumption of non-interacting MOLNDs and perfectly inelastic collisions with the channel walls, we described the trajectory (i.e., the time evolution of the vector position $\mathbf{s}$ and velocity $\mathbf{v}$) of a generic MOLND with mass $\chi$, hydrodynamic radius $R_{\text{hyd}}$ and magnetic moment $\mathbf{m}$ by the following equation:

$$\begin{cases}\chi\frac{d\mathbf{v}}{dt} = \mu_{\text{f}}(\mathbf{m}\cdot\nabla)\mathbf{H}_{\text{magnet}} - 6\pi\eta_{\text{f}}R_{\text{hyd}}(\mathbf{v}-\mathbf{v}_{\text{f}}) + \mathbf{F}_{\text{g}}\\ \frac{d\mathbf{s}}{dt} = \mathbf{v}\end{cases} \tag{B.2}$$

where $\mu_{\text{f}}$, $\eta_{\text{f}}$ and $\mathbf{v}_{\text{f}}$ are the magnetic permeability, viscosity and velocity of the fluid within the micro-channel, here considered to be water. [201] Neglecting the contribution of the chitosan or dextran coating, the MOLND mass $\chi$ was determined as:

$$\chi = \rho_{\text{core}}V_{\text{core}} + \rho_{\text{MNPs}}V_{\text{MNPs}}, \tag{B.3}$$

where $\rho_{\text{core}}$ and $\rho_{\text{MNPs}}$ are the densities of the MOLND core and of the decorating MNPs. The volumes of the core and of the MNP aggregates were extracted from DLS measurements (see Table 5.4 in Chapter 5) and observation of SEM/TEM images (see Figures 5.4 and 5.5 in Chapter 5), assuming as a first approximation that the MNP aggregates form a uniform layer on top of the OLND surface. The gravitational force $\mathbf{F}_{\text{g}}$, taking into account buoyancy effects, was expressed as:

$$\mathbf{F}_{\text{g}} = -\Big[\chi - \rho_{\text{f}}(V_{\text{core}} + V_{\text{MNPs}})\Big]\mathbf{g}, \tag{B.4}$$

where $\rho_{\text{f}}$ is the fluid density and $\mathbf{g}$ is the gravitational force vector. [202]
Under laminar flow conditions, the profile of the fluid velocity amplitude within the rectangular cross-section of the channel ($yz$-plane) was approximated as:

$$v_{\mathrm{f}} = v_{\mathrm{f_{max}}} \left[1 - \left(\frac{2y}{b}\right)^{n}\right] \left[1 - \left(\frac{2z}{a}\right)^{m}\right], \tag{B.5}$$

where $v_{\mathrm{f_{max}}}$ is the maximum fluid velocity, achieved at the channel center, $a$ and $b$ represent the width and thickness of the channel (with aspect ratio $b/a \leq 0.5$), and the parameters are $n = 2$ and $m = 1.7 + 0.5(b/a)^{-1.4}$. [203]
In Equation C.2, the magnetic moment of the MOLND was expressed using the Langevin function as:

$$\mathbf{m} = M_S \cdot V_{\mathrm{MNPs}} \left[ coth\left(\frac{\mathbf{H}_{\mathrm{magnet}}}{H_0}\right) - \frac{H_0}{\mathbf{H}_{\mathrm{magnet}}} \right] \tag{B.6}$$

where $M_{\mathrm{S}}$ is the saturation magnetization of the MNPs derived from their magnetization curve, measured with vibrating sample magnetometry, [38] and $H_0$ is a fitting parameter. [204]

The spatial distribution of the magnetic field amplitude generated by the magnet, utilized in the microfluidic experiments to assess the efficiency of magnetic decoration (see Section 5.1.3 in Chapter 5), was simulated. The results are presented in Figure B.5. In particular, the magnetic field amplitude decreases from 25 kA/m to around 10 kA/m along the 1.5 mm width channel, corresponding to a magnetic field gradient of $10 \times 10^3$ kA/m$^2$.

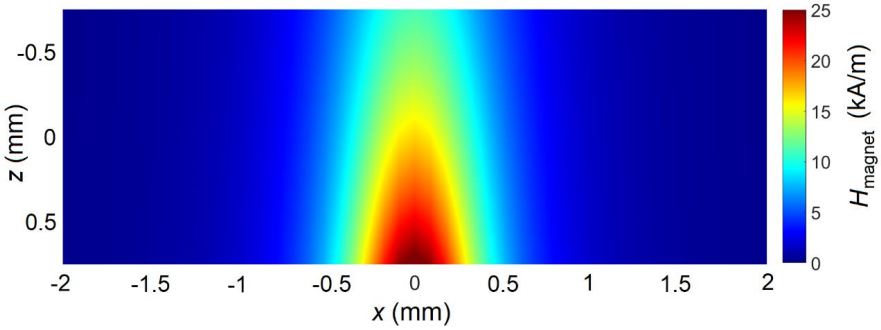



**Figure B.5.** Spatial distribution of the amplitude of the magnetic field produced by the permanent magnet in the $xz$-plane. The magnet is assumed to be uniformly magnetized along the out-of-plane direction, with a magnetization of 715 kA/m. The magnetization value was chosen to guarantee a good agreement between simulation and magnetic field measurement results obtained with a Hall probe.

To obtain a more comprehensive understanding of the trajectories of MOLNDs within the micro-channel, the outcomes of microfluidic experiments (outlined in Section 5.1.3 in Chapter 5) are validated through numerical modeling. The corresponding results are depicted in the Figure B.6. In particular, it can be observed

that the trajectories of MOLNDs inside the micro-channel are strongly influenced by the initial position of the droplets at the inlet. Due to the substantial variability in the MNP loading level, there is a significant dispersion in the magnetic moment of MOLNDs at saturation. The presented offer only an illustrative example, assuming a saturation magnetic moment of 0.042 pA $m^2$ for all chitosan-coated DFP-core MOLNDs injected in the micro-channel, and 0.0085 pA $m^2$ for all dextran-coated ones. The trajectories calculated in the *xz*-plane when the magnet is located at position 3 are presented in Figure B.6A for chitosan coating and Figure B.6B for dextran coating. For the latter, characterized by a reduced MNP loading and a lower magnetic moment, the overall trajectories are less influenced by the presence of the magnet. At larger distances from the magnet, the trajectory is slightly deviated, and only the nanodroplets closer to the magnet move towards it. On the contrary, for chitosan-coated MOLNDs, irrespective of the initial positions considered, the nanodroplets tend to move toward the channel wall where the magnet is positioned. In Figure B.6C, we present the simulation results obtained for the chitosan-coated MOLNDs when the magnet is located at position 1. The trajectories in the *xy*-plane highlight an opposing influence between the magnet and gravitational force, with the latter being dominant for the MOLNDs near the channel bottom surface. From the simulation results, in all cases, the deflection angles along the trajectory vary significantly, reaching values on the order of 90° when the MOLNDs approach the magnet. When comparing experimental and modeling results, strong discrepancies can be observed between the measured and calculated deflection angles. These differences can be attributed to various factors. Firstly, the evaluation of MOLND trajectories in the experimental analysis is limited to a small observation window (227×167 $\mu$m), which is only a fraction of the simulated area inside the channel, falling across the curvature of the simulated trajectories. Secondly, the model involves the assumptions of perfectly inelastic collisions, causing the stream of MOLNDs to stop when they collide with the channel wall. Lastly, the simulations assume a uniform distribution of magnetic decoration across the droplet surface, whereas SEM and TEM images have indicated the presence of MNP agglomerates with diameters around 150 nm.

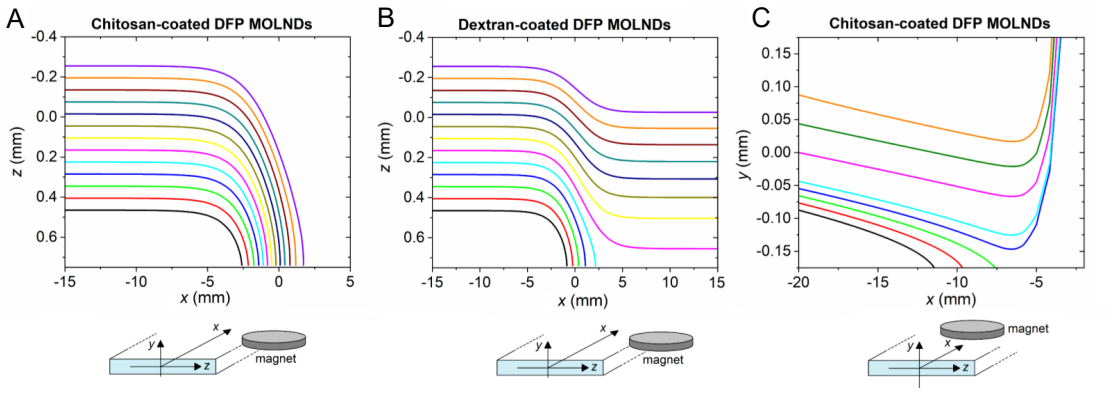



**Figure B.6.** Trajectories in $xz$-plane calculated for (**A**) chitosan-coated DFP-MOLNDs and (**B**) dextran-coated DFP-MOLNDs, for magnet position 3. (**C**) Trajectories in the $xy$-plane calculated for chitosan-coated DFP-MOLNDs, for magnet position 1. In the simulation graphs, the magnet center is positioned at $x = 20$ mm.

## B.3 Oxygen release following ultrasound field exposure

The evaluation of oxygen release from OLNDs was performed with an HQ 40D digital oximeter (Hach, Lainate, IT) connected with a LDO 101 luminescent/optical dissolved oxygen probe (Hach, Lainate, IT), placed in a small bath hermetically closed with an US transducer at the base (as shown in Figure B.7A), with a working frequency of 1 MHz resulting in an acoustic pressure of 0.13 MPa. The droplet suspension (5 mL), whose oxygen concentration level was previously collected and used as a reference, was exposed to US excitation for 270 s measuring and storing the oxygen concentration value every 30 s.

The results concerning the assessment of oxygen release from OLNDs samples are presented in Figure B.7B, illustrating the changes in oxygen concentration measured following the application of the US external stimulus (acoustic pressure = 0.13 MPa). The plots illustrate measurements over time, with the reported oxygen variation data being relative to the minimum value recorded during US exposure. Upon analyzing the different cores, it is noteworthy that for DFP-based OLNDs ($T_{boiling}$ = 51 °C), the oxygen concentration in the solution increases linearly, reaching significant increments of about 5 mg/L. In contrast, for the PFP-core, which has a lower boiling temperature ($T_{boiling}$ = 29 °C), the release of oxygen is less evident. For dextran-coated OLNDs, oxygen release beings before US stimulation, as the vaporization process is triggered by the ambient temperature. The distinct behavior between dextran and chitosan coatings could be attributed to the less rigid dextran-based shell.

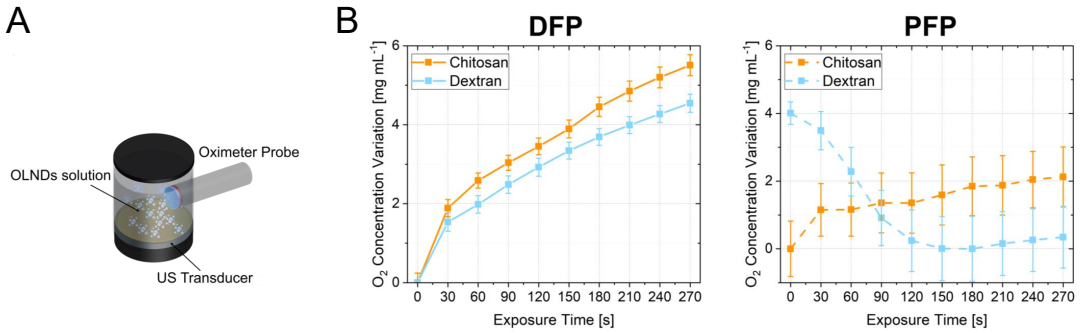



**Figure B.7.** (**A**) Visual depiction of the setup used to conduct oxygen release experiments on OLND samples during US exposure ($f_0$ = 1 MHz, $P_a$ = 0.13 MPa). (**B**) Variations of the oxygen concentration collected by the oximeter probe during US excitation over time (270 s).

# Appendix C

# Application of magnetic hyperthermia in radical polymerization processes

In this Appendix, the results of additional investigations carried out on the application of magnetic hyperthermia in radical polymerization, discussed in Chapter 6, are presented. In particular, the appendix reports rheological and mechanical characterizations of the hydrogels conducted at the University of Naples Federico II, and simulations conducted with heat-transfer numerical modeling.

## C.1 Mechanical tests of polyacrylamide hydrogels

The mechanical behavior of the hydrogels has been investigated through small amplitude oscillatory shear and unconfined compression tests conducted on cylindrical samples using an AR-G2 controlled stress rheometer (TA Instruments, New Castle, Delaware, USA). A plate-plate configuration featuring a Peltier base for temperature regulation (with a plate diameter of 25 mm) is utilized. To prevent slippage, a plate with a rough surface and a slight compression during oscillatory tests is employed. [205] The linear viscoelastic shear moduli are measured at 25 °C within the frequency range from $5 \times 10^{-2}$ to $5 \times 10^{1}$ rad/s. For uniaxial unconfined compression tests, samples are compressed between the rheometer's parallel plates at a rate of 10 $\mu$m/s. The normal force and sample height are continuously monitored to determine stress and strain. [206]
Oscillatory shear measurements also provide evidence of strong gel formation (Figure C.1A). Regardless of the polymerization conditions, all samples exhibit typical gel-like behavior characterized by viscoelastic shear moduli that are nearly independent of frequency, with the elastic modulus (G') significantly surpassing the

viscous modulus (G"). Further insights into the impact of different polymerization conditions can be gained by focusing on the elastic modulus, which is linked to the chemical structure of the polymeric network and the density of crosslinks. On one hand, no substantial differences are observed for samples obtained through bulk heating, even in the presence of MNPs, suggesting that the latter played a negligible role in the thermally triggered polymerization process. On the other hand, an increase in the elastic contribution is noted in the case of magnetic hyperthermia polymerization. Since the gel fraction is identical to that of the sample obtained through bulk heating (refer to Table 6.1 in Chapter 6), the influence of a higher crosslinking density can be discounted. Therefore, the higher G' is likely attributable to the formation of a more uniform crosslinked structure (with no temperature gradient effects as in bulk heating), wherein the MNPs are better integrated into the polymeric matrix. This aligns with the lower swelling degree of the gel obtained through magnetic hyperthermia polymerization, indicating the formation of a stiffer network.
Unconfined compression tests provide additional evidence to support this observation. As depicted in Figure C.1B, hyperthermia polymerization results in the formation of the most mechanically durable gel, characterized by a higher elastic modulus, $E_c$, and greater strength at larger deformations. Interestingly, both MNPs-containing gels exhibit a higher $E_c$ compared to the neat gel, despite having a lower gel fraction (as shown in the inset), indicating that the presence of MNPs contributes to enhancing mechanical resistance under compression. The summarized mechanical properties of the gels are presented in Table C.1.

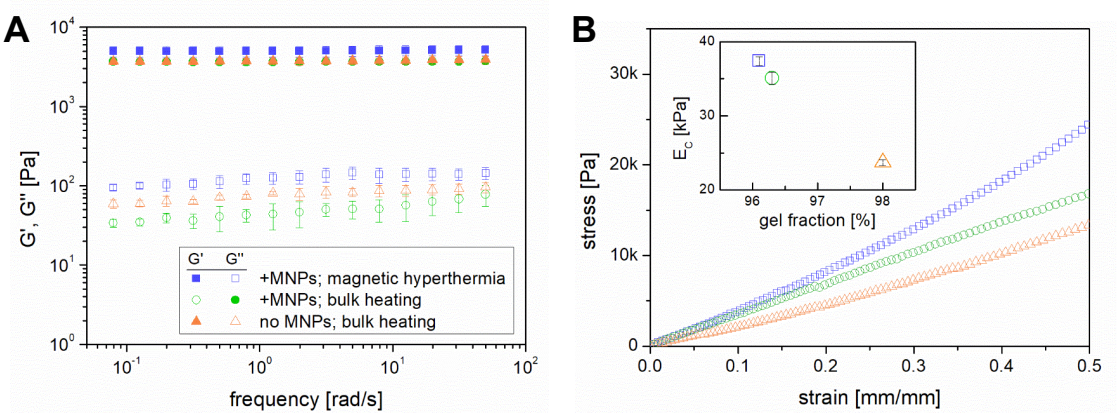



**Figure C.1.** Rheological and mechanical tests on hydrogels with and without $CoFe_2O_4$ NPs: (**A**) frequency dependence of the viscoelastic shear moduli; (**B**) stress-strain curves for unconfined compression.

**Table C.1.** Summary of the mechanical properties of the hydrogels.

| Hydrogel | MNPs | Type of polymerization | G' @ 1 rad/s [kPa] | $E_c$ [kPa] |
|---|---|---|---|---|
| 1 | ✓ | Magnetic hyperthermia | 4.95 ± 0.75 | 37.4 ± 0.6 |
| 2 | ✓ | Bulk heating | 3.71 ± 0.38 | 35.1 ± 0.8 |
| 3 | ✗ | Bulk heating | 3.64 ± 0.31 | 23.7 ± 0.4 |

Moreover, mechanical experiments have been conducted also on non-magnetic hydrogels polymerized by magnetic hyperthermia with MNPs concentrated in a small volume of the sample. To explore the impact of this process on the characteristics of the resulting hydrogel, we have been selected the 6 mL sample from Figure 6.8 in Chapter 6 (i.e., the one with the larger volume) for further analysis. Specifically, after removing the bottom part containing the MNPs, the remaining hydrogel is divided into two equally sized disk-shaped samples, which are then subjected to rheological tests. The results are presented in Figure C.2, where data from the hydrogel obtained through conventional bulk heating are also included for comparison purposes. It is evident from the rheological and mechanical tests that the properties of the two hydrogel slices are comparable. This suggests that the polymerization induced by the confined MNPs progresses uniformly throughout the sample, at least within the volumes investigated. Furthermore, both the elastic shear modulus (G') and elastic compression modulus ($E_C$) are similar to those of the hydrogel obtained through simple bulk heating, confirming the reliability and applicability of the proposed method.

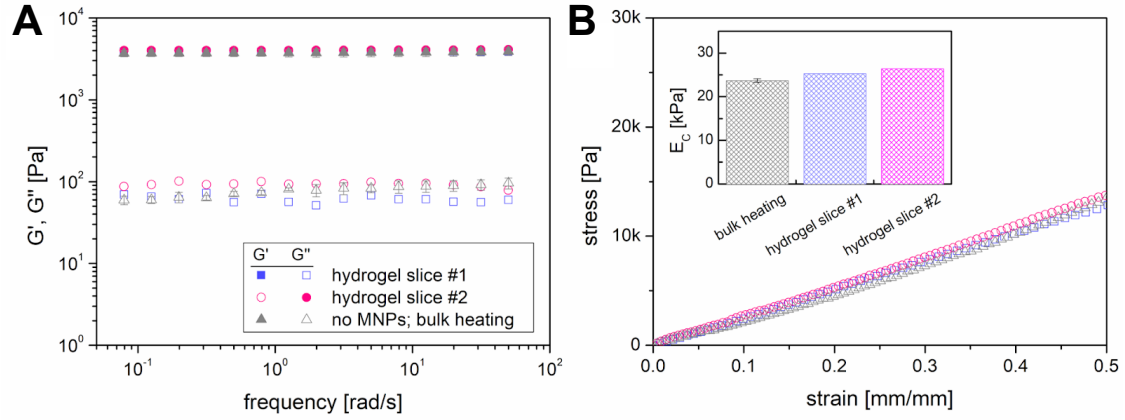



**Figure C.2.** Rheological and mechanical tests on non-magnetic hydrogels obtained by magnetic hyperthermia polymerization with confined MNPs. (**A**) Frequency dependence of the viscoelastic shear moduli; (**B**) stress-strain curves for unconfined compression (the computed elastic modulus is reported in the inset). "Gel slice #1" refers to the top slice, while "Gel slice #2" refers to the slice more in proximity to the MNPs. Data for the reference hydrogel obtained by simple bulk heating are the same as in Figure C.1.

## C.2 Heat transfer numerical modeling

The heating-cooling transient observed in the magnetic gel has been modeled using an in-house 3D finite element solver developed at Istituto Nazionale di Ricerca Metrologica. This software effectively calculates heat transfer within the system, accounting for minimal convective effects. The system includes the magnetic gel containing uniformly dispersed MNPs, the surrounding vial walls, and the air above the gel. [192] Specifically, the following equation was implemented:

$$\rho C_{\mathrm{p}} \frac{\partial T}{\partial t} = \nabla \cdot k \nabla T + \Gamma_1 Q_{\mathrm{MNPs}} + \Gamma_2 Q_{\mathrm{reaction}} \tag{C.1}$$

where $\rho$ is the density of the medium (magnetic gel, plastic vial or air), $C_{\mathrm{p}}$ is the medium heat capacity, $k$ is the medium thermal conductivity, $T$ is the temperature, $Q_{\mathrm{MNPs}}$ is the specific heating power released by MNPs under the action of an AC magnetic field, and $Q_{\mathrm{reaction}}$ is the specific heating power released by the exothermic reaction during the polymerization process. In particular, $Q_{\mathrm{MNPs}}$ is specified as the product of the SLP (determined from thermometric measurements) and the concentration of MNPs within the sample, whereas $Q_{\mathrm{reaction}}$ is determined from the measured enthalpy of reaction. $\Gamma_1$ and $\Gamma_2$ are piecewise functions that are set at 1 within the magnetic gel and zero elsewhere. Specifically, $\Gamma_1 \neq 0$ when the magnetic field is switched on, causing the MNPs to become activated, while $\Gamma_2 \neq 0$ during the exothermic reaction.
Equation C.1 is supplemented by the following boundary condition applied to the outer surface of the vial:

$$q = -k \frac{\partial T}{\partial t} = -h(T_{\mathrm{ext}} - T) \tag{C.2}$$

where $q$ is the outward heat flux, $h$ is the heat transfer coefficient, and $T_{\mathrm{ext}}$ is the external temperature, i.e. the room temperature.
The finite element solution for Equation C.1 was achieved by discretizing the analysis domain into a tetrahedral mesh and utilizing linear shape functions. Time integration was executed through the implementation of the Crank-Nicolson method. Table C.2 outlines the material properties utilized in the thermal simulations for the magnetic gel, the polyethylene vial, and the surrounding air. A uniform initial temperature throughout the system was assumed, corresponding to the external temperature of 26.4 °C. The heat transfer coefficient was set at 25 $\mathrm{W/m^2K}$ to describe the boundary condition for free convection in air. [207]

**Table C.2.** Summary of the material properties used in the thermal simulations.

| **Material** | $\rho$ [kg/m$^3$] | $\boldsymbol{C_p}$ [J/(kgK)] | $\boldsymbol{k}$ [W/(mK)] |
|---|---|---|---|
| Hydrogel [208] | 1024 | 6350 | 0.83 |
| Polyethylene | 950 | 1900 | 0.5 |
| Air | 1.16 | 1007 | 0.026 |

To interpret the experimental findings, numerical simulation of the heating-cooling transient during magnetic hyperthermia-induced polymerization has been conducted. This simulation employes the heat transfer model outlined above incorporating as inputs the SLP of the $CoFe_2O_4$ NPs, determined from thermometric measurements, and the enthalpy change associated with the polymerization reaction obtained from Differential Scanning Calorimetry (DSC). [209, 210] The heating efficiency of $CoFe_2O_4$ NPs has been assessed by fitting the initial slope of the heating curve (Figure 6.2 in the Chapter 6) to determine the SLP, estimated to be approximately 60 W/g.
Figure C.3A depicts the time evolution of the temperature, simulated at various locations within the magnetic gel (refer to Figure C.3B for their positions). The modeling outcomes closely align with experimental observations, reproducing the main phenomena occurring in the solution. Initially, there is a temperature rise driven by the activation of MNPs upon the application of the AC magnetic field. Subsequently, at around 6 minutes, as the solution temperature reaches 60 °C, the exothermic reaction starts, resulting in a further rise in the temperature curve slope. This is followed by a decline around 7.2 minutes, coinciding with the cessation of the AC magnetic field and the consequent stop of heat release from MNPs. The temperature continues to increase up to 7.7 minutes, marking the peak of polymerization enthalpy, after which a cooling phase initiates. Over the subsequent 6 minutes, the temperature decreases by approximately 25°C.
Figure C.3B presents the temperature distribution map calculated within the magnetic gel at the peak temperature, coinciding with the maximum heat released by the exothermic reaction. A slight temperature gradient is noticeable, with a change on the order of 1.2 °C within a volume measuring 3.5 mm, centered around the sample barycenter.
With the aid of the heat transfer model, we are able to explore strategies for optimizing the polymerization process. This involves varying factors such as the type of MNPs, their concentration in the solution, and the parameters of the AC magnetic field (peak amplitude $\hat{H}_a$ and frequency $f$). In an initial investigation, Figure C.3C illustrates the time duration required to reach a temperature of 60 °C as a function of $Q_{\mathrm{MNPs}}$, representing the specific heating power released by MNPs under the influence of an AC magnetic field. The data point indicated by the red circle corresponds to the values used to replicate the experimental outcomes; specifically,

in this scenario, approximately 6 minutes of magnetic hyperthermia application are adequate to initiate polymerization. This time frame can be potentially reduced by enhancing factors contributing to $Q_{\mathrm{MNPs}}$, such as the SLP of MNPs (dependent on MNP type and/or excitation parameters) and their concentration.

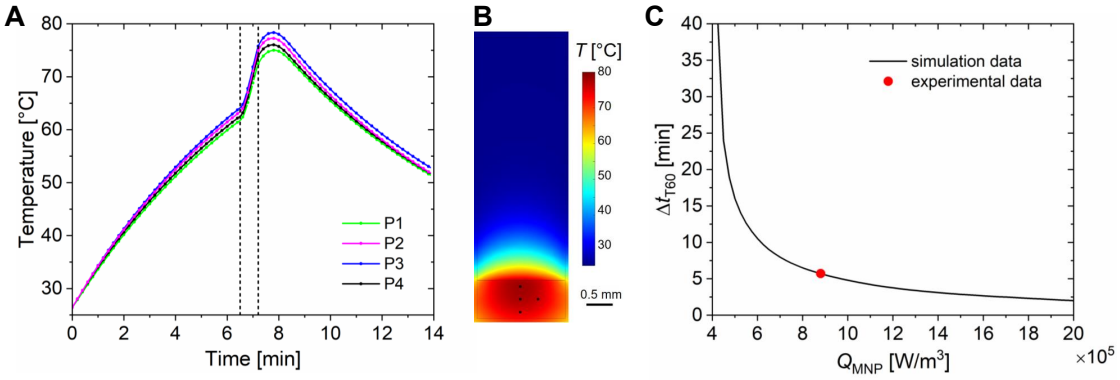



**Figure C.3.** (**A**) Simulated heating-cooling transients at different points within the sample, whose positions are marked in the map of Figure **B**. The time instants corresponding to the polymerization reaction start and the AC magnetic field switching off are indicated with dashed lines. (**B**) Spatial distribution of the temperature calculated on the longitudinal section of the vial at the temperature peak, associated with the maximal enthalpy change during the polymerization reaction. (**C**) Time interval required to reach 60 °C, as a function of the specific heating power released by MNPs (the experimental data is indicated with a red circle as a reference).

In Figure C.4, a comparison of the thermal properties of two types of commercial iron oxide NPs is presented: core-shell NPs with a citrate shell from NanoMaterials Technology Pte Ltd, referred to as JHU NPs, and matrix-based NPs composed of superparamagnetic iron oxide NPs dispersed in a dextran matrix from micromod Partikeltechnologie GmbH, known as nanomag®-D-spio NPs. [211] Figure C.4A and Figure C.4B display SLP values as a function of $\hat{H}$a derived through polynomial fitting at two different frequencies (150 and 300 kHz) for JHU and nanomag®-D-spio NPs, respectively. [201] For JHU NPs, at $f = 150$ kHz, the SLP ranges from 150 W/g to 480 W/g within the range of $\hat{H}_{\mathrm{a}}$ $10 - 40$kA/m, while at $f = 300$ kHz, the SLP ranges from 50 W/g to 780 W/g within the range of $\hat{H}_{\mathrm{a}}$ 5-20 kA/m. For nanomag®-D-spio NPs, at $f = 150$ kHz, the SLP varies from 15 W/g to 45 W/g within the range of $\hat{H}_{\mathrm{a}}$ 10-40 kA/m, and at $f = 300$ kHz, the SLP ranges from 15 W/g to 70 W/g within the range of $\hat{H}_{\mathrm{a}}$ 5-20 kA/m.
In Figures C.4C-F, maps are presented illustrating the time required for the application of the AC magnetic field to reach 60 °C ($\Delta t_{\mathrm{T60}}$) as a function of $\hat{H}$a value and NP concentration; for each sample, diagrams corresponding to frequencies of 150 and 300 kHz are provided. Due to the distinct heating properties, concentrations

of MNPs on the order of 5 mg/mL may suffice to achieve 60 °C and initiate polymerization within 2 min when employing JHU NPs and AC magnetic fields with $f$ = 150 kHz and $\hat{H}_{\mathrm{a}} = 40$ kA/m (Figure C.4C). Even lower concentrations (approximately 3 mg/mL) and magnetic field peak amplitudes (20 kA/m) could be required when $f = 300$ kHz (Figure C.3D). Conversely, when using nanomag®-D-spio NPs, higher concentrations are necessary. In this scenario, to initiate polymerization at 60 °C within 2 min, concentrations around 40 mg/mL are required when $f = 150$ kHz and $\hat{H}_{\mathrm{a}} = 40$ kA/m (Figure C.3F), while concentrations of at least 30 mg/mL are needed when $f = 300$ kHz and $\hat{H}_{\mathrm{a}} = 20$ kA/m.
In conclusion, this model provides a strategy for optimizing the polymerization process, providing feedback on how reducing the polymerization time by playing with MNP concentration and AC magnetic field parameters.

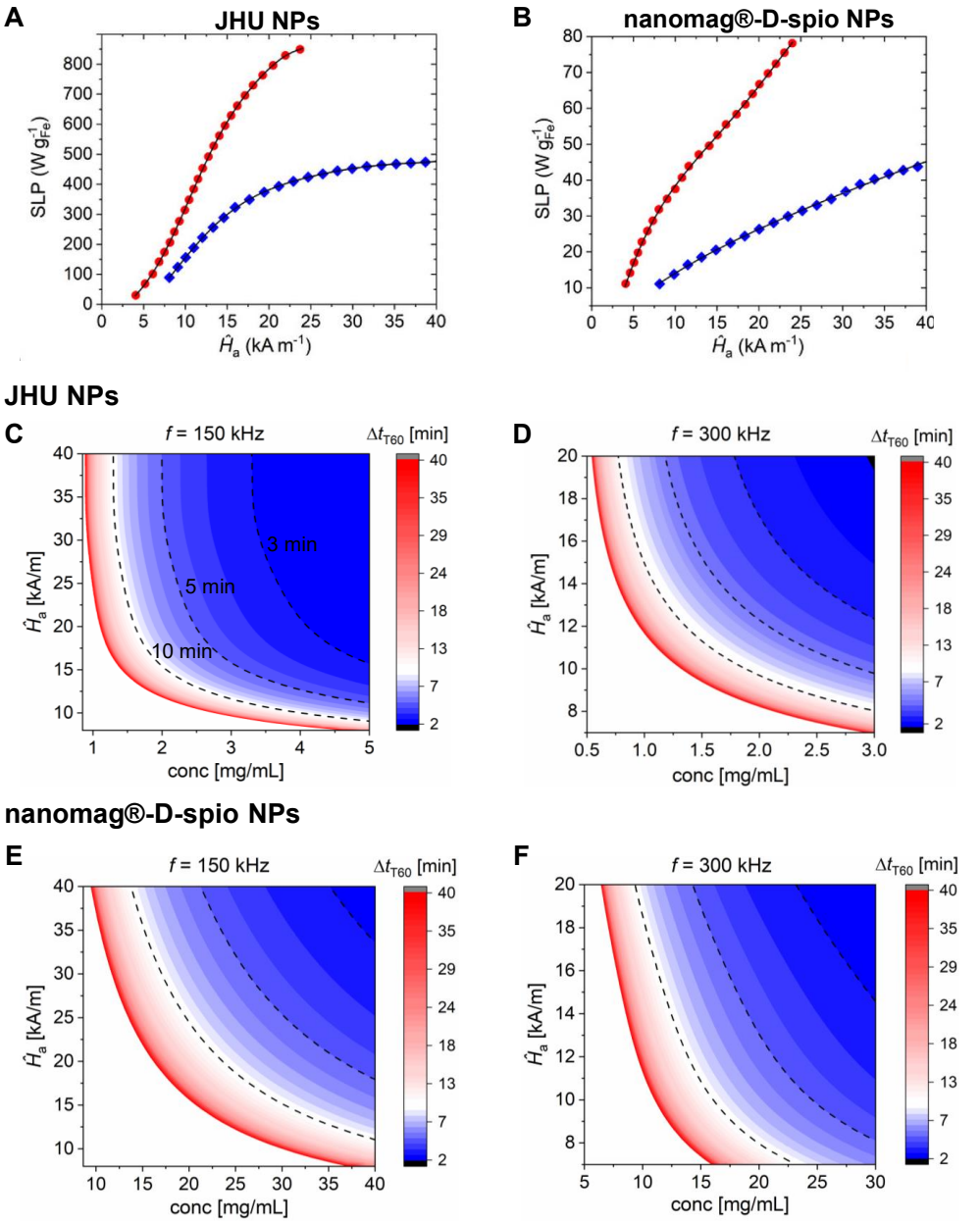



**Figure C.4.** SLP versus AC magnetic field peak amplitude for two frequencies (150 and 300 kHz), for (**A**) JHU NPs, and (**B**) nanomag®-D-spio NPs. The blue and red markers correspond to the experimental data extrapolated from the literature, [211] whereas the black curves to their polynomial interpolation. Diagrams of the time interval required to reach 60 °C, as a function of MNP concentration and magnetic field peak amplitude, when using commercial MNPs, namely (**C-D**) JHU NPs and(**E-F**) nanomag®-D-spio NPs.

# Bibliography


[1] M. Colombo et al. “Biological applications of magnetic nanoparticles”. In: *Chemical Society Reviews* 41.11 (2012), pp. 4306–4334.

[2] K. Tang et al. “Design and synthesis of bioinspired nanomaterials for biomedical application”. In: *Wiley Interdisciplinary Reviews: Nanomedicine and Nanobiotechnology* 16.1 (2024), e1914.

[3] H. Inam et al. “Magnetic Hydroxyapatite Nanoparticles in Regenerative Medicine and Nanomedicine”. In: *International Journal of Molecular Sciences* 25.5 (2024), p. 2809.

[4] H. Zhou et al. “Harnessing Nanomedicine for Cartilage Repair: Design Considerations and Recent Advances in Biomaterials”. In: *ACS nano* (2024).

[5] P. Padmanabhan et al. “Nanoparticles in practice for molecular-imaging applications: an overview”. In: *Acta biomaterialia* 41 (2016), pp. 1–16.

[6] J. K. Patra et al. “Nano based drug delivery systems: recent developments and future prospects”. In: *Journal of nanobiotechnology* 16 (2018), pp. 1–33.

[7] W. H. De Jong and P. J. Borm. “Drug delivery and nanoparticles: applications and hazards”. In: *International journal of nanomedicine* 3.2 (2008), pp. 133–149.

[8] S. Soares et al. “Nanomedicine: principles, properties, and regulatory issues”. In: *Frontiers in chemistry* 6 (2018), p. 356901.

[9] M. Byakodi et al. “Emerging 0D, 1D, 2D, and 3D nanostructures for efficient point-of-care biosensing”. In: *Biosensors and Bioelectronics: X* 12 (2022), p. 100284.

[10] J.-B. Coty and C. Vauthier. “Characterization of nanomedicines: A reflection on a field under construction needed for clinical translation success”. In: *Journal of controlled release* 275 (2018), pp. 254–268.

[11] R. Abbasi et al. “Structural parameters of nanoparticles affecting their toxicity for biomedical applications: a review”. In: *Journal of Nanoparticle Research* 25.3 (2023), p. 43.

[12] P. M. Martins et al. “Magnetic nanoparticles for biomedical applications: from the soul of the earth to the deep history of ourselves”. In: *ACS Applied Bio Materials* 4.8 (2021), pp. 5839–5870.

[13] L. Mohammed et al. “Magnetic nanoparticles for environmental and biomedical applications: A review”. In: *Particuology* 30 (2017), pp. 1–14.

[14] M. M. Woldeamanuel et al. “Role of Magnetic Nanomaterials in Environmental Remediation”. In: *Iron Oxide-Based Nanocomposites and Nanoenzymes: Fundamentals and Applications*. Springer, 2024, pp. 185–208.

[15] S. S. S. Rani, S. Radhika, and C. Padma. “Single-Domain Hard Ferromagnetic M-SrFe Nanoparticles for Magnetic Data Storage”. In: *Journal of Metastable and Nanocrystalline Materials* 38 (2024), pp. 31–41.

[16] H. A. Alsalmah, A. Rajeh, and O. Nur. “Optical, conductivity, dielectric, and magnetic properties of polymer nanocomposite based on PAM/cs matrix and ZnFe2O4 NPs for use in magneto-electronic and energy storage capacitor devices”. In: *Ceramics International* (2024).

[17] M. Gholinejad et al. “Cysteine and ionic liquid modified magnetic nanoparticles supported RuCu as a new bimetallic catalyst in reduction reactions”. In: *Journal of Molecular Structure* 1298 (2024), p. 137100.

[18] L. Geng et al. “Magnetite nanoparticles immobilized on hydrophilic polyelectrolyte-grafted carbon nanotube as efficient organic–inorganic hybrid heterogeneous catalyst for Knoevenagel condensation in aqueous medium”. In: *Colloids and Surfaces A: Physicochemical and Engineering Aspects* 685 (2024), p. 133283.

[19] C. Jiang, C. W. Leung, and P. W. Pong. “Self-assembled thin films of Fe3O4-Ag composite nanoparticles for spintronic applications”. In: *Applied Surface Science* 419 (2017), pp. 692–696.

[20] M. Vaseem et al. “Iron oxide nanoparticle-based magnetic ink development for fully printed tunable radio-frequency devices”. In: *Advanced Materials Technologies* 3.4 (2018), p. 1700242.

[21] X. Song et al. “Preparation and characterization of biofunctionalized chitosan/Fe3O4 magnetic nanoparticles for application in liver magnetic resonance imaging”. In: *Journal of Magnetism and Magnetic Materials* 388 (2015), pp. 116–122.

[22] H. Li et al. “Progress in magnetic Fe3O4 nanomaterials in magnetic resonance imaging”. In: *Nanotechnology Reviews* 9.1 (2020), pp. 1265–1283.

[23] Z. Yuanbi, Q. Zumin, and J. Huang. “Preparation and analysis of Fe3O4 magnetic nanoparticles used as targeted-drug carriers”. In: *Chinese Journal of Chemical Engineering* 16.3 (2008), pp. 451–455.

[24] L. Shen, B. Li, and Y. Qiao. "Fe3O4 nanoparticles in targeted drug/gene delivery systems". In: *Materials* 11.2 (2018), p. 324.

[25] Y. V. Kolen'ko et al. "Large-scale synthesis of colloidal Fe3O4 nanoparticles exhibiting high heating efficiency in magnetic hyperthermia". In: *The Journal of Physical Chemistry C* 118.16 (2014), pp. 8691–8701.

[26] H. Chen et al. "Tuning the dynamics in Fe3O4 nanoparticles for hyperthermia optimization". In: *Applied Physics Letters* 117.7 (2020).

[27] G. Zhang et al. "One-pot solvothermal method to prepare functionalized Fe3O4 nanoparticles for bioseparation". In: *Journal of Materials Research* 27.7 (2012), pp. 1006–1013.

[28] J. Kim et al. "Scalable solvothermal synthesis of superparamagnetic Fe3O4 nanoclusters for bioseparation and theragnostic probes". In: *ACS Applied Materials & Interfaces* 10.49 (2018), pp. 41935–41946.

[29] K. D. Petrov and A. S. Chubarov. "Magnetite nanoparticles for biomedical applications". In: *Encyclopedia* 2.4 (2022), pp. 1811–1828.

[30] I. M. Obaidat et al. "Principles of magnetic hyperthermia: a focus on using multifunctional hybrid magnetic nanoparticles". In: *Magnetochemistry* 5.4 (2019), p. 67.

[31] K. McNerny et al. "Chemical synthesis of monodisperse $\gamma$-Fe–Ni magnetic nanoparticles with tunable Curie temperatures for self-regulated hyperthermia". In: *Journal of applied physics* 107.9 (2010).

[32] M. M. Selim et al. "A review of magnetic nanoparticles used in nanomedicine". In: *APL Materials* 12.1 (2024).

[33] J. Garg et al. "Emerging trends in zinc ferrite nanoparticles for biomedical and environmental applications". In: *Applied biochemistry and biotechnology* 196.2 (2024), pp. 1008–1043.

[34] S. Y. Srinivasan et al. "Applications of cobalt ferrite nanoparticles in biomedical nanotechnology". In: *Nanomedicine* 13.10 (2018), pp. 1221–1238.

[35] K. Wu et al. "Magnetic nanoparticles in nanomedicine: a review of recent advances". In: *Nanotechnology* 30.50 (2019), p. 502003.

[36] B. Rezaei et al. "Magnetic nanoparticles: a review on synthesis, characterization, functionalization, and biomedical applications". In: *Small* 20.5 (2024), p. 2304848.

[37] Z. W. Tay et al. "Magnetic particle imaging-guided heating in vivo using gradient fields for arbitrary localization of magnetic hyperthermia therapy". In: *ACS nano* 12.4 (2018), pp. 3699–3713.

[38] M. Vassallo et al. “Improvement of Hyperthermia Properties of Iron Oxide Nanoparticles by Surface Coating”. In: *ACS omega* 8.2 (2023), pp. 2143–2154.

[39] W. M. O. De Santana et al. “Ureasil–Polyether–CoFe2O4 Nanocomposites: Coupling a Drug Delivery System and Magnetic Hyperthermia”. In: *ACS Applied Polymer Materials* 3.10 (2021), pp. 4837–4848.

[40] V. V. Mody, A. Singh, and B. Wesley. “Basics of magnetic nanoparticles for their application in the field of magnetic fluid hyperthermia”. In: *European Journal of Nanomedicine* 5.1 (2013), pp. 11–21.

[41] Q. A. Pankhurst et al. “Applications of magnetic nanoparticles in biomedicine”. In: *Journal of physics D: Applied physics* 36.13 (2003), R167.

[42] A. G. Kolhatkar et al. “Tuning the magnetic properties of nanoparticles”. In: *International journal of molecular sciences* 14.8 (2013), pp. 15977–16009.

[43] R. Wildeboer, P. Southern, and Q. Pankhurst. “On the reliable measurement of specific absorption rates and intrinsic loss parameters in magnetic hyperthermia materials”. In: *Journal of Physics D: Applied Physics* 47.49 (2014), p. 495003.

[44] S. Tong et al. “Size-dependent heating of magnetic iron oxide nanoparticles”. In: *ACS nano* 11.7 (2017), pp. 6808–6816.

[45] E. C. Abenojar et al. “Structural effects on the magnetic hyperthermia properties of iron oxide nanoparticles”. In: *Progress in Natural Science: Materials International* 26.5 (2016), pp. 440–448.

[46] N. A. Usov et al. “Heating ability of magnetic nanoparticles with cubic and combined anisotropy”. In: *Beilstein Journal of Nanotechnology* 10.1 (2019), pp. 305–314.

[47] D. Cabrera et al. “Influence of the aggregation, concentration, and viscosity on the nanomagnetism of iron oxide nanoparticle colloids for magnetic hyperthermia”. In: *Journal of Nanoparticle Research* 17.3 (2015), p. 121.

[48] G. Salas et al. “Modulation of magnetic heating via dipolar magnetic interactions in monodisperse and crystalline iron oxide nanoparticles”. In: *The Journal of Physical Chemistry C* 118.34 (2014), pp. 19985–19994.

[49] G. Barrera, P. Allia, and P. Tiberto. “Dipolar interactions among magnetite nanoparticles for magnetic hyperthermia: A rate-equation approach”. In: *Nanoscale* 13.7 (2021), pp. 4103–4121.

[50] M. S. Darwish et al. “Synthesis of magnetic ferrite nanoparticles with high hyperthermia performance via a controlled co-precipitation method”. In: *Nanomaterials* 9.8 (2019), p. 1176.

[51] P. B. Balakrishnan et al. “Exploiting unique alignment of cobalt ferrite nanoparticles, mild hyperthermia, and controlled intrinsic cobalt toxicity for cancer therapy”. In: *Advanced Materials* 32.45 (2020), p. 2003712.

[52] D. Lachowicz et al. “Enhanced hyperthermic properties of biocompatible zinc ferrite nanoparticles with a charged polysaccharide coating”. In: *Journal of materials chemistry B* 7.18 (2019), pp. 2962–2973.

[53] X. Liu et al. “Comprehensive understanding of magnetic hyperthermia for improving antitumor therapeutic efficacy”. In: *Theranostics* 10.8 (2020), p. 3793.

[54] C. Kittel. *Introduction to solid state physics*. John Wiley & Sons, 2004.

[55] R. Ferrero et al. “Experimental and modelling analysis of the hyperthermia properties of iron oxide nanocubes”. In: *Nanomaterials* 11.9 (2021), p. 2179.

[56] R. Ferrero, M. Vicentini, and A. Manzin. “Influence of size, volume concentration and aggregation state on magnetic nanoparticle hyperthermia properties versus excitation conditions”. In: *Nanoscale Advances* 6.6 (2024), pp. 1739–1749.

[57] A. Sathya et al. “Co x Fe3–x O4 nanocubes for theranostic applications: effect of cobalt content and particle size”. In: *Chemistry of Materials* 28.6 (2016), pp. 1769–1780.

[58] A. Omelyanchik et al. “Magnetocrystalline and surface anisotropy in cofe2o4 nanoparticles”. In: *Nanomaterials* 10.7 (2020), p. 1288.

[59] T. Dippong, E. A. Levei, and O. Cadar. “Recent advances in synthesis and applications of MFe2O4 (M= Co, Cu, Mn, Ni, Zn) nanoparticles”. In: *Nanomaterials* 11.6 (2021), p. 1560.

[60] E. Fantechi et al. “Influence of cobalt doping on the hyperthermic efficiency of magnetite nanoparticles”. In: *Journal of Magnetism and Magnetic Materials* 380 (2015), pp. 365–371.

[61] L. Phong et al. “Structural, magnetic and hyperthermia properties and their correlation in cobalt-doped magnetite nanoparticles”. In: *RSC advances* 12.2 (2022), pp. 698–707.

[62] D. Zahn et al. “Optimization of Magnetic Cobalt Ferrite Nanoparticles for Magnetic Heating Applications in Biomedical Technology”. In: *Nanomaterials* 13.10 (2023), p. 1673.

[63] N. Datta et al. “Local hyperthermia combined with radiotherapy and-/or chemotherapy: Recent advances and promises for the future”. In: *Cancer treatment reviews* 41.9 (2015), pp. 742–753.

[64] S. Jha, P. K. Sharma, and R. Malviya. "Hyperthermia: role and risk factor for cancer treatment". In: *Achievements in the life sciences* 10.2 (2016), pp. 161–167.

[65] K. Ahmed, Y. Tabuchi, and T. Kondo. "Hyperthermia: an effective strategy to induce apoptosis in cancer cells". In: *Apoptosis* 20 (2015), pp. 1411–1419.

[66] M. Johannsen et al. "Clinical hyperthermia of prostate cancer using magnetic nanoparticles: presentation of a new interstitial technique". In: *International journal of hyperthermia* 21.7 (2005), pp. 637–647.

[67] M. Johannsen et al. "Thermotherapy of prostate cancer using magnetic nanoparticles: feasibility, imaging, and three-dimensional temperature distribution". In: *European urology* 52.6 (2007), pp. 1653–1662.

[68] K. Maier-Hauff et al. "Efficacy and safety of intratumoral thermotherapy using magnetic iron-oxide nanoparticles combined with external beam radiotherapy on patients with recurrent glioblastoma multiforme". In: *Journal of neuro-oncology* 103 (2011), pp. 317–324.

[69] W. J. Atkinson, I. A. Brezovich, and D. P. Chakraborty. "Usable frequencies in hyperthermia with thermal seeds". In: *IEEE Transactions on Biomedical Engineering* 1 (1984), pp. 70–75.

[70] R. Hergt and S. Dutz. "Magnetic particle hyperthermia—biophysical limitations of a visionary tumour therapy". In: *Journal of Magnetism and Magnetic Materials* 311.1 (2007), pp. 187–192.

[71] S. Dutz and R. Hergt. "Magnetic nanoparticle heating and heat transfer on a microscale: Basic principles, realities and physical limitations of hyperthermia for tumour therapy". In: *International Journal of Hyperthermia* 29.8 (2013), pp. 790–800.

[72] A. Bisazza et al. "Microbubble-mediated oxygen delivery to hypoxic tissues as a new therapeutic device". In: *2008 30th Annual International Conference of the IEEE Engineering in Medicine and Biology Society*. IEEE. 2008, pp. 2067–2070.

[73] C. Magnetto et al. "Ultrasound-activated decafluoropentane-cored and chitosan-shelled nanodroplets for oxygen delivery to hypoxic cutaneous tissues". In: *RSC Adv.* 4.72 (2014), pp. 38433–38441.

[74] M. Xavierselvan et al. "Photoacoustic nanodroplets for oxygen enhanced photodynamic therapy of cancer". In: *Photoacoustics* 25 (2022), p. 100306.

[75] H. Fu et al. "An ultrasound activated oxygen generation nanosystem specifically alleviates myocardial hypoxemia and promotes cell survival following acute myocardial infarction". In: *Journal of Materials Chemistry B* 8.28 (2020), pp. 6059–6068.

[76] B. Yang et al. “Engineered drug delivery nanosystems for tumor microenvironment normalization therapy”. In: *Nano Today* 49 (2023), p. 101766.

[77] H. Fang et al. “Biomimetic oxygen delivery nanoparticles for enhancing photodynamic therapy in triple-negative breast cancer”. In: *Journal of nanobiotechnology* 19 (2021), pp. 1–14.

[78] H. Lea-Banks et al. “Ultrasound-triggered oxygen-loaded nanodroplets enhance and monitor cerebral damage from sonodynamic therapy”. In: *Nanotheranostics* 6.4 (2022), p. 376.

[79] E. G. Schutt et al. “Injectable microbubbles as contrast agents for diagnostic ultrasound imaging: the key role of perfluorochemicals”. In: *Angewandte Chemie International Edition* 42.28 (2003), pp. 3218–3235.

[80] M. Prato et al. “2H, 3H-decafluoropentane-based nanodroplets: new perspectives for oxygen delivery to hypoxic cutaneous tissues”. In: *PLoS One* 10.3 (2015), e0119769.

[81] J. J. Kwan et al. “Theranostic oxygen delivery using ultrasound and microbubbles”. In: *Theranostics* 2.12 (2012), p. 1174.

[82] R. Cavalli et al. “Preparation and characterization of dextran nanobubbles for oxygen delivery”. In: *International Journal of Pharmaceutics* 381.2 (2009), pp. 160–165.

[83] R. Cavalli et al. “Ultrasound-mediated oxygen delivery from chitosan nanobubbles”. In: *International journal of pharmaceutics* 378.1-2 (2009), pp. 215–217.

[84] E. A. Neppiras. “Acoustic cavitation”. In: *Physics reports* 61.3 (1980), pp. 159–251.

[85] S. Galati and A. Troia. “Multiple Approaches for Ultrasonic Cavitation Monitoring of Oxygen-Loaded Nanodroplets”. In: *International Journal of Physical and Mathematical Sciences* 15.4 (2021), pp. 57–62.

[86] O. D. Kripfgans et al. “Acoustic droplet vaporization for therapeutic and diagnostic applications”. In: *Ultrasound in medicine & biology* 26.7 (2000), pp. 1177–1189.

[87] E. Strohm et al. “Vaporization of perfluorocarbon droplets using optical irradiation”. In: *Biomedical Optics Express* 2.6 (2011), pp. 1432–1442.

[88] S. Galati et al. “Dual-responsive magnetic nanodroplets for controlled oxygen release via ultrasound and magnetic stimulation”. In: *Nanoscale* (2024).

[89] Z. Teng et al. “A magnetic droplet vaporization approach using perfluorohexane-encapsulated magnetic mesoporous particles for ultrasound imaging and tumor ablation”. In: *Biomaterials* 134 (2017), pp. 43–50.

[90] J. Wang et al. “Magnetic Nanodroplets for Enhanced Deep Penetration of Solid Tumors and Simultaneous Magnetothermal-Sensitized Immunotherapy against Tumor Proliferation and Metastasis”. In: *Advanced Healthcare Materials* 11.23 (2022), p. 2201399.

[91] Ş. H. Şanlıer et al. “Development of ultrasound-triggered and magnetic-targeted nanobubble system for dual-drug delivery”. In: *Journal of pharmaceutical sciences* 108.3 (2019), pp. 1272–1283.

[92] S. A. Ansari et al. “Step-by-Step Design of New Theranostic Nanoformulations: Multifunctional Nanovectors for Radio-Chemo-Hyperthermic Therapy under Physical Targeting”. In: *Molecules* 26.15 (2021), p. 4591.

[93] E. Ficiarà et al. “Beyond oncological hyperthermia: physically drivable magnetic nanobubbles as novel multipurpose theranostic carriers in the central nervous system”. In: *Molecules* 25.9 (2020), p. 2104.

[94] S. Zullino et al. “Superparamagnetic oxygen-loaded nanobubbles to enhance tumor oxygenation during hyperthermia”. In: *Frontiers in Pharmacology* 10 (2019), p. 1001.

[95] A. Khadjavi et al. “‘In Vitro’,‘In Vivo’and ‘In Silico’investigation of the anticancer effectiveness of oxygen-loaded chitosan-shelled nanodroplets as potential drug vector”. In: *Pharmaceutical Research* 35 (2018), pp. 1–11.

[96] W. Song et al. “Magnetic nanobubbles with potential for targeted drug delivery and trimodal imaging in breast cancer: an in vitro study”. In: *Nanomedicine* 12.9 (2017), pp. 991–1009.

[97] K. Matyjaszewski and T. P Davis. *Handbook of radical polymerization*. Wiley Online Library, 2002.

[98] N. Ballard and J. M. Asua. “Radical polymerization of acrylic monomers: An overview”. In: *Progress in Polymer Science* 79 (2018), pp. 40–60.

[99] M. Ganglani, S. H. Carr, and J. M. Torkelson. “Influence of cure via network structure on mechanical properties of a free-radical polymerizing thermoset”. In: *Polymer* 43.9 (2002), pp. 2747–2760.

[100] N. Ilie, A. Keßler, and J. Durner. “Influence of various irradiation processes on the mechanical properties and polymerisation kinetics of bulk-fill resin based composites”. In: *Journal of dentistry* 41.8 (2013), pp. 695–702.

[101] H. Fang and C. A. Guymon. “Recent advances to decrease shrinkage stress and enhance mechanical properties in free radical polymerization: A review”. In: *Polymer international* 71.5 (2022), pp. 596–607.

[102] M. Chen, M. Zhong, and J. A. Johnson. “Light-controlled radical polymerization: mechanisms, methods, and applications”. In: *Chemical reviews* 116.17 (2016), pp. 10167–10211.

[103] P. Chmielarz et al. “Electrochemically mediated atom transfer radical polymerization (eATRP)”. In: *Progress in Polymer Science* 69 (2017), pp. 47–78.

[104] F. Wiesbrock, R. Hoogenboom, and U. S. Schubert. “Microwave-assisted polymer synthesis: state-of-the-art and future perspectives”. In: *Macromolecular Rapid Communications* 25.20 (2004), pp. 1739–1764.

[105] L. Debbi et al. “Ultrasound Mediated Polymerization for Cell Delivery, Drug Delivery, and 3D Printing”. In: *Small Methods* (2024), p. 2301197.

[106] J. Fischer and M. Wegener. “Three-dimensional optical laser lithography beyond the diffraction limit”. In: *Laser & Photonics Reviews* 7.1 (2013), pp. 22–44.

[107] A. Bagheri and J. Jin. “Photopolymerization in 3D printing”. In: *ACS Applied Polymer Materials* 1.4 (2019), pp. 593–611.

[108] I. De Bellis et al. “Two-Photon Laser Writing of Soft Responsive Polymers via Temperature-Controlled Polymerization”. In: *Laser & Photonics Reviews* 15.8 (2021), p. 2100090.

[109] J. del Barrio and C. Sánchez-Somolinos. “Light to shape the future: from photolithography to 4D printing”. In: *Advanced Optical Materials* 7.16 (2019), p. 1900598.

[110] S. Nocentini et al. “3D printed photoresponsive materials for photonics”. In: *Advanced Optical Materials* 7.16 (2019), p. 1900156.

[111] N. A. Chartrain, C. B. Williams, and A. R. Whittington. “A review on fabricating tissue scaffolds using vat photopolymerization”. In: *Acta biomaterialia* 74 (2018), pp. 90–111.

[112] S. Bynum et al. “The effect of acrylate functionality on frontal polymerization velocity and temperature”. In: *Journal of Polymer Science Part A: Polymer Chemistry* 57.9 (2019), pp. 982–988.

[113] I. D. Robertson et al. “Rapid energy-efficient manufacturing of polymers and composites via frontal polymerization”. In: *Nature* 557.7704 (2018), pp. 223–227.

[114] M. S. Malik et al. “Review on UV-induced cationic frontal polymerization of epoxy monomers”. In: *Polymers* 12.9 (2020), p. 2146.

[115] M. Vassallo et al. “Magnetic Hyperthermia to Promote Acrylamide Radical Polymerizations”. In: *ACS Applied Polymer Materials* 6.8 (2024), pp. 4696–4707.

[116] C. Zimmerer et al. “Inductive heating using a high-magnetic-field pulse to initiate chemical reactions to generate composite materials”. In: *Polymers* 11.3 (2019), p. 535.

[117] A. Ferraro et al. “Tailoring of plasmonic functionalized metastructures to enhance local heating release”. In: *Nanophotonics* 10.15 (2021), pp. 3907–3916.

[118] S. Ye et al. “Induction curing of thiol–acrylate and thiol–ene composite systems”. In: *Macromolecules* 44.12 (2011), pp. 4988–4996.

[119] A. Mittal, I. Roy, and S. Gandhi. “Magnetic nanoparticles: An overview for biomedical applications”. In: *Magnetochemistry* 8.9 (2022), p. 107.

[120] K. Simeonidis et al. “In-situ particles reorientation during magnetic hyperthermia application: Shape matters twice”. In: *Scientific reports* 6.1 (2016), p. 38382.

[121] H. Gavilán et al. “How size, shape and assembly of magnetic nanoparticles give rise to different hyperthermia scenarios”. In: *Nanoscale* 13.37 (2021), pp. 15631–15646.

[122] K. Kaczmarek et al. “The effect of tissue-mimicking phantom compressibility on magnetic hyperthermia”. In: *Nanomaterials* 9.5 (2019), p. 803.

[123] C. A. Schneider, W. S. Rasband, and K. W. Eliceiri. “NIH Image to ImageJ: 25 years of image analysis”. In: *Nature methods* 9.7 (2012), pp. 671–675.

[124] M. Coïsson et al. “Hysteresis losses and specific absorption rate measurements in magnetic nanoparticles for hyperthermia applications”. In: *Biochimica et Biophysica Acta (BBA)-General Subjects* 1861.6 (2017), pp. 1545–1558.

[125] M. Coïsson et al. “Specific loss power measurements by calorimetric and thermal methods on $\gamma$-Fe2O3 nanoparticles for magnetic hyperthermia”. In: *Journal of Magnetism and Magnetic Materials* 473 (2019), pp. 403–409.

[126] W. Kim et al. “A new method for the identification and quantification of magnetite–maghemite mixture using conventional X-ray diffraction technique”. In: *Talanta* 94 (2012), pp. 348–352.

[127] B. S. Yadav et al. “Facile synthesis of substantially magnetic hollow nanospheres of maghemite ($\gamma$-Fe 2 O 3) originated from magnetite (Fe 3 O 4) via solvothermal method”. In: *Journal of Superconductivity and Novel Magnetism* 33 (2020), pp. 2199–2208.

[128] R. Marsalek. “Particle size and zeta potential of ZnO”. In: *APCBEE procedia* 9 (2014), pp. 13–17.

[129] J. Feng et al. “Ultrasonic-assisted in situ synthesis and characterization of superparamagnetic Fe3O4 nanoparticles”. In: *Journal of Alloys and Compounds* 509.37 (2011), pp. 9093–9097.

[130] J. De Vicente et al. “Stability of cobalt ferrite colloidal particles. Effect of pH and applied magnetic fields”. In: *Langmuir* 16.21 (2000), pp. 7954–7961.

[131] B. D. Cullity and C. D. Graham. *Introduction to magnetic materials*. John Wiley & Sons, 2011.

[132] J. Chen et al. "Size-dependent magnetic properties of MnFe 2 O 4 fine particles synthesized by coprecipitation". In: *Physical review B* 54.13 (1996), p. 9288.

[133] C. Sciancalepore et al. "Structural characterization and functional correlation of Fe3O4 nanocrystals obtained using 2-ethyl-1, 3-hexanediol as innovative reactive solvent in non-hydrolytic sol-gel synthesis". In: *Materials Chemistry and Physics* 207 (2018), pp. 337–349.

[134] J. M. Vargas et al. "Temperature trends and correlation between SQUID superparamagnetic relaxometry and dc-magnetization on model iron-oxide nanoparticles". In: *Journal of Applied Physics* 127.4 (2020).

[135] S. Sun et al. "Monodisperse mfe2o4 (m= fe, co, mn) nanoparticles". In: *Journal of the American chemical society* 126.1 (2004), pp. 273–279.

[136] E. Lima et al. "Spin disorder and magnetic anisotropy in Fe3O4 nanoparticles". In: *Journal of Applied Physics* 99.8 (2006).

[137] H. Nemala et al. "Investigation of magnetic properties of Fe3O4 nanoparticles using temperature dependent magnetic hyperthermia in ferrofluids". In: *Journal of Applied Physics* 116.3 (2014).

[138] C. Nayek et al. "Size-dependent magnetic anisotropy of PEG coated Fe3O4nanoparticles; comparing two magnetization methods". In: *IOP Conference Series: Materials Science and Engineering*. Vol. 305. IOP Publishing. 2018, p. 012012.

[139] P. Allia et al. "Magnetic hysteresis based on dipolar interactions in granular magnetic systems". In: *Physical Review B* 60.17 (1999), p. 12207.

[140] M. Maccarini et al. "Interactions at the CMC/magnetite interface: implications for the stability of aqueous dispersions and the magnetic properties of magnetite nanoparticles". In: *Colloids and Surfaces A: Physicochemical and Engineering Aspects* 462 (2014), pp. 107–114.

[141] S. Nigam, K. Barick, and D. Bahadur. "Development of citrate-stabilized Fe3O4 nanoparticles: conjugation and release of doxorubicin for therapeutic applications". In: *Journal of Magnetism and Magnetic Materials* 323.2 (2011), pp. 237–243.

[142] S. Srivastava et al. "Innovative synthesis of citrate-coated superparamagnetic Fe3O4 nanoparticles and its preliminary applications". In: *Journal of colloid and interface science* 359.1 (2011), pp. 104–111.

[143] G. Aguilera et al. "Carboxymethyl cellulose coated magnetic nanoparticles transport across a human lung microvascular endothelial cell model of the blood–brain barrier". In: *Nanoscale Advances* 1.2 (2019), pp. 671–685.

[144] Y. Cai et al. “Synthesis of core–shell structured Fe 3 O 4@ carboxymethyl cellulose magnetic composite for highly efficient removal of Eu (III)”. In: *Cellulose* 24 (2017), pp. 175–190.

[145] B. Cortés-Llanos et al. “Influence of coating and size of magnetic nanoparticles on cellular uptake for in vitro MRI”. In: *Nanomaterials* 11.11 (2021), p. 2888.

[146] G. Barrera et al. “Specific loss power of Co/Li/Zn-mixed ferrite powders for magnetic hyperthermia”. In: *Sensors* 20.7 (2020), p. 2151.

[147] S. Ota and Y. Takemura. “Dynamics of magnetization and easy axis of individual ferromagnetic nanoparticle subject to anisotropy and thermal fluctuations”. In: *Journal of the Magnetics Society of Japan* 43.2 (2019), pp. 34–41.

[148] G. Barrera, P. Allia, and P. Tiberto. “Heating ability modulation by clustering of magnetic particles for precision therapy and diagnosis”. In: *Journal of Physics D: Applied Physics* 54.31 (2021), p. 315003.

[149] J. Wells, O. Kosch, and F. Wiekhorst. “Multi-frequency hyperthermia characterisation via calorimetry and AC magnetometry measurements”. In: *Journal of Magnetism and Magnetic Materials* 563 (2022), p. 169992.

[150] M. Ognjanović et al. “The effect of surface-modifier of magnetite nanoparticles on electrochemical detection of dopamine and heating efficiency in magnetic hyperthermia”. In: *Journal of Alloys and Compounds* 884 (2021), p. 161075.

[151] P. I. Soares et al. “Thermal and magnetic properties of iron oxide colloids: influence of surfactants”. In: *Nanotechnology* 26.42 (2015), p. 425704.

[152] P. Shete et al. “Magnetic chitosan nanocomposite for hyperthermia therapy application: Preparation, characterization and in vitro experiments”. In: *Applied Surface Science* 288 (2014), pp. 149–157.

[153] R. Ghosh et al. “Induction heating studies of Fe3O4 magnetic nanoparticles capped with oleic acid and polyethylene glycol for hyperthermia”. In: *Journal of Materials Chemistry* 21.35 (2011), pp. 13388–13398.

[154] K. Simeonidis et al. “A versatile large-scale and green process for synthesizing magnetic nanoparticles with tunable magnetic hyperthermia features”. In: *RSC advances* 6.58 (2016), pp. 53107–53117.

[155] K. El-Boubbou et al. “Evaluating magnetic and thermal effects of various Polymerylated magnetic iron oxide nanoparticles for combined chemo-hyperthermia”. In: *New Journal of Chemistry* 46.12 (2022), pp. 5489–5504.

[156] F. SENTURK, S. Çakmak, and G. G. OZTURK. "Synthesis and characterization of oleic acid coated magnetic nanoparticles for hyperthermia applications". In: *Natural and Applied Sciences Journal* 2.2 (2019), pp. 16–29.

[157] J. Gonçalves et al. "Coating of magnetite nanoparticles with fucoidan to enhance magnetic hyperthermia efficiency". In: *Nanomaterials* 11.11 (2021), p. 2939.

[158] K. Präbst et al. "Basic colorimetric proliferation assays: MTT, WST, and resazurin". In: *Cell viability assays: methods and protocols* (2017), pp. 1–17.

[159] V. Kuete, O. Karaosmanoğlu, and H. Sivas. "Anticancer activities of African medicinal spices and vegetables". In: *Medicinal spices and vegetables from Africa*. Elsevier, 2017, pp. 271–297.

[160] J. O'brien et al. "Investigation of the Alamar Blue (resazurin) fluorescent dye for the assessment of mammalian cell cytotoxicity". In: *European journal of biochemistry* 267.17 (2000), pp. 5421–5426.

[161] J. Weyermann, D. Lochmann, and A. Zimmer. "A practical note on the use of cytotoxicity assays". In: *International journal of pharmaceutics* 288.2 (2005), pp. 369–376.

[162] T. L. Riss et al. "Cell viability assays". In: *Assay Guidance Manual [Internet]* (2016).

[163] C. Divieto et al. "Uncertainty analysis of cell counting by metabolic assays". In: *Journal of Physics: Conference Series*. Vol. 459. 1. IOP Publishing. 2013, p. 012051.

[164] C. Divieto and M. P. Sassi. "A first approach to evaluate the cell dose in highly porous scaffolds by using a nondestructive metabolic method". In: *Future science OA* 1.4 (2015), FSO58.

[165] J. Petiti et al. *How to optimize resazurin-based viability assays: A549 cell line case report*. Tech. rep. Istituto Nazionale di Ricerca Metrologica, 2023.

[166] J. Petiti, L. Revel, and C. Divieto. "Standard operating procedure to optimize resazurin-based viability assays". In: *Biosensors* 14.4 (2024), p. 156.

[167] H. Kim et al. "In vitro magnetic hyperthermia properties of angle-shaped superparamagnetic iron oxide nanoparticles synthesized by a bromide-assisted polyol method". In: *RSC advances* 13.5 (2023), pp. 2803–2810.

[168] S. Tiwari et al. "Comprehensive in-vitro and magnetic hyperthermia investigation of biocompatible non-stoichiometric Zn0. 5Ca0. 5Fe2O4 and Mg0. 5Ca0. 5Fe2O4 nanoferrites on lung cancer cell lines". In: *Journal of Alloys and Compounds* 972 (2024), p. 172588.

[169] F. Chamani et al. “In vitro measurement and mathematical modeling of thermally-induced injury in pancreatic cancer cells”. In: *Cancers* 15.3 (2023), p. 655.

[170] K. Sharma et al. “Synthesis and characterization of monodispersed water dispersible Fe3O4 nanoparticles and in vitro studies on human breast carcinoma cell line under hyperthermia condition”. In: *Scientific reports* 8.1 (2018), p. 14766.

[171] A. Bhardwaj, K. Parekh, and N. Jain. “In vitro hyperthermic effect of magnetic fluid on cervical and breast cancer cells”. In: *Scientific Reports* 10.1 (2020), p. 15249.

[172] C. Iacovita et al. “In vitro intracellular hyperthermia of iron oxide magnetic nanoparticles, synthesized at high temperature by a polyol process”. In: *Pharmaceutics* 12.5 (2020), p. 424.

[173] H. Patel et al. “In vitro evaluation of magnetic fluid hyperthermia therapy on breast cancer cells using monodispersed Mn0. 5Zn0. 5Fe2O4 nanoflowers”. In: *Journal of Magnetism and Magnetic Materials* 587 (2023), p. 171275.

[174] D. Chang et al. “Biologically targeted magnetic hyperthermia: Potential and limitations”. In: *Frontiers in pharmacology* 9 (2018), p. 386237.

[175] A. E. Dunn et al. “Recent developments in the design of nanomaterials for photothermal and magnetic hyperthermia induced controllable drug delivery”. In: (2013).

[176] Y. Huang et al. “Repurposing ferumoxytol: Diagnostic and therapeutic applications of an FDA-approved nanoparticle”. In: *Theranostics* 12.2 (2022), p. 796.

[177] D. Prokopiou et al. “Synthesis and characterization of modified magnetic nanoparticles as theranostic agents: In vitro safety assessment in healthy cells”. In: *Toxicology in Vitro* 72 (2021), p. 105094.

[178] E. E. Connor et al. “Gold nanoparticles are taken up by human cells but do not cause acute cytotoxicity”. In: *Small* 1.3 (2005), pp. 325–327.

[179] C. M. Goodman et al. “Toxicity of gold nanoparticles functionalized with cationic and anionic side chains”. In: *Bioconjugate chemistry* 15.4 (2004), pp. 897–900.

[180] N. Lewinski, V. Colvin, and R. Drezek. “Cytotoxicity of nanoparticles”. In: *small* 4.1 (2008), pp. 26–49.

[181] S. D. Caruthers, S. A. Wickline, and G. M. Lanza. “Nanotechnological applications in medicine”. In: *Current opinion in Biotechnology* 18.1 (2007), pp. 26–30.

[182] O. Choi and Z. Hu. "Size dependent and reactive oxygen species related nanosilver toxicity to nitrifying bacteria". In: *Environmental science & technology* 42.12 (2008), pp. 4583–4588.

[183] M. A. Zoroddu et al. "Toxicity of nanoparticles". In: *Curr. Med. Chem* 21.33 (2014), pp. 3837–3853.

[184] N. Revi, O. D. Oladejo, and D. Bijukumar. "In Vitro, In Vivo and Ex Vivo Models for Toxicity Evaluation of Nanoparticles: Advantages and Disadvantages". In: (2023).

[185] P. L. Silva et al. "Mapping intracellular thermal response of cancer cells to magnetic hyperthermia treatment". In: *Nanoscale* 12.42 (2020), pp. 21647–21656.

[186] H. L. Karlsson et al. "Copper oxide nanoparticles are highly toxic: a comparison between metal oxide nanoparticles and carbon nanotubes". In: *Chemical research in toxicology* 21.9 (2008), pp. 1726–1732.

[187] M. Mahmoudi et al. "Assessing the in vitro and in vivo toxicity of superparamagnetic iron oxide nanoparticles". In: *Chemical reviews* 112.4 (2012), pp. 2323–2338.

[188] L. S. Arias et al. "Iron oxide nanoparticles for biomedical applications: a perspective on synthesis, drugs, antimicrobial activity, and toxicity". In: *Antibiotics* 7.2 (2018), p. 46.

[189] Y. Lu et al. "Citrate induces apoptotic cell death: a promising way to treat gastric carcinoma?" In: *Anticancer research* 31.3 (2011), pp. 797–805.

[190] B. Kruspig et al. "Citrate kills tumor cells through activation of apical caspases". In: *Cellular and molecular life sciences* 69 (2012), pp. 4229–4237.

[191] H. Mitome. "Action of ultrasound on particles and cavitation bubbles". In: *Proc. World Congress on Ultrasonics, Paris*. Vol. 2342. 2003.

[192] A. Manzin, R. Ferrero, and M. Vicentini. "From micromagnetic to in silico modeling of magnetic nanodisks for hyperthermia applications". In: *Advanced Theory and Simulations* 4.5 (2021), p. 2100013.

[193] S. Merabia et al. "Heat transfer from nanoparticles: A corresponding state analysis". In: *Proceedings of the National Academy of Sciences* 106.36 (2009), pp. 15113–15118.

[194] M. E. Smithmyer, L. A. Sawicki, and A. M. Kloxin. "Hydrogel scaffolds as in vitro models to study fibroblast activation in wound healing and disease". In: *Biomaterials science* 2.5 (2014), pp. 634–650.

[195] A. Cappitti et al. "Development of accessible platforms to promote myofibroblast differentiation by playing on hydrogel scaffold composition". In: *Biomaterials Advances* 155 (2023), p. 213674.

[196] H. Kaşgöz, S. Özgümüş, and M. Orbay. "Modified polyacrylamide hydrogels and their application in removal of heavy metal ions". In: *Polymer* 44.6 (2003), pp. 1785–1793.

[197] A. A. de Almeida et al. "Magnetic hyperthermia experiments with magnetic nanoparticles in clarified butter oil and paraffin: a thermodynamic analysis". In: *The Journal of Physical Chemistry C* 124.50 (2020), pp. 27709–27721.

[198] R. J. Pelham Jr and Y.-l. Wang. "Cell locomotion and focal adhesions are regulated by substrate flexibility". In: *Proceedings of the national academy of sciences* 94.25 (1997), pp. 13661–13665.

[199] J. Frohly et al. "Ultrasonic cavitation monitoring by acoustic noise power measurement". In: *The Journal of the Acoustical Society of America* 108.5 (2000), pp. 2012–2020.

[200] H. Corte-León et al. "Comparison and validation of different magnetic force microscopy calibration schemes". In: *Small* 16.11 (2020), p. 1906144.

[201] M. Vicentini, R. Ferrero, and A. Manzin. "In Silico Experiments to Explore the Heating Efficiency of Magnetic Nanoparticles in Hyperthermia Preclinical Tests". In: *Advanced Theory and Simulations* 6 (2023), p. 2300234.

[202] E. P. Furlani. "Magnetic biotransport: analysis and applications". In: *Materials* 3.4 (2010), pp. 2412–2446.

[203] R. K. Shah and A. L. London. *Laminar flow forced convection in ducts: a source book for compact heat exchanger analytical data*. Academic press, 2014.

[204] M. Monticelli et al. "On-Chip Magnetic Platform for Single-Particle Manipulation with Integrated Electrical Feedback". In: *Small* 12.7 (2016), pp. 921–929.

[205] N. R. Richbourg, M. K. Rausch, and N. A. Peppas. "Cross-evaluation of stiffness measurement methods for hydrogels". In: *Polymer* 258 (2022), p. 125316.

[206] C. M. Buffinton et al. "Comparison of mechanical testing methods for biomaterials: Pipette aspiration, nanoindentation, and macroscale testing". In: *journal of the mechanical behavior of biomedical materials* 51 (2015), pp. 367–379.

[207] P. Kosky et al. *Exploring Engineering. An Introduction to Engineering and Design*. Academic press, 2020.

[208] A. F. Prokop et al. "Polyacrylamide gel as an acoustic coupling medium for focused ultrasound therapy". In: *Ultrasound in medicine & biology* 29.9 (2003), pp. 1351–1358.

[209] N. Y. Abu-Thabit. "Thermochemistry of acrylamide polymerization: an illustration of auto-acceleration and gel effect". In: *World J Chem. Educ* 5.3 (2017), pp. 94–101.

[210] K. Kishore and K. Santhanalakshmi. "Thermal polymerization of acrylamide by differential scanning calorimetry". In: *Journal of Polymer Science: Polymer Chemistry Edition* 19.10 (1981), pp. 2367–2375.

[211] F. Soetaert et al. "Experimental estimation and analysis of variance of the measured loss power of magnetic nanoparticles". In: *Scientific reports* 7.1 (2017), p. 6661.

This Ph.D. thesis has been typeset by means of the TEX-system facilities. The typesetting engine was pdfLATEX. The document class was `toptesi`, by Claudio Beccari, with option `tipotesi=scudo`. This class is available in every up-to-date and complete TEX-system installation.